BACTERIAL FLAGELLAR MOTOR RESPONSES TO MECHANICAL AND CHEMICAL STIMULUS

A Dissertation

by

RAVI CHAWLA

Submitted to the Office of Graduate and Professional Studies of
Texas A&M University
in partial fulfillment of the requirements for the degree of

DOCTOR OF PHILOSOPHY

Chair of Committee,	Pushkar P. Lele
Committee Members,	Arul Jayaraman
	Steve W. Lockless
	Michael D. Manson
Head of Department,	Arul Jayaraman

December 2019

Major Subject: Chemical Engineering

ABSTRACT

Recent work has shown that the bacterial flagellar motor is able to regulate its structure in order to adapt to long-lived perturbations in the cell's thermal, chemical, electrical, and mechanical environments. These flagellar adaptations play a key role in invasion, colonization, and pathogenesis. However, the mechanisms of adaptations are unknown. Here, we determined the mechanisms of motor adaptation to mechanical and chemical stimuli with the overall goal of explaining how the motor regulates cell physiology.

The flagellar motor consists of a membrane-embedded stator and a transmembrane rotor. We determined the mechanisms whereby the flagellar stator-complex senses mechanical signals and remodels in response. The remodeling involves recruitment of additional stator-units to the original complex as the viscous load increases. Our experiments suggested that the association of stator units to the motor was strengthened when the torque they delivered to the rotor increased. An analytical model that incorporated an exponential decay of the stator unit's dissociation rate with increasing torque provided accurate fits to the experimental measurements of stator-rotor binding over a wide range of loads. When mechanical resistance to motor rotation increases, the torque delivered by each unit also increases. This leads to remodeling under increased viscous loads.

Next, we utilized flagellar motor output as a probe for the chemotactic responses of *E. coli* to a prominent gut microbiota metabolite, indole. Indole regulates numerous bacterial phenotypes, however, its role in the modulation of bacterial chemotaxis is poorly understood. We discovered that *E. coli* exhibited a time-dependent inversion in response to indole; a strong repellent response inverted to a potent attractant response above a threshold concentration of indole. The opposing responses were mediated by two major chemoreceptors. Interestingly, the flagellar motor itself mediated a repellent response independent of the receptors. Our chemotaxis assays revealed the broad implications of this inversion –wild-type cells were attracted to regions of high indole concentrations only if they had adapted to it previously. Otherwise, they were repelled. We propose that indole likely segregates beneficial and harmful bacteria based on their state of adaptation to promote the development of healthy niches in the GI tract.

DEDICATION

To my mother for always inspiring me to

push my limits and to never be satisfied with the status quo

"Life is not easy for any of us. But what of that? We must have perseverance and above all confidence in ourselves. We must believe that we are gifted for something, and that this thing, at whatever cost, must be attained."

— Marie Curie

ACKNOWLEDGEMENTS

First and foremost, I would like to thank my advisor Dr. Pushkar Lele for all his support for my development as a researcher. Second, I would like to thank Dr. Mike Manson for his constant belief in me and encouragement to think critically. I would also like to thank my committee members, Dr. Jayaraman and Dr. Lockless for their guidance throughout the course of this research.

Thanks also go to my lab members, friends and colleagues and the department faculty and staff for making my time at Texas A&M University a great experience. A special thanks to friends from 5th floor who helped me grow not only in my research but also personally. Finally, thanks to my parents and brother for their encouragement, patience, and love.

CONTRIBUTORS AND FUNDING SOURCES

Contributors

This work was supervised by a dissertation committee consisting of Dr. Pushkar Lele (advisor) and Dr. Arul Jayaraman of the Department of Chemical Engineering and Drs. Steve Lockless and Dr. Mike Manson of the Department of Biology.

Section 2 is a review article 'A skeptic's guide to bacterial mechanosensing' published in Journal of Molecular Biology. Rachit Gupta was instrumental in preparation of the manuscript. Section 3 is part of journal article 'Torque, but not FliL, regulates mechanosensitive flagellar motor-function' published in Scientific Reports (2017). Katie Ford conducted the bead-assay and analysis. Section 4 is part of the manuscript 'Induction of biphasic chemotaxis in *E. coli* by gut metabolite indole' currently under preparation. The experiments were carried out in collaboration with Jayaraman Research Group and Jingyun Yang (Department of Chemical Engineering) contributed equally. Kathy Rhee conducted the cytoplasmic pH experiments. Rachit Gupta helped generate PL15 Δ*tar* mutant for Section 4. Rachit Gupta analyzed the bead videos for surface-drag project described in Section 5.

All other work conducted for the dissertation was completed by me under the supervision of Dr. Pushkar Lele.

Funding Sources

This work was supported in part by grants from Texas A&M Engineering Experiment Station (TEES) start-up funds and from National Institutes of General Medical Sciences Health (R01-GM123085) to Dr. Pushkar Lele. The funding agency had no role in study design, data collection or interpretation, or the decision to submit the work for publication.

NOMENCLATURE

Amp	ampicillin
BFM	bacterial flagellar motor
CCW	counter-clockwise
CFP	cyan fluorescent protein
CW_{bias}	clockwise bias
DMSO	dimethyl sulfoxide
FRET	Forster resonance energy transfer
GFP	green florescent protein
IPTG	isopropyl β-D-thiogalactoside
Kan	kanamycin
LB	Lysogeny broth/ Luria Bertani media
MB	motility buffer
YFP	yellow florescent protein

TABLE OF CONTENTS

Page

LIST OF FIGURES

Page

LIST OF TABLES

Page

1. INTRODUCTION

The bacterial flagellum is widely known as the output of the chemotaxis network. However, recent work has shown that the flagellar motor is able to regulate its structure in order to adapt to long-lived perturbations in the cell's thermal, chemical, electrical, and mechanical environments. These flagellar adaptations appear to play a key role in invasion, colonization, and pathogenesis. Hence, in this work we were interested in determining the mechanisms for the motor's adaptive responses, in particular, to mechanical and chemical stimuli.

In Section 2, we have reviewed the current literature to better understand bacterial surface-sensing and mechanosensing. Surface sensing in bacteria is a precursor to the colonization of biotic and abiotic surfaces, and an important cause of drug resistance and virulence. As a motile bacterium approaches and adheres to a surface from the bulk fluid, the mechanical forces that act on it change. Bacteria are able to sense these changes in the mechanical load through a process termed mechanosensing. Bacterial mechanosensing has featured prominently in recent literature as playing a key role in surface sensing. However, the changes in mechanical loads on different parts of the cell at a surface vary in magnitudes as well as in signs. This confounds the determination of a causal relationship between the activation of specific mechanosensors and surface sensing. Here, we explain how contrasting mechanical stimuli arise on a surface adherent cell, and how known mechanosensors respond to these stimuli. The evidence for mechanosensing in select bacterial species is re-interpreted, with a focus on mechanosensitive molecular

motors. We conclude with proposed criteria that bacterial mechanosensors must satisfy to successfully mediate surface sensing.

Next, in Section 3, we investigated the bacterial flagellar motor as mechanosensor. The flagellar motor consists of a membrane-embedded stator and a transmembrane rotor. We first determined the mechanisms whereby the flagellar stator-complex senses mechanical stimuli and responds. The stator-complex remodels in response to perturbations in viscous loads (mechanical stimulus), recruiting additional stator-units as the load increases. We tested a hypothesis that the amount of torque generated by each stator-unit modulates its association with the flagellar rotor. To do this, we measured stator-binding to the rotor in mutants in which motors reportedly develop lower torque compared to wildtype motors. Then, we developed an analytical model that incorporated an exponential dependence of the unit's dissociation rate on the force delivered to the rotor. The model provided accurate fits to measurements of stator-rotor binding over a wide range of loads. Based on these results, we propose that the binding of each stator-unit is enhanced by the torque it develops.

Next, in Section 4, we utilized flagellar motor output as a probe for the chemotactic responses of *E. coli* to a metabolite indole. Indole, a key gastrointestinal tract microbiota metabolite, regulates numerous bacterial phenotypes, including stress response, drug resistance and biofilm formation. How indole modulates bacterial chemotaxis, an important virulence factor, is unclear. Here, we dissected the mechanisms underlying chemotaxis signaling in response to indole in *E. coli*. Tethered cells were stimulated with a range of indole concentrations and the chemotactic responses were inferred from the

output (CW_{bias}) of the flagellar switch. Below 1 mM indole concentration, a repellent response was observed. Between 1 – 2 mM concentrations of indole, a time-dependent inversion from repellent to attractant response was observed. Cells lacking the Tsr receptor exhibited an attractant response and those lacking the Tar receptor exhibited a strong repellent response, suggesting competing mediation by Tsr and Tar chemoreceptors. Additionally, direct interactions between indole and flagellar switch proteins induced a network-independent repellent response. Chemotactically-adapted cells migrated towards and adhered to indole-rich regions. In comparison, there was a 250% reduction in the number of adherent cells when they were not adapted to indole. Our observations are consistent with a model in which indole helps maintain healthy metabolite niches in the gastrointestinal tract by promoting selective colonization by beneficial bacteria.

In Section 5, we investigated the surface-drag force experienced by motile bacteria in proximity of agar surface to understand the underlying mechanical forces required to trigger morphological changes in motile bacteria. Surface-dependent collective motility of elongated, flagellated bacteria known as swarming represents an important mechanism for colonies to effectively cover large distances on soft surfaces and tissues. Swarming, involved in urinary tract infections, is likely initiated when the flagella sense higher viscous loads such as those experienced near solid boundaries. As cells of *E. coli* transition into the swarmer state, they develop twice as many flagella to overcome the surface drag. However, the underlying assumption that soft surfaces like agar result in high loads on the flagella remains untested. Here, we developed an approach to estimate the hydrodynamic drag as a function of separation from soft-agar interfaces. Blinking

optical tweezers were employed to estimate the variation of diffusion coefficient of latex beads as a function of separation from soft substrates interfaces using a novel geometry. A hard surface was used to validate the novel geometry and results of the transverse diffusion coefficient were in good agreement with published literature.

Lastly, in Appendix A, I describe the detailed Lambda Red recombination protocol we have employed to generate *E. coli* mutants in our lab.

2. A SKEPTIC'S GUIDE TO BACTERIAL MECHANOSENSING*

2.1. Introduction

Motile bacterial species spend a small fraction of their lifetime in a planktonic or vegetative state in a liquid medium. In their natural habitat, bacteria spend a majority of their lifetime in surface-associated states, for example, in biofilms or in swarmer colonies [1-5]. The transition from the planktonic state to a surface-associated state is typically initiated when a swimming bacterium encounters and senses a surface. The mechanisms responsible for the initiation of this transition are of considerable interest given the importance of bacterial surface-colonization in host invasion and infections, and in the failure of biomedical implants [6, 7]. Furthermore, bacteria in surface-associated states tend to exhibit elevated resistance to antibiotics [8-10].

The mechanical load on a bacterium changes as it approaches and adheres to a surface from the bulk fluid. Similar to mammalian cells [11-15], bacteria sense changes in the mechanical load through a process termed mechanosensing. Bacterial mechanosensing is likely to play a major role in surface sensing and in the initiation of intracellular signaling [16-19]. However, bacterial cells might experience varied mechanical stimuli at a surface, which can make it challenging to identify the role of

---

*Adapted with modifications from "A skeptic's guide to bacterial mechanosensing" by R. Chawla, R. Gupta, T.P. Lele, P.P. Lele, 2019. Journal of Molecular Biology, Article reference: 66263, doi.org/10.1016/j.jmb.2019.09.004,

specific mechanosensors in signaling. Also, surface sensing may occur through mechanisms that do not necessarily involve the detection of changes in mechanical loads. The cell could sense alterations in its chemical, electrical, or thermal environments upon surface-attachment and initiate intracellular signaling [20].

In order to correctly determine the role of mechanosensing in the transition from the planktonic state to a surface-associated state, it is critical to understand the type of mechanical load changes experienced by a cell at a surface. This in turn depends on how the bacterium attaches to the surface that is, the specific organelle(s) and/or portion of the cell body which mediate the surface attachment. The nature of the surface attachment determines which mechanosensors are triggered. However, an analysis of the type and magnitude of stresses that cells encounter at a surface is lacking. This may in part be responsible for why the surface sensing mechanisms and the molecular pathways involved in bacterial mechanotransduction remain obscure.

Here, we discuss prominent modes of bacterial attachments to a surface and how they lead to mechanical load-changes of varying magnitudes and contrasting signs. We explore how such opposing nature of load-changes pose a challenge in the analysis and in the interpretation of experimental results. We reinterpret prominent evidence for mechanosensitive signaling in select bacterial species in the context of mechanosensors. We then conclude with criteria that bacterial mechanosensors must meet in order to trigger mechanosensitive pathways.

2.2. Changes in Mechanical Load Following Surface-Attachment

Motile planktonic cells experience viscous resistance to their motion due to the surrounding fluid. A typical planktonic, flagellated bacterium swims at 30-100 μm/s in water and experiences a viscous drag force of ~ 0.5-1 pN. The cell body counter rotates at a speed of 10-20 Hz due to the rotation of the flagellar filament, resulting in a resistive torque on the cell body of ~ 1600 pN.nm. The resistive torque and the viscous drag together with the mechanical forces that arise due to contact with other cells and due to transient attachments to solid surfaces, establish a baseline viscous load that is ever-present on the cell body. When attachment to a surface obstructs motility in a quiescent fluid (Figure 2-1A), there is a dramatic reduction in the shear load on the cell body relative to the baseline (Figure 2-1B). These negative mechanical load changes occur the moment a cell ceases to swim, whether due to surface attachment or due to the loss of ion-motive-force that drives flagellar rotation. Such cessation in motility may activate putative mechanosensors on the surface of the cell body.

A membrane-embedded motor that actuates an extracellular appendage is a natural candidate for mechanosensors. This is because the motor can track changes in the mechanical loads by sensing changes in the viscous resistance to the movement of its appendage (i.e., the viscous load). Two motor-driven appendages, the flagellum and the type IV pilus, have been implicated in surface-sensing [21, 22]. The flagellum consists of an extracellular flagellar filament that is rotated by an electric transmembrane motor. The flagellar motor itself consists of a multi-unit stator that generates torque to rotate the rotor with the aid of the proton (ion)-motive-force [23]. The major components of the type IV

pilus include an extensible/retractile extracellular filament, and the ATPases responsible for retraction and extension. In order for the flagellar and pilus motors to sense surface-attachment and initiate signaling via mechanosensitive mechanisms, the viscous load on the respective appendages must change following the attachment.

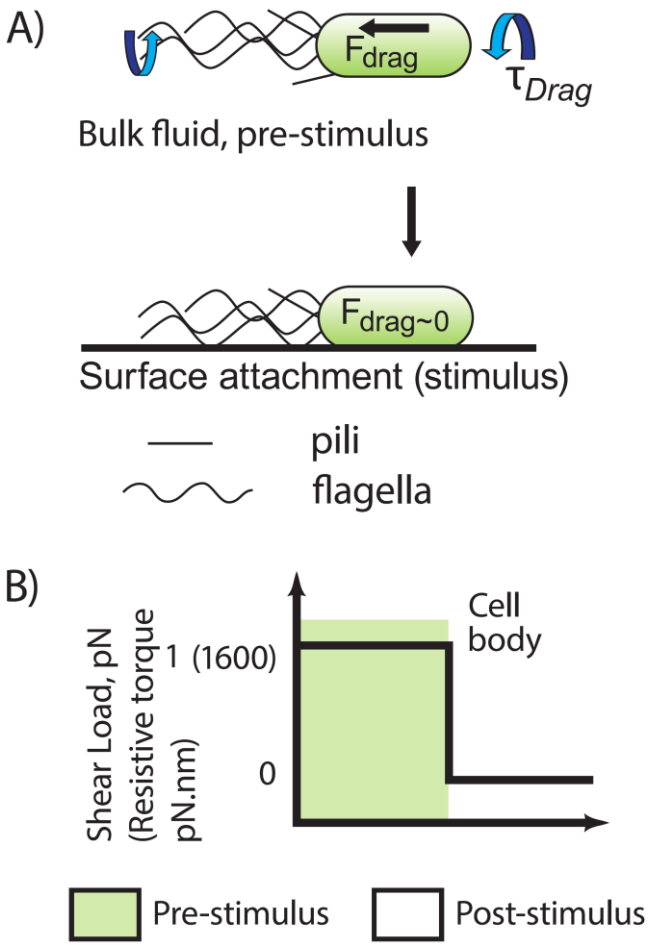

Figure 2-1 Load experienced by the bacterial cell body. A) A swimmer experiences a persistent viscous drag force (F_{Drag}) and a resistive torque (τ_{Drag}) due to its motility (top). When it encounters a surface that obstructs its motility, it immediately experiences a reduction in F_{Drag} and τ_{Drag} in a quiescent fluid. B) The pre-stimulus load on the cell body is proportional to the swimming speed and the cell's counter-rotation frequency. Attachment to a surface causes a negative change in load: change in F_{Drag} ~ -1 pN, and change in τ_{Drag} ~ -1600 pN-nm. Reprinted with permission from Chawla et al, 2019 [102].

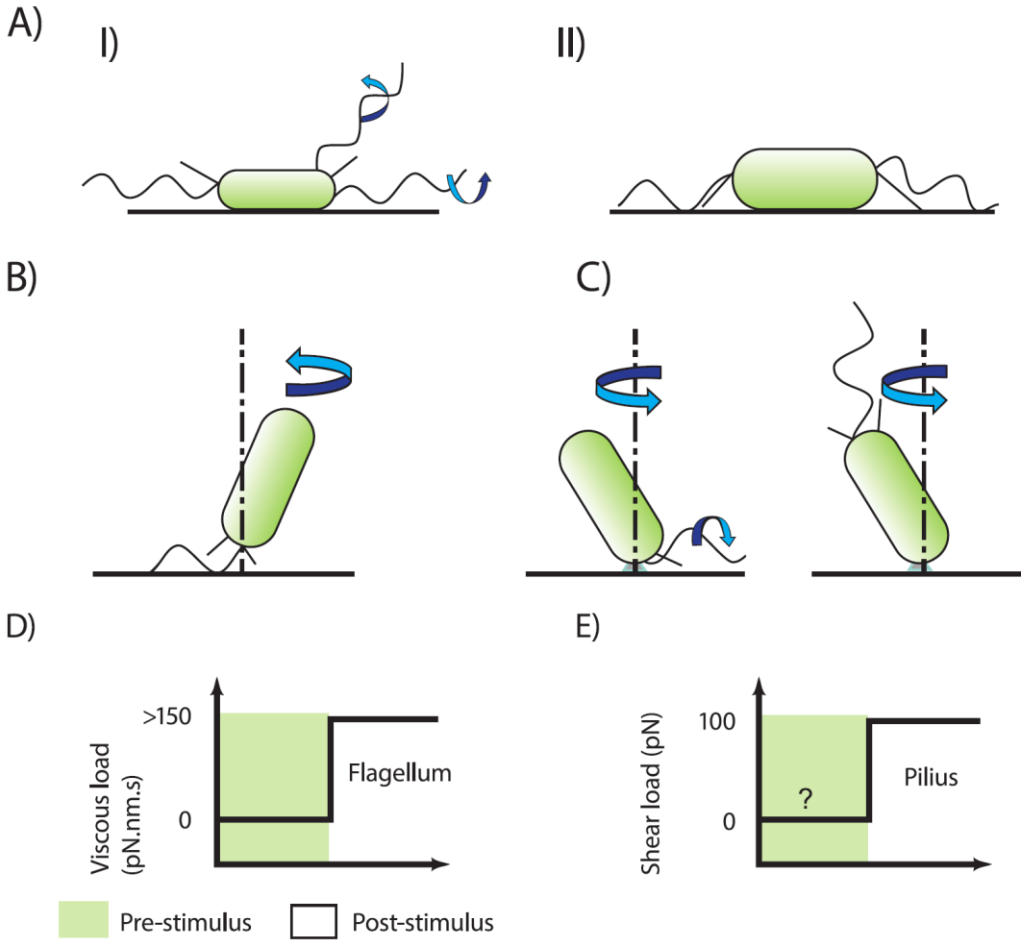

Figure 2-2 Load experienced by the bacterial appendages. A) Scenario I – cell body is surface-attached but the appendages are free and unloaded. Scenario II – the cell and prominent appendages become surface-attached and thus, loaded. B) Flagellar attachment to the surface will cause a rotation of the cell provided other appendages remain unattached. C) Cases where cell may attach to a surface due to the presence of adhesive components on its body, and is able to freely-pivot around the joint. Cell rotation occurs either due to hydrodynamic interactions of the rotating flagellum with the surface (left) or due to off-axis flagellar thrust that generates a torque on the cell (right). Another possibility is that the cell simply counter-rotates around the fluid joint due to on-axis flagellar rotation. D) Increase in flagellar and pili-loads when the respective appendages attach to the surface and are stalled, as indicated in scenario II. Reprinted with permission from Chawla et al, 2019 [102].

The magnitudes of load changes on these appendages depend on the manner of cell attachment to the surface (Figure 2-2A). For example, the cell body might attach to the surface such that the appendages remain free (scenario I). Alternately, the cell body including some or all the appendages may adhere to the surface (scenario II). Often, a single flagellum alone may attach to the surface (Figure 2-2B). This is typically achieved in the laboratory with the aid of flagellin variants that stick readily to hydrophobic surfaces [24], or with anti-flagellin antibodies that link the flagellum to the surface [25, 26]. In these cases, the cell has been 'tethered' and it rotates. Rotation of the cell body does not require flagellar tethering to a surface though. It can also occur due to hydrodynamic interactions of the rotating flagellum with the surface (Figure 2-2C, [27]).

The load on the flagellar motor due to viscous drag on the rotating flagellar filament in a swimming cell is ~ 5 pN.nm.s/rev. The motor experiences a significant mechanical load (> 150 pN.nm.s/rev, [28]) if the filament adheres to the surface (Figure 2-2A, scenario II and Figure 2-2B). As a result, the attachment corresponds to a significant increase in the load on the flagellum of > 145 pN.nm.s/rev (Figure 2-2D). In contrast, the flagellar load changes are modest in a rotating cell body which appears to be tethered via its flagellum, but is actually surface-adherent due to a fluid joint (Figure 2-2C).

The pili are free from any attachments in a swimming cell. Therefore, they should experience negligible tensile loads during swimming. When they adhere to the surface, they are capable of pulling and moving the entire cell body, resulting in twitching motility [29, 30]. Tensile forces within the extracellular filament balance the retracting force applied by the force-generating enzymes in the pilus, and these forces can range from 8 -

100 pN [31-34]. The tensile forces act as the load on the force-generating pilus motor. The load is high when the pilus adheres to the surface (e.g., scenario II, Figure 2-2A), and it is negligible when the pilus detaches from the surface and extends (e.g. scenario I, Figure 2-2A). Because the pili stochastically attach and detach from the surface [35], the load on the pilus-motor changes over time. Nonetheless, the load-change experienced by a surface-adherent pilus can be as high as 100 pN (Fig 2E).

Since the appendages are not easily observable, it is not straightforward to determine how they interact with the surface in standard microscopy experiments [36]. Yet in each of the above representative scenarios, the type and magnitude of mechanical load change is different. Therefore, the knowledge of the nature of surface-attachment is crucial in order to discriminate between mechanosensitive and non-mechanosensitive signaling during bacterial-surface interactions.

In addition to the changes in load depicted in Figure 2-1 and Figure 2-2, the bacterium may experience other types of mechanical stimuli at a surface, especially when exposed to fluid flows. Gravitational forces are negligible because of the small size of the bacterium; likewise any balancing reaction force from the surface is also negligible. But, strong adhesion interactions can occur between the surface and the cell [20]. These forces can resist detachment forces as high as a few nN [37] and are predicted to cause cell wall deformations [38]. Mechanosensitive proteins within the cell membranes are believed to be able to detect deformations in the cell wall [18, 39]. However, significant cell deformations do not seem to occur in surface-adherent wildtype bacteria even over an hour following attachment [40].

Swimming bacteria in the bulk fluid frequently encounter other cells or diffusing objects, physically. In order to prevent premature turning-on of mechanosensitive signaling in the bulk fluid, a bacterial mechanosensor should become activated and initiate signaling primarily in response to load-changes that arise during surface attachment. One way to ignore basal mechanical loads and to respond selectively to surface-attachment is by discriminating between load changes based on their magnitudes. However, as should be evident from the foregoing discussion, not only the magnitudes but also the signs of the surface-induced mechanical stimuli are different on different parts of the cell. Several types of load-changes can occur simultaneously during surface-attachment. For example, when a swimming bacterium adheres to a surface along with its appendages (Figure 2-2A scenario II), not only does the viscous drag on the cell body decrease, but the flagellar and the pili loads also increase simultaneously. There may be an additional increase in the adhesive forces on the cell in presence of hydrodynamic flows. This suggests that a primary criterion for the effective functioning of a bacterial mechanosensor is that it must be able to discriminate between the magnitudes as well as the signs of mechanical stimuli.

In the next sections, we discuss the response of bacterial mechanosensors to load changes, and the challenges in interpretation of experimental results involving bacterial mechanosensing.

2.3. Sensing of load changes

The levels of select messenger molecules in the bacterium can change when the cell attaches to a surface. Examples are the global regulators cyclic diguanylate monophosphate (c-di-GMP) and cyclic adenosine monophosphate (cAMP), which

regulate a variety of cellular processes such as surface colonization, biofilm formation, cell cycle regulation, and virulence [17, 41-46]. Here, we focus on how mechanosensors, especially mechanosensitive molecular motors, detect load-changes to modulate the activity of regulatory molecules.

2.3.1. Mechanosensing by motors

Mechano-sensing by the flagellar motors: Flagella have been implicated in sensing of and cellular adaptation to surfaces in numerous bacterial species [2, 22, 47, 48] and large number of bacterial species carry flagellar genes [49]. To determine how flagella respond to mechanical load-changes (Fig 2D), Lele and co-workers employed optical traps to stick beads to shortened flagellar filaments in *E. coli* cells. Because the load on the flagellar motor scales cubically with the size of the object that it rotates, attachment of the bead to the short flagellum instantaneously increased the load on the motor by a factor of ~ 8000 [50]. In an alternate experiment, they tethered the cell to a surface similar to the manner depicted in Fig 2B. In either case, the flagellar stator complex responded by adding ~ 6 - 11 stator units to increase the flagellar power under high loads [50]. Another study showed that such load-dependent binding of stator units to individual motors was persistent; the remodeled units continued to associate with the motor despite the stalling of rotation for several minutes [51]. These observations and other observations suggest that the flagellar stator is the mechanosensitive protein complex. The structural remodeling of the stator complex and the resultant functional adaptation in response to flagellar load changes has so far been reproducibly observed in *E. coli* and *B. subtilis* [28, 50-55].

The viscous load on the extracellular flagellum should be experienced by the flagellar motor only so long as the stator continues to generate torque. Consistent with this idea, torque-generating stators were observed to remodel when the flagella were tethered to the surface, but paralyzed stators that were unable to generate torque did not remodel in tethered cells [28]. These findings are consistent with a model in which the unbinding/binding rates of a stator-unit to the motor are controlled by the torque the unit generates [28]. There is additional support for this idea; recent experiments indicate that the unbinding rates of stator molecules decrease as torque increases, and the on-rates decrease with speed when the motor speeds are high [56].

Mechanosensing by stators may contribute to the initation of biofilm formation, swarming, increased expression of virulence genes, as well as in the regulation of genetic competence [47] [57]. The mechanisms are unknown. One possibility is that stator-remodeling under high loads modifies the local cell membrane potential, which could subsequently initiate signaling [58]. Or the increased torque upon remodeling might modify rotor interfaces to enhance the binding of downstream effectors that are involved in signaling. Another model involves the depletion of the pool of free stator units in the cell due to load-dependent remodeling. The depletion in free stator units could trigger downstream signaling. There is some experimental support for this. For example, two types of stators, MotA-B and MotC-D, are responsible for flagellar-rotation in *P. aeruginosa*. MotC-D is recruited by the motor in preference to MotA-B under high loads, which appears to modulate interactions with diguanylate cyclases and the levels of c-di-GMP [44, 57]. However, there are around 100-200 total stator units in a cell [59], with

each motor likely binding around 4-6 units at loads experienced in swimming cells, and no more than 11-16 units at maximum loads [60-62]. In the depletion model, the messenger molecule levels would have to be very sensitive to small changes in the number of freely-available stator units in the cell (of the order of 7-10 stator units). In species such as *P. aeruginosa* that carry a lone flagellar motor, the reduction in the number of free stator units upon surface-attachment is expected to be < 5%. This mechanism poses a challenge as it may necessitate an impracticably tight control over cell to cell variability in stator protein copies.

Mechanosensing by the type IV pilus*:* Mechanical stimuli-induced structural modifications and functional adaptations that are readily measurable in flagellar motors have not been reported in the type IV pilus yet. However, the activity of the motor enzymes is likely responsive to mechanical contact between the tip of the pilus and a surface [63]. Sensing of the surface by the pilus is typically inferred from subsequent downstream effects in signaling [64-69]. In *Pseudomonas aeruginosa*, the extracellular pilin filament consists of PilA subunits and the retraction is facilitated by the ATPase PilT. PiIT has been implicated in downstream signaling events and the upregulation of virulence [66, 70]. If PiIT is capable of sensing the tensile load in the extracellular filament, it could function as a mechanosensitive protein similar to stator proteins in the flagellar motor.

A prominent example of pili-mediated post-translational signaling is that of hold-fast induction in *Caulobacter crescentus* [69]. The hold-fast is a strong adhesin which irreversibly attaches a cell via its pole to a surface, resulting in rapid surface-colonization. The induction begins almost immediately following surface-attachment [71, 72].

Although some evidence indicates that the pili induce holdfast synthesis, other experimental observations point to a prominent role for the flagellar motor instead [73]. This might likely be due to a cross-talk between the two appendages [34, 74]. Interestingly, holdfast induction is observed even in strains lacking the pili and the extracellular components of the flagella, so long as functional components of the flagellar rotor and the stator units were present within the cell body [73]. This type of sensing has been termed as tether-less surface-sensing. As discussed before, without the extracellular tethers, motors are unlikely to sense changes in extracellular viscous loads. Hence, whether surface-sensing by the pili and the flagella in *C. crescentus* is evidence of mechanosensing remains an open question.

2.3.2. Mechanosensing with non-motor proteins

Putative non-motor bacterial mechanosensors include protein-sensors that may reside on the cell surface. Motile cells in gram negative species may sense reduction in the viscous drag on their bodies (Fig 1B) with the aid of outer-membrane mechanosensors. Alternately, the sensors might undergo conformational changes due to the proximity to charged entities on a surface or due to some other reason [20]. Parsing the extent to which these sensors respond to surface conditions versus changes in mechanical load is a significant challenge.

Candidate mechanosensors include the outer-membrane lipoprotein NlpE in *E. coli* which likely triggers the CpxA-R two component signaling pathway upon surface contact [75]. The CpxA-R system is involved in the invasion of host cells, as well as in multidrug resistance [76-79]. Recent work implicates the RcsCDB phosphorelay system

in surface-sensing, which involves the outer-membrane lipoprotein RcsF [80]. The Rcs system regulates biofilm growth, modulates the expression of motility genes, and mediates a variety of bacterial functions [81]. In *P. aeruginosa*, outer-membrane protein PilY1 likely mediates bacterial attachment to surfaces [67, 82].

The area of contact between the bacterial body and the surface is typically small, probably < 5% of the total area of the bacterial surface (Figure 2-3A). Furthermore, a thin fluid layer ~ 5-20 nm separates the two [83, 84]. As any part of the bacterial outer surface may randomly come to rest on the surface, the limited contact area imposes a spatial constraint on the functioning of outer membrane mechanosensors. This is because the large majority of these mechanosensors are on the non-contacting cell area (> 95 %), and do not experience the mechanical perturbations experienced by the contacting mechanosensors. How might such a small number of contacting sensors trigger signaling? Additionally, how might membrane mechanosensors distinguish between attachment to a surface and the occasional contact with objects in the bulk fluid? One possibility is that the cell relies on temporal integration of the signal that is received from the mechanosensors such that once a signal-threshold is exceeded, mechanosensitive pathways are triggered. In such a mechanism, transient contacts will be filtered out since the integrated signal will remain below the threshold. If however, the cell relies on spatial integration of sensor-signals, then a high sensitivity to mechanical contact and a high degree of cooperativity among the contacting and non-contacting sensors could help limit the number of sensors required on the cell body, while possibly resolving conflicting

signals. A good example of high cooperativity is seen in bacterial chemoreceptors that are distributed in dense patches in the inner membrane [85, 86].

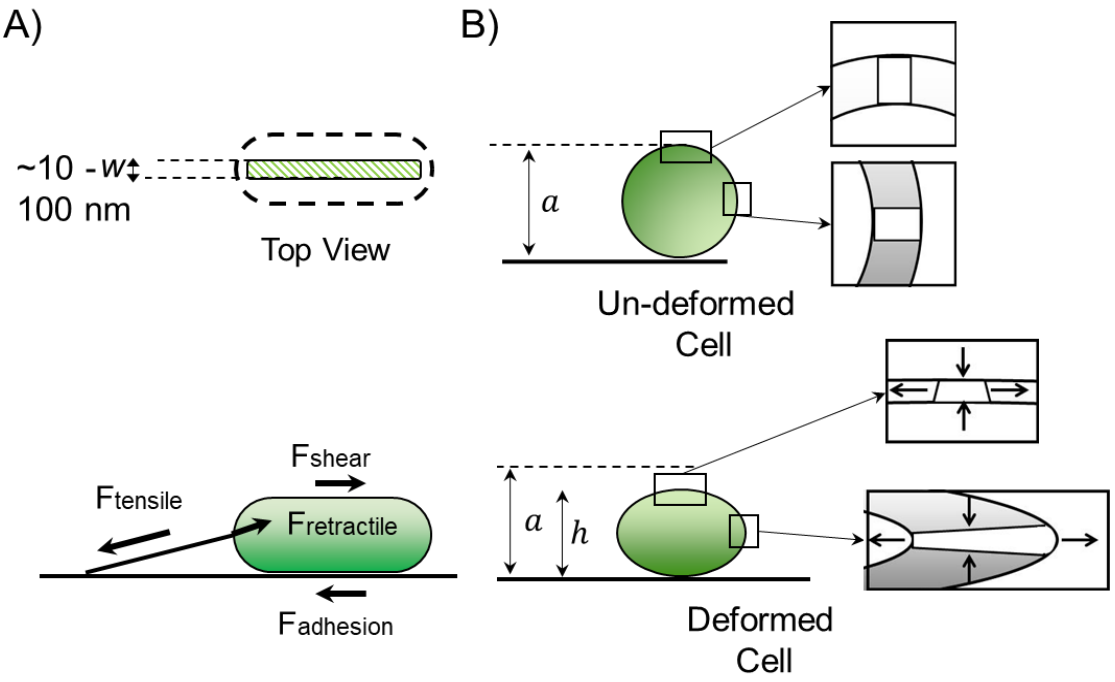

Figure 2-3 Adhesion forces and putative mechanosensitive channels. A) *Top:* The contact area between the surface and the attached cell is a tiny fraction of the overall surface area of the cell (top view). The adhesion forces act only on this area. *Bottom:* In a non-quiescent fluid, the tensile force on a surface-adherent pilus is a combination of the shear force, the adhesion force, and the retractile force. When the fluid flow is in a direction opposite to the retractile force, it reduces the total tensile force. B) An attached cell viewed along its pole. *Top:* the un-deformed cell diameter is *a*. Inactive putative mechanosensitive channels embedded within the cell membrane are indicated in the inset figures. *Bottom*: The cell deforms over a period of time to *h*, and the channels along the top and side sections of the cell experience different forces as indicated in the inset. Reprinted with permission from Chawla et al, 2019 [102].

Ion channels such as MscL and MscC in the inner membrane of bacteria respond to stresses generated in the membranes [38, 87, 88]. In addition to adhesion forces, the strong forces generated by the pilus and/or flagellar motors upon surface-attachment could

modulate the mechanical stresses within the membranes, and trigger these sensors. Typical host surfaces that may be colonized by bacteria such as cells, tissues, or mucosal layers are soft and deformable, though. Their flexibility will limit the development of mechanical stresses in bacteria. The cell wall is highly rigid (~ 0.1 GPa,[89-91]) such that for a characteristic cell dimension of ~1 μm, a force of 100 pN motor-force will cause insignificant overall cell wall deformation (< 1 nm). If significant deformation does occur, different parts of the cell wall will experience either compressive or tensile stresses, resulting in contrasting stimuli on putative sensors (Figure 2-3B). Much work remains to be done to uncover whether and how non-motor mechanosensors respond to such contrasting and small mechanical stresses.

2.4. Dynamics of Mechanosensing

The bacterium likely discriminates between real mechanical signals that arise due to surface attachment from those that might be transient or short-lived, such as the occasional interactions with another cell or solid objects in the bulk fluid, by sensing the persistence of mechanical signals. Sensing only those stimuli that persist for long enough times may help reduce the occurrence of erroneous signaling [66]. Measurements of the relevant time scales are limited, but they are likely to be on the order of several seconds. For example, in *E. coli*, stator remodeling initiates within ~ 10 seconds after the load change on the flagellar motor [50, 92], while in *P. aeruginosa*, the flagellar motor modulates c-di-GMP levels within a few seconds of surface attachment [93].

For a motor-based mechanosensor, temporal persistence in mechanical stimulus is force- or torque-dependent as inhibition of force/torque dissipates the load. For non-motor based mechanosensors, temporal persistence in mechanical stimulus is probably dependent on the specificity of adhesive interactions with surfaces. For example, the type 1 fimbrial FimH adhesin binds with high specificity to D-mannose, and the adhesion is shear-dependent [94-96]. Specificity in binding might help trigger specific pathways due to strong and persistent interactions. Non-specific adhesions are likely to be transient and weak, therefore, such interactions may not trigger specific signaling pathways, or may be too slow to initiate signaling. Testing of these ideas will likely contribute to a better understanding of mechanosensing.

Disruption in enzymatic functions via genetic modifications has been widely-employed to study the role of mechanosensitive proteins in the initiation of intracellular signaling. However, bacterial mechanosensing and mechanotransduction are dynamic processes, and approaches that involve load-changes through genetic modifications may not be optimally suited for exploring these dynamics. This is because the mechanosensitive response may adapt to the loss or mutation of a putative critical enzyme. If the responses pre- and post-genetic modification happen to be similar, then the role of the mechanosensitive protein encoded by that gene may remain undetected in experiments altogether.

2.5. Mechanosensing, Shear Rate Sensing and Swimming-Speed Sensing

A common approach to mechanically stimulate bacteria is to adhere them to a surface, and then apply increasing shear stresses through fluid flows over the cell and its

appendages (Fig 3A). The typical viscous stresses on the bacterium in such experiments are very small (F_{shear} ~ 0.002-0.01 pN, [82]), partly owing to the small chamber sizes in laboratory flowcells. Recent experiments with this approach indicate that c-di-GMP levels in surface-adherent *P. aeruginosa* increase with hydrodynamic flow rates, with the current interpretation being that the shear stresses generated by the flows are responsible for the increase [82]. The applied stresses on adherent cells in these experiments though are orders of magnitude smaller than those typically experienced by swimmers (F_{Drag} ~ 1 pN, Figure 2-3B). If high shear stresses on the cell body elevate c-di-GMP levels, then the levels would be higher in swimming bacteria, which is not the case. Perhaps these flows increase the load on surface-adherent pili and the pili mediate downstream signaling in response. However, the tensile loads on a surface-adherent and retracting pilus are already ~ 100 pN (Figure 2-1E). Hence, an F_{shear} ~ 0.01 pN is not expected to change pilin loads appreciably (Figure 2-3A). Since the loads on the pili with and without the hydrodynamic flows are likely similar, the mediation of biochemical signaling by the pili may occur through non-mechanosensitive pathways in this example. Alternately, the c-di-GMP levels are modulated by the adhesion forces between the bacterium and the surface, which balance the hydrodynamic shear force. If this is the case, the phenomenon may be mechanosensitive, with a small number of outer membrane-embedded mechanosensors in the narrow contacting area playing a key role.

Hydrodynamic flows reduce the concentrations of secreted chemical species that build up near surface-adherent cells. The depletion of these chemicals due to the flows could also play a role in initiating cell-signaling. This notion is consistent with recent

findings that suggest that the expression of certain genes in *Pseudomonas aeruginosa* is regulated by hydrodynamic shear rates, rather than the shear forces induced by flows [97]. Because the shear rate in such experiments is a measure of the fluid velocity relative to the surface-adherent cell body, another way of interpreting the results is to ask whether the expression of genes is tied to the swimming speed of the bacterium in quiescent fluid. Higher the swimming speed, greater the apparent shear rate. An intriguing possibility then exists – does the cell sense how fast it swims and thereby regulates signaling? One mechanism for the cell to determine its own swimming speed is to keep track of the flagellar rotation rates based on the proton (or ion) influx through flagellar stators. Another mechanism could be to track the levels of the chemical species it secretes.

Not all mechanosensitive signaling pathways are surface-dependent. For example, the transition of *B. subtilis* into the so-called K-state promotes natural competence [98]. Entry into the K-state is independent of surface-adhesion and correlates with basal levels of DegU phosphorylation. DegU is a transcriptional regulatory protein and a response regulator in *Bacillus subtilis* that regulates genetic competence and biofilm formation [99]. Diethmaier and co-workers recently observed that a reduction in flagellar loads correlated with elevated DegU-P levels and reduced K-state transition probabilities. Flagellar stalling also seems to elevate DegU-P levels [48, 100]. This surface-independent, flagellar-mediated control of DegU-P levels appears consistent with a mechanism in which the viscous load on the flagellum is optimal in a wildtype swimmer for maintaining basal DegU-P levels. However, as flagellar mechanosensing is mediated by flagellar stators, it is possible that these proteins regulate DegU-P. Yet, in the above experiments that

interfered with flagellar functions, the swimming speed of the cell was affected as well. Therefore, an alternate interpretation is that at least in some of these experiments, reduction in viscous drag (Figure 2-1B) caused by the disruption of flagellar rotation activates mechanosensors on the cell surface. Yet another possibility is that a loss of motility may by itself activate signaling.

2.6. Summary and future directions

The evidence summarized in this paper suggest the following criteria for the proper functioning of a bacterial mechanosensor:

a. Ability to sense differences in the signs and magnitudes of mechanical stimuli.

b. Ability to detect temporal persistence of mechanical stimuli to filter out noise.

c. High sensitivity to mechanical signals and cooperative behavior, especially in case of mechanosensors that do not rely on motor action.

There are multiple challenges that limit our understanding of bacterial mechanosensing. First, the dynamics of mechanosensing are relatively understudied and not well-understood. Challenges also exist in the design of experiments for stimulating putative mechanosensors. Among these is determining whether a particular appendage such as the flagellum or the pilus is actually loaded in a mechanical-stimulation assay. To obtain unambiguous evidence regarding the role of a specific type of appendage in mechanosensing, it may help to simultaneously load all or a majority of the multiple appendages of that type on the cell. This can be challenging, in part, due to the technical difficulties in appendage-visualization. These challenges are being overcome with

exciting techniques based on interferometric approaches [63, 101]. To distinguish between signaling events that are activated by mechanosensing from those that may be activated by other types of surface sensing phenomena, a comparative analysis of the mechanosensing response in the bulk fluid away from any surfaces will be necessary. Determining how mechanosensors initiate post-translational modifications, how various regulatory events are controlled by shear rates and shear stresses on the cell, and discriminating between mechanosensing mechanisms from other surface sensing mechanisms are among the key challenges for the future.

2.7. References

[1] Kearns DB. A field guide to bacterial swarming motility. Nat Rev Microbiol. 2010;8:634.

[2] Belas R. Biofilms, flagella, and mechanosensing of surfaces by bacteria. Trends Mcrobiol. 2014;22:517-27.

[3] Mattingly AE, Weaver AA, Dimkovikj A, Shrout JD. Assessing Travel Conditions: Environmental and Host Influences on Bacterial Surface Motility. J Bacteriol. 2018;200:e00014-18.

[4] Verstraeten N, Braeken K, Debkumari B, Fauvart M, Fransaer J, Vermant J, et al. Living on a surface: swarming and biofilm formation. Trends Microbiol. 2008;16:496-506.

[5] Henrichsen J. Bacterial surface translocation: a survey and a classification. Bacteriol Rev. 1972;36:478-503.

[6] Khatoon Z, McTiernan CD, Suuronen EJ, Mah T-F, Alarcon EI. Bacterial biofilm formation on implantable devices and approaches to its treatment and prevention. Heliyon. 2018;4:e01067-e.

[7] Costerton JW, Stewart PS, Greenberg EP. Bacterial biofilms: a common cause of persistent infections. Science. 1999;284:1318-22.

[8] Lai S, Tremblay J, Deziel E. Swarming motility: a multicellular behaviour conferring antimicrobial resistance. Environ Microbiol. 2009;11:126-36.

[9] Davies D. Understanding biofilm resistance to antibacterial agents. Nat Rev Drug Discov 2003;2:114-22.

[10] Donlan RM, Costerton JW. Biofilms: survival mechanisms of clinically relevant microorganisms. Clin Microbiol Rev. 2002;15:167-93.

[11] Wang JHC, Thampatty BP. An Introductory Review of Cell Mechanobiology. Biomech Mode Mechanobiol. 2006;5:1-16.

[12] Janmey PA, Weitz DA. Dealing with mechanics: mechanisms of force transduction in cells. Trends Biochem Sci. 2004;29:364-70.

[13] Paluch EK, Nelson CM, Biais N, Fabry B, Moeller J, Pruitt BL, et al. Mechanotransduction: use the force(s). BMC biology. 2015;13:47-.

[14] Leckband DE, de Rooij J. Cadherin adhesion and mechanotransduction. Annu Rev Cell Dev Biol. 2014;30:291-315.

[15] Mammoto A, Mammoto T, Ingber DE. Mechanosensitive mechanisms in transcriptional regulation. J Cell Sci. 2012;125:3061-73.

[16] Hughes KT, Berg HC. The bacterium has landed. Science. 2017;358:446.

[17] Gordon VD, Wang L. Bacterial mechanosensing: the force will be with you, always. J Cell Sci. 2019;132:jcs227694.

[18] Booth IR. Bacterial mechanosensitive channels: progress towards an understanding of their roles in cell physiology. Curr Opin Microbiol. 2014;18:16-22.

[19] Persat A, Nadell CD, Kim MK, Ingremeau F, Siryaporn A, Drescher K, et al. The mechanical world of bacteria. Cell. 2015;161:988-97.

[20] Tuson HH, Weibel DB. Bacteria-surface interactions. Soft Matter. 2013;9:4368-80.

[21] O'Toole GA, Kolter R. Flagellar and twitching motility are necessary for *Pseudomonas aeruginosa* biofilm development. Mol Microbiol. 1998;30:295-304.

[22] Mccarter L, Hilmen M, Silverman M. Flagellar dynamometer controls swarmer cell-differentiation of *V-Parahaemolyticus*. Cell. 1988;54:345-51.

[23] Berg HC. The Rotary Motor of Bacterial Flagella. Annu Rev Biochem. 2003;72:19-54.

[24] Scharf BE, Fahrner KA, Turner L, Berg HC. Control of direction of flagellar rotation in bacterial chemotaxis. Proc Natl Acad Sci USA. 1998;95:201-6.

[25] Berg HC, Anderson RA. Bacteria swim by rotating their flagellar filaments. Nature. 1973;245:380-2.

[26] Silverman M, Simon M. Flagellar rotation and the mechanism of bacterial motility. Nature. 1974;249:73-4.

[27] Lele PP, Roland T, Shrivastava A, Chen YH, Berg HC. The flagellar motor of *Caulobacter crescentus* generates more torque when a cell swims backwards. Nat Phys. 2016;12:175-8.

[28] Chawla R, Ford KM, Lele PP. Torque, but not FliL, regulates mechanosensitive flagellar motor-function. Sci Rep. 2017;7:5565.

[29] Wall D, Kaiser D. Type IV pili and cell motility. Molecular microbiology. 1999;32:1-10.

[30] Bradley DE. A function of *Pseudomonas aeruginosa* PAO polar pili: twitching motility. Can J Microbiol. 1980;26:146-54.

[31] Clausen M, Jakovljevic V, Søgaard-Andersen L, Maier B. High-force generation is a conserved property of type IV pilus systems. J Bacteriol. 2009;191:4633-8.

[32] Merz AJ, So M, Sheetz MP. Pilus retraction powers bacterial twitching motility. Nature. 2000;407:98.

[33] Maier B, Potter L, So M, Seifert HS, Sheetz MP. Single pilus motor forces exceed 100 pN. Proc Natl Acad Sci. 2002;99:16012-7.

[34] Sangermani M, Hug I, Sauter N, Pfohl T, Jenal U. Tad Pili Play a Dynamic Role in *Caulobacter crescentus* Surface Colonization. MBio. 2019;10.

[35] Skerker JM, Berg HC. Direct observation of extension and retraction of type IV pili. Proc Natl Acad Sci. 2001;98:6901-4.

[36] Burrows LL. *Pseudomonas aeruginosa* twitching motility: type IV pili in action. Annual review of microbiology. 2012;66:493-520.

[37] Liu Y, Strauss J, Camesano TA. Adhesion forces between *Staphylococcus epidermidis* and surfaces bearing self-assembled monolayers in the presence of model proteins. Biomaterials. 2008;29:4374-82.

[38] Harapanahalli AK, Younes JA, Allan E, van der Mei HC, Busscher HJ. Chemical Signals and Mechanosensing in Bacterial Responses to Their Environment. PLOS Pathog. 2015;11:e1005057.

[39] Haswell ES, Phillips R, Rees DC. Mechanosensitive channels: what can they do and how do they do it? Structure. 2011;19:1356-69.

[40] Chen Y, Harapanahalli AK, Busscher HJ, Norde W, van der Mei HC. Nanoscale cell wall deformation impacts long-range bacterial adhesion forces on surfaces. Appl Environ Microbiol. 2014;80:637-43.

[41] Jenal U, Reinders A, Lori C. Cyclic di-GMP: second messenger extraordinaire. Nat Rev Microbiol. 2017;15:271.

[42] Baker AE, O'Toole GA. Bacteria, Rev Your Engines: Stator Dynamics Regulate Flagellar Motility. J Bacteriol. 2017;199:e00088-17.

[43] Berne C, Ellison CK, Ducret A, Brun YV. Bacterial adhesion at the single-cell level. Nat Rev Microbiol. 2018;16:616-27.

[44] Jain R, Kazmierczak BI. Should I Stay or Should I Go? *Pseudomonas* Just Can't Decide. Cell host & microbe. 2019;25:5-7.

[45] Boehm A, Kaiser M, Li H, Spangler C, Kasper CA, Ackermann M, et al. Second messenger-mediated adjustment of bacterial swimming velocity. Cell. 2010;141:107-16.

[46] Wang R, Wang F, He R, Zhang R, Yuan J. The Second Messenger c-di-GMP Adjusts Motility and Promotes Surface Aggregation of Bacteria. Biophys J. 2018;115:2242-9.

[47] Toutain CM, Caizza NC, Zegans ME, O'Toole GA. Roles for flagellar stators in biofilm formation by *Pseudomonas aeruginosa*. Res Microbiol. 2007;158:471-7.

[48] Cairns LS, Marlow VL, Bissett E, Ostrowski A, Stanley-Wall NR. A mechanical signal transmitted by the flagellum controls signalling in *Bacillus subtilis*. Mol Microbiol. 2013;90:6-21.

[49] Aizawa SI. Flagella. In: Brenner S, Miller JH, editors. Encyclopedia of Genetics. New York: Academic Press; 2001. p. 711-2.

[50] Lele PP, Hosu BG, Berg HC. Dynamics of mechanosensing in the bacterial flagellar motor. Proc Natl Acad Sci. 2013;110:11839-44.

[51] Tipping MJ, Delalez NJ, Lim R, Berry RM, Armitage JP. Load-Dependent Assembly of the Bacterial Flagellar Motor. mBio. 2013;4:e00551-13.

[52] Zhu S, Kumar A, Kojima S, Homma M. FliL associates with the stator to support torque generation of the sodium-driven polar flagellar motor of *Vibrio*. Molecular microbiology. 2015;98:101-10.

[53] Terahara N, Noguchi Y, Nakamura S, Kami-ike N, Ito M, Namba K, et al. Load- and polysaccharide-dependent activation of the Na+-type MotPS stator in the *Bacillus subtilis* flagellar motor. Sci Rep. 2017;7:46081.

[54] Nord AL, Gachon E, Perez-Carrasco R, Nirody JA, Barducci A, Berry RM, et al. Catch bond drives stator mechanosensitivity in the bacterial flagellar motor. Proceedings of the National Academy of Sciences of the United States of America. 2017;114:12952-7.

[55] Suzuki Y, Morimoto YV, Oono K, Hayashi F, Oosawa K, Kudo S, et al. Effect of the MotA(M206I) Mutation on Torque Generation and Stator Assembly in the *Salmonella* H+ Driven Flagellar Motor. J Bacteriol. 2019;201:e00727-18.

[56] Wadhwa N, Phillips R, Berg HC. Torque-dependent remodeling of the bacterial flagellar motor. Proc Natl Acad Sci USA. 2019.

[57] Baker AE, Webster SS, Diepold A, Kuchma SL, Bordeleau E, Armitage JP, et al. Flagellar stators stimulate c-di-GMP production by *Pseudomonas aeruginosa*. J Bacteriol. 2019:JB.00741-18.

[58] Van Dellen KL, Houot L, Watnick PI. Genetic analysis of *Vibrio cholerae* monolayer formation reveals a key role for DeltaPsi in the transition to permanent attachment. J Bacteriol. 2008;190:8185-96.

[59] Leake MC, Chandler JH, Wadhams GH, Bai F, Berry RM, Armitage JP. Stoichiometry and turnover in single, functioning membrane protein complexes. Nature. 2006;443:355.

[60] Beeby M, Ribardo DA, Brennan CA, Ruby EG, Jensen GJ, Hendrixson DR. Diverse high-torque bacterial flagellar motors assemble wider stator rings using a conserved protein scaffold. Proc Natl Acad Sci USA. 2016;113:E1917-26.

[61] Blair DF, Berg HC. Restoration of torque in defective flagellar motors. Science. 1988;242:1678-81.

[62] Block SM, Berg HC. Successive incorporation of force-generating units in the bacterial rotary motor. Nature. 1984;309:470-2.

[63] Tala L, Fineberg A, Kukura P, Persat A. Pseudomonas aeruginosa orchestrates twitching motility by sequential control of type IV pili movements. Nat Microbiol. 2019;4:774-80.

[64] Hoffman MD, Zucker LI, Brown PJB, Kysela DT, Brun YV, Jacobson SC. Timescales and Frequencies of Reversible and Irreversible Adhesion Events of Single Bacterial Cells. Anal Chem. 2015;87:12032-9.

[65] Utada AS, Bennett RR, Fong JCN, Gibiansky ML, Yildiz FH, Golestanian R, et al. *Vibrio cholerae* use pili and flagella synergistically to effect motility switching and conditional surface attachment. Nat Commun. 2014;5:4913.

[66] Persat A, Inclan YF, Engel JN, Stone HA, Gitai Z. Type IV pili mechanochemically regulate virulence factors in *Pseudomonas aeruginosa*. Proc Nat Acad Sci. 2015;112:7563-8.

[67] Siryaporn A, Kuchma SL, O'Toole GA, Gitai Z. Surface attachment induces *Pseudomonas aeruginosa* virulence. Proc Natl Acad Sci. 2014;111:16860-5.

[68] Lee CK, de Anda J, Baker AE, Bennett RR, Luo Y, Lee EY, et al. Multigenerational memory and adaptive adhesion in early bacterial biofilm communities. Proc Natl Acad Sci USA. 2018;115:4471-6.

[69] Ellison CK, Kan J, Dillard RS, Kysela DT, Ducret A, Berne C, et al. Obstruction of pilus retraction stimulates bacterial surface sensing. Science. 2017;358:535-8.

[70] Inclan YF, Persat A, Greninger A, Von Dollen J, Johnson J, Krogan N, et al. A scaffold protein connects type IV pili with the Chp chemosensory system to mediate activation of virulence signaling in *Pseudomonas aeruginosa*. Mol Microbiol. 2016;101:590-605.

[71] Li G, Brown PJ, Tang JX, Xu J, Quardokus EM, Fuqua C, et al. Surface contact stimulates the just-in-time deployment of bacterial adhesins. Mol Microbiol. 2012;83:41-51.

[72] Levi A, Jenal U. Holdfast formation in motile swarmer cells optimizes surface attachment during *Caulobacter crescentus* development. J Bacteriol. 2006;188:5315-8.

[73] Hug I, Deshpande S, Sprecher KS, Pfohl T, Jenal U. Second messenger–mediated tactile response by a bacterial rotary motor. Science. 2017;358:531-4.

[74] Kazmierczak BI, Schniederberend M, Jain R. Cross-regulation of *Pseudomonas* motility systems: the intimate relationship between flagella, pili and virulence. Curr Opin Microbiol. 2015;28:78-82.

[75] Otto K, Silhavy TJ. Surface sensing and adhesion of *Escherichia coli* controlled by the Cpx-signaling pathway. Proc Natl Acad Sci. 2002;99:2287-92.

[76] Raivio TL, Silhavy TJ. Periplasmic stress and ECF sigma factors. Annu Rev Microbiol. 2001;55:591-624.

[77] Herbert EE, Cowles KN, Goodrich-Blair H. CpxRA regulates mutualism and pathogenesis in *Xenorhabdus nematophila*. Appl Environ Microbiol. 2007;73:7826-36.

[78] Duguay AR, Silhavy TJ. Quality control in the bacterial periplasm. Biochimica et Biophysica Acta (BBA)-Mol Cell Res 2004;1694:121-34.

[79] Raivio TL. MicroReview: Envelope stress responses and Gram-negative bacterial pathogenesis. Mol Microbiol. 2005;56:1119-28.

[80] Kimkes TEP, Heinemann M. Reassessing the role of the *Escherichia coli* CpxAR system in sensing surface contact. PLoS One. 2018;13:e0207181.

[81] Wall E, Majdalani N, Gottesman S. The Complex Rcs Regulatory Cascade. Annu Rev Microbiol. 2018;72:111-39.

[82] Rodesney CA, Roman B, Dhamani N, Cooley BJ, Katira P, Touhami A, et al. Mechanosensing of shear by *Pseudomonas aeruginosa* leads to increased levels of the cyclic-di-GMP signal initiating biofilm development. Proc Natl Acad Sci. 2017;114:5906-11.

[83] Vigeant MA, Ford RM, Wagner M, Tamm LK. Reversible and irreversible adhesion of motile *Escherichia coli* cells analyzed by total internal reflection aqueous fluorescence microscopy. Appl Environ Microbiol. 2002;68:2794-801.

[84] Smith LV, Tamm LK, Ford RM. Explaining non-zero separation distances between attached bacteria and surfaces measured by total internal reflection aqueous fluorescence microscopy. Langmuir. 2002;18:5247-55.

[85] Tu Y, Shimizu TS, Berg HC. Modeling the chemotactic response of *Escherichia coli* to time-varying stimuli. Proc Natl Acad Sci. 2008;105:14855.

[86] Sourjik V, Berg HC. Functional interactions between receptors in bacterial chemotaxis. Nature. 2004;428:437-41.

[87] Naismith JH, Booth IR. Bacterial Mechanosensitive Channels—MscS: Evolution's Solution to Creating Sensitivity in Function. Ann Rev Biophys. 2012;41:157-77.

[88] Perozo E, Kloda A, Cortes DM, Martinac B. Physical principles underlying the transduction of bilayer deformation forces during mechanosensitive channel gating. Nat Struct Mol Biol. 2002;9:696.

[89] Wingreen NS, Huang KC. Physics of Intracellular Organization in Bacteria. Ann Rev Microbiol. 2015;69:361-79.

[90] Tuson HH, Auer GK, Renner LD, Hasebe M, Tropini C, Salick M, et al. Measuring the stiffness of bacterial cells from growth rates in hydrogels of tunable elasticity. Mol Microbiol. 2012;84:874-91.

[91] Yao X, Jericho M, Pink D, Beveridge T. Thickness and elasticity of gram-negative murein sacculi measured by atomic force microscopy. J Bacteriol. 1999;181:6865-75.

[92] Wang B, Zhang R, Yuan J. Limiting (zero-load) speed of the rotary motor of *Escherichia coli* is independent of the number of torque-generating units. Proc Natl Acad Sci USA. 2017;114:12478-82.

[93] Laventie BJ, Sangermani M, Estermann F, Manfredi P, Planes R, Hug I, et al. A Surface-Induced Asymmetric Program Promotes Tissue Colonization by *Pseudomonas aeruginosa*. Cell host & microbe. 2019;25:140-52.e6.

[94] Brinton Jr CC. The Structure, Function, Synthesis & Geneticc Control of Bacterial Pili & A Molecular Model for DNA & RNA Transport in Gram Negative Bacteria*. Transact N Y Acad Sci. 1965;27:1003-54.

[95] Thomas WE, Trintchina E, Forero M, Vogel V, Sokurenko EV. Bacterial adhesion to target cells enhanced by shear force. Cell. 2002;109:913-23.

[96] Le Trong I, Aprikian P, Kidd BA, Forero-Shelton M, Tchesnokova V, Rajagopal P, et al. Structural basis for mechanical force regulation of the adhesin FimH via finger trap-like beta sheet twisting. Cell. 2010;141:645-55.

[97] Sanfilippo JE, Lorestani A, Koch MD, Bratton BP, Siryaporn A, Stone HA, et al. Microfluidic-based transcriptomics reveal force-independent bacterial rheosensing. Nat Microbiol. 2019.

[98] Chen I, Dubnau D. DNA uptake during bacterial transformation. Nat Rev Microbiol. 2004;2:241-9.

[99] Murray EJ, Kiley TB, Stanley-Wall NR. A pivotal role for the response regulator DegU in controlling multicellular behaviour. Microbiology. 2009;155:1-8.

[100] Chan JM, Guttenplan SB, Kearns DB. Defects in the flagellar motor increase synthesis of poly-γ-glutamate in *Bacillus subtilis*. J Bacteriol. 2014;196:740-53.

[101] Ortega Arroyo J, Cole D, Kukura P. Interferometric scattering microscopy and its combination with single-molecule fluorescence imaging. Nat Protoc. 2016;11:617-33.

[102] Chawla R, Gupta R, Lele TP, Lele, PP. A skeptic's guide to bacterial mechanosensing. Journal of Molecular Biology, 2019. Article reference: 66263, doi.org/10.1016/j.jmb.2019.09.004

3. TORQUE REGULATES MECHANOSENSITIVE FLAGELLAR MOTOR FUNCTION*

3.1. Background

The bacterial flagellar motor consists of a membrane-embedded stator and a transmembrane rotor. The stator is responsible for surface-sensing, an ability that likely helps initiate biochemical signaling. It remodels in response to perturbations in viscous loads, recruiting more units as the load increases. Here, we tested a hypothesis that the amount of torque generated by each unit modulates its binding to the rotor. We measured remodeling in strains lacking FliL, a membrane protein that is believed to be important in stabilizing motor torque. Measurements revealed that the torque as well as stator-rotor association in *fliL* mutants was comparable to that in wild-type cells. On the other hand, the association was weaker in paralyzed motors that were unable to generate torque, consistent with our hypothesis. An analytical binding model that incorporated an exponential dependence of the stator dissociation rate on the amount of force delivered to the rotor was able to provide accurate fits to the measurements of stator-rotor binding over a wide range of loads. Based on these results, we propose that the binding of each unit to the motor is enhanced by the force it develops. We further conclude that FliL does not play a significant role in motor function in *E. coli*.

---

*Adapted with modifications from "Torque, but not FliL, regulates mechanosensitive flagellar function" by R. Chawla, K.M. Ford, P.P. Lele, 2017. Scientific Reports, 7, Article number: 5565,

The flagellar motor is able to undergo structural and functional modifications in response to long-lived perturbations in thermal [1,2], chemical [3-7] , electrical [8,9], and mechanical [10-14] environments. Structural remodeling improves the odds of survival; for example, remodeling of rotor complexes enables motor-level adaptation that extends the range of signal detection during chemotaxis [5,7]. In *Escherichia coli*, the motor is rotated by a set of stator units consisting of two proteins, MotA and MotB, that utilize the proton motive force (pmf) to deliver torque to the rotor [15]. In previous work, we showed that the stators are mechanosensitive and adapt the motor to dramatic changes in viscous loads [10]. Adaptation is facilitated by stator remodeling, enabling the motor to retain a higher number of stator units under high viscous loads [10,11,13]. Stator remodeling modulates motor torque, which is likely to be advantageous for swimmers that find themselves in high-viscosity environments or for swarmers that need to overcome higher shear when swarming on substrates. The ability of the motor to sense and adapt to mechanical signals makes it one of the clearest examples of a mechanosensitive biological motor [10,16].

The role of the mechanosensitive motor in surface sensing and triggering of biochemical pathways is of significant interest [17-20], but the mechanisms underlying its response to mechanical signals remain unclear. Previously, we proposed a mechanism for remodeling that was torque dependent [10] – the torque generated by individual stator units modulates the accessibility of cryptic binding sites, thereby controlling the binding affinity to the motor. Higher torque stabilizes the association, whereas lower torque results in weaker stator-rotor association. According to such a mechanism, any degradation in torque generated by individual units is expected to weaken its association with the rotor.

To test the hypothesis, we measured stator binding under conditions in which torque was anticipated to be weak or negligible. Recent work suggested that FliL, a membrane-associated 17 kDa protein [21] , stabilizes the torque generated by the stators as well as the chemotactic response at high loads in *E. coli* and *S. enterica* [22]. However, these findings are at odds with earlier reports by the Macnab group that suggested that FliL does not regulate chemotaxis and motility in *E. coli* [23]. Nonetheless, several other species have been observed to be deficient in swimming (under high loads) and swarming when lacking FliL, presumably because the motors fail to deliver adequate torque at high loads [24-26]. Hence, we measured torque and stator-binding in a strain of *E. coli* lacking FliL. Our observations indicated that the loss of FliL did not significantly affect motor torque over a wide range of loads. Consistent with our hypothesis, stator-rotor association was not affected either. Furthermore, these mutants swarmed, in agreement with recent reports [27]. Next, we worked with strains carrying paralyzed stators that were unable to develop torque, as a result of which tethered cells remained predominantly locked. In these strains, stators exhibited weaker association with the rotor lending support to the notion that remodeling is regulated by absolute torque. An analytical model was developed that explained load-dependent stator remodeling by incorporating an exponential dependence of the stator-unit's off-rate constant on the amount of force delivered to the rotor. The model was able to fit accurately the dependence of stator binding on viscous loads measured by Tipping and co-workers [11]. Our results suggest that a torque-dependent mechanism likely underlies mechanosensitive remodeling of the motor and emphasize the indispensable role of remodeling in swarming.

3.2. Results

3.2.1. FliL and Torque at High Loads

Employing the tethered-cell assay, we determined the torque developed by individual motors at near-stall viscous loads in the *fliL* and wildtype strains. Cells were tethered to the glass surface via the filaments and were observed to rotate at constant speeds several minutes after tethering (*Materials and Methods*). The cells switched between clockwise (CW) and counterclockwise (CCW) directions of rotation. A subset of the total data that had a narrow distribution of cell length was selected for further analysis (mean *fliL* mutant cell length = 2.28±0.44 μm and wild-type control cell length = 2.40±0.26 μm). The rotational speeds of motors in the *fliL* strain are shown in Figure 3-1A, for both directions. The corresponding wild-type motor speeds are also indicated. The flagellar motor generates nearly constant torque at high loads and, as a consequence, its speed decreases with increasing load [28]. Consistent with this, speeds were observed to decrease with increasing cell lengths (Figure 3-1). The motors in the two strains exhibited similar speed versus cell-length characteristics in either direction, and the differences in the mean motor speeds were not significant (p-value > 0.05, Figure 3-1A). To compare the torque generated in the two strains, we first calculated the torque developed by each motor in the *fliL* strain by taking into account the size of the cell (see *Materials and Methods*). Individual torque was then normalized by the mean torque generated by wild-type motors. The normalized torque over a range of speeds is indicated in Fig 1B, for both directions. The mean normalized values were 1.09 ± 0.06 (CCW) and 1.03 ± 0.06 (CW).

We concluded from these results that the absence of FliL did not adversely affect the torque developed by flagellar motors at near-stall loads.

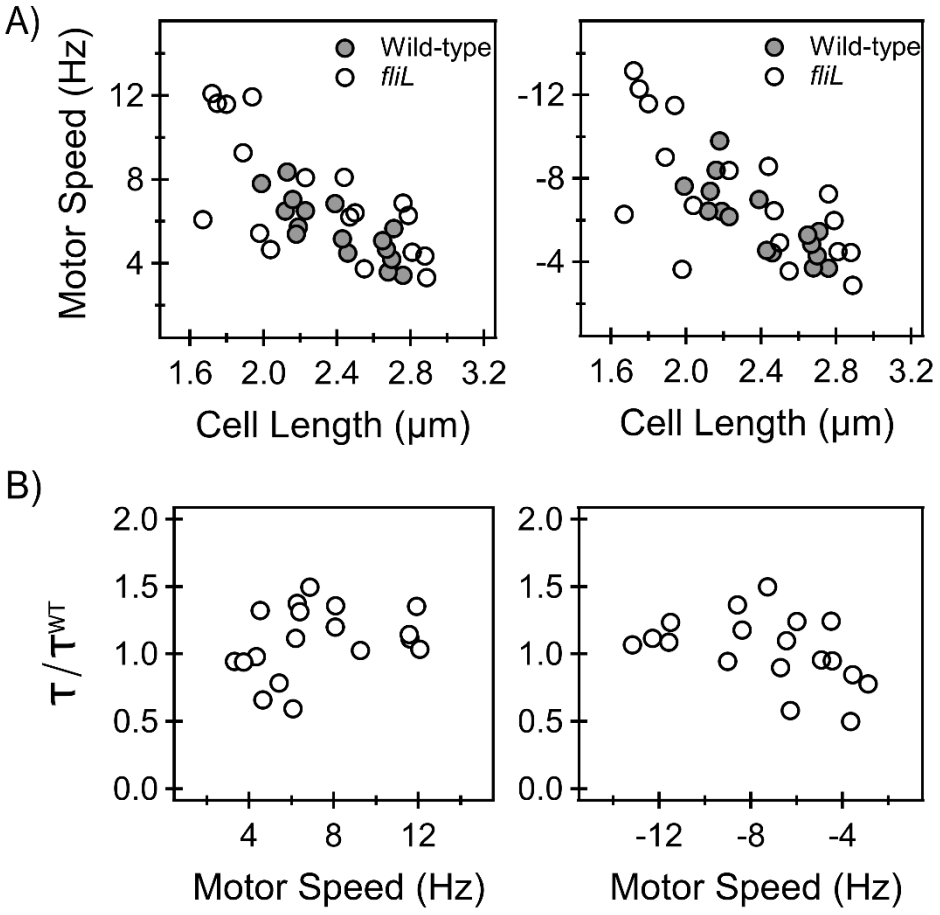

Figure 3-1 Comparison of motor performance *fliL* mutant with wild-type under high-load conditions. A) *Steady-state speed versus length:* The rotational speeds and cell-length in the *fliL* (open circles, n=18 motors) and wild-type (filled gray circles, n=16 motors) strains are indicated. The left panel indicates speeds in the CCW direction and the right panel indicates speeds in the CW direction. The mean CCW speeds were 5.65 ± 1.44 Hz (wild-type strain) and 7.24 ± 2.93 Hz (*fliL* strain). The mean CW speeds were 5.96 ± 1.75 Hz (wild-type strain) and 7.28 ± 3.19 Hz (*fliL* strain). Differences in the mean speeds were not significant (p-value > 0.05) between the two strains. B) *Torque versus speed*: Torque generated by motors in the *fliL* mutant was calculated from mean rotational-speed and cell-geometry. The left and right panels indicate the CCW and CW data respectively. τ represents the torque generated by individual motors in the *fliL* strain and τ^{WT} represents the mean torque generated by motors in the wild-type strain. Reprinted with permission from Chawla et al, 2017 [45].

3.2.2. Stator-Rotor Association and Torque

fliL strains

Since torque was not deficient at high loads in the absence of FliL, we tested whether stator-rotor binding remained unchanged as well. The rotational speed (Figure 3-1A) depends not only on the torque developed by individual units within the stator complex but also on the number of units bound to the rotor. To determine the number of bound stator-units, we applied step increments in viscous loads on individual motors by allowing cells to tether and recorded their rotation following the onset of tethering [10]. The response of a representative *fliL* motor is shown in Figure 3-2A. The motor initially rotated at a low speed. Over the next hundred seconds, the speed increased in a step-wise fashion to reach a maximum value (~12.75 Hz). The adaptation in speed is consistent with our observations with wild-type motors (data not shown) and is indicative of stator-remodeling. This confirmed our previous result that flagellar mechanosensing is independent of FliL [10].

At very low loads, stators deliver a small amount of torque (~ 10 pN-nm), and the number of bound units at these loads has been observed to be ~ 1-2 units in wildtype motors [10]. To estimate the number of stator units in *fliL* motors at very low loads, we employed a step-finding algorithm and calculated the mean speed at each step in the speed data [10]. Next, we identified the initial speeds at which the *fliL* motors rotated (indicated by the 1st step in the inset in Figure 3-2A). Based on these speeds and the cell-geometry, the initial torque generated (τ_{ini}) was determined for each motor. The torque values were normalized by the mean torque generated by single-units in wildtype cells (τ^{WT}_{1}). The

normalized torque data (n = 17 motors) are shown in Figure 3-2B as a function of speed and can be approximately placed into two groups. The first group in the lower left corner represents motors that initially carried single units (τ_{ini} / τ^{WT}_{1} ~ 1). and the second group, on the upper right corner, represents motors that carried two units (τ_{ini} / τ^{WT}_{1} ~ 2). Since the load on the motor prior to tethering is very low, this indicated that motors in *fliL* mutants employ no more than 1-2 stator-units at very low loads, similar to the wild-type cells [10].

To measure stator-rotor association at high loads, we obtained the mean step increment in speed for each motor from the adaptation data. Dividing the final speed attained by the motor by the step size enabled us to estimate the number of units bound to each rotor upon the completion of remodeling. This approach is appropriate because at high loads, each new unit that binds to the motor has been shown to contribute equivalent torque as its predecessors [29]. Calculations indicated that the mean number of stator units engaged by the motors at high loads in the *fliL* mutant was 8.7 ± 3.0, similar to the wildtype (9.1 ± 1.87). Thus, the lack of FliL had little effect on the stator-rotor association.

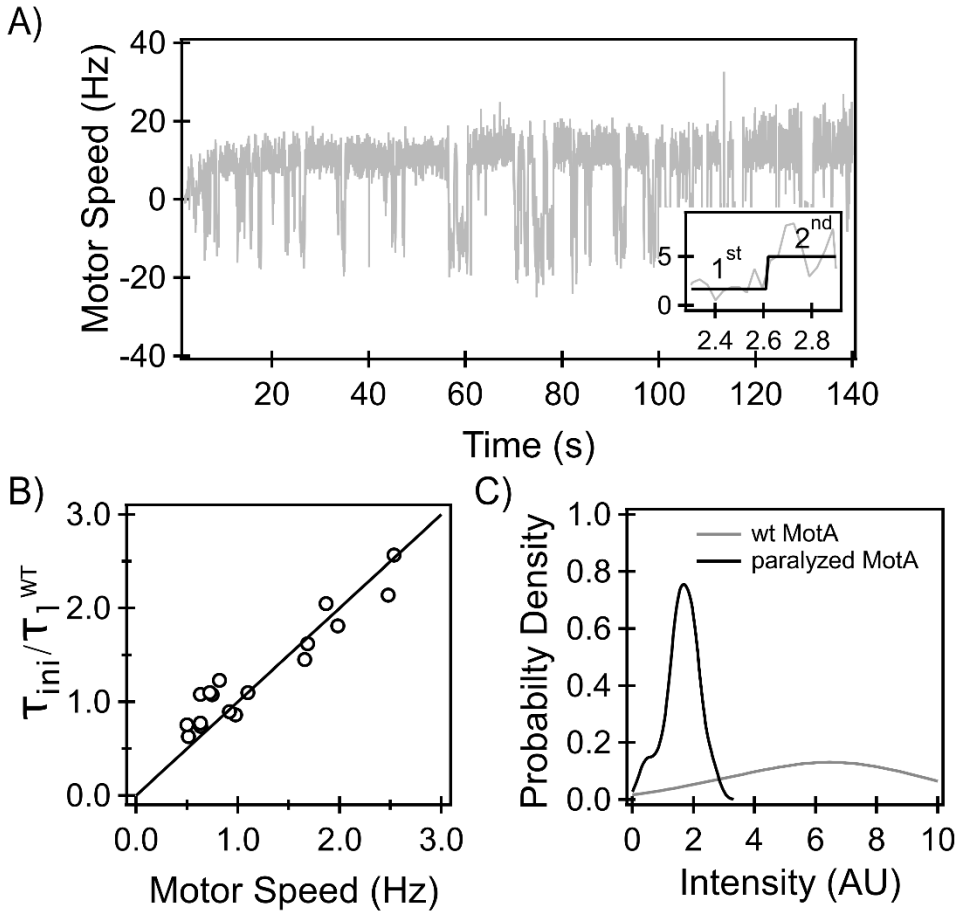

Figure 3-2 Adaptive remodeling to mechanical stimulus. A) *Response to mechanical stimulus:* The adaptive response of the stator to mechanical stimulus in a representative *fliL* motor is visible from the step-wise increments in speeds over time. Inset shows the response of the motor (gray) over the first few seconds and the black line is the output of the step-finding algorithm, indicating the 1st and the 2nd step. B) *Stator-binding:* Initial torque developed by *fliL* motors (τ_{ini}) normalized by the average torque developed by single units ($\tau^{WT}{}_1$) in wildtype tethered cells [10]. Torque was determined from the cell-geometry and the initial speed (inset Fig 2A). The data near the lower left corner corresponds to 1 unit ($\tau/\tau^{WT}{}_1 \sim 1$) and the data near the upper right corner represents two units ($\tau/\tau^{WT}{}_1 \sim 2$). C) *Remodeling in paralyzed motors:* Distributions inferred from stator-intensity measurements in paralyzed motors (black) and functional motors (gray) are shown. The mean values were 1.5 ± 0.14 a.u. (paralyzed) and 4.63 ± 0.4 a.u. (wildtype). The difference in means was highly significant (p-value < 0.01). Reprinted with permission from Chawla et al, 2017 [45].

Paralyzed motors

To test whether a full complement of stators could assemble around the rotor when the torque is degraded, we employed a strain that carried chromosomal *eyfp-motB* and a point mutation in *motA* that resulted in paralyzed motors [30]. In these motors, the paralyzed stator binds to the rotor [30] but cannot generate torque, causing tethered cells to remain predominantly locked. Cells were tethered, and fluorescently labeled stators associated with the motors were imaged via TIRF after ~ 600 seconds. The intensities of the motor-bound stators was quantitatively determined using previous protocols [6]. The kernel density estimates of intensities in the paralyzed strain are shown in Figure 3-2C. The corresponding intensities of wild-type motors with functioning-units are also indicated. The raw data have been included in the Appendix B (Figure B1). The difference in the mean intensities was highly significant (p-value < 0.01, Figure 3-2C). Evidently, functional units bound to the motor in higher numbers than the paralyzed units. The mean intensity in wild-type motors was ~ 3 times higher than the mean intensity in paralyzed motors. A functional stator unit generates a significant amount of torque (~100-200 pN-nm) in a tethered cell. On the other hand, in paralyzed strains the stators do not generate a torque. Therefore, these measurements support the hypothesis that torque regulates binding of the stator units to the rotor.

FliL and Torque over a Range of Loads

To determine if FliL affected motor-function at viscous loads other than near-stall conditions, we measured torque in *fliL* strains over a range of loads. Hydrodynamic

screening near solid substrates ensures that the viscous loads (ζ) on motors in swarmer cells are higher than the viscous loads on motors in swimmer cells. Hence, we first tested motor performance at swimming loads ($\zeta_{swimming}$). Wild-type motors at these loads typically rotate at ~165-175 Hz [31]. To determine if the *fliL* mutants exhibited subnormal motor torques at $\zeta_{swimming}$, we compared swimming speeds in wild-type and *fliL* strains in liquid growth media. The motion of swimming cells was recorded and speeds were quantitatively determined as discussed in *Methods and Materials.* Unbiased kernel density estimates of speeds obtained from our measurements are shown in Figure 3-3A for the wild-type and *fliL* strains. The difference in the mean swimming speed was significant (p-value < 0.05, Figure 3-3A). Assuming a similar number of flagella per cell in the *fliL* and the wild-type strains, the torque generated by motors in the *fliL* strain was estimated to be ~ 90% of the torque generated by wild-type motors.

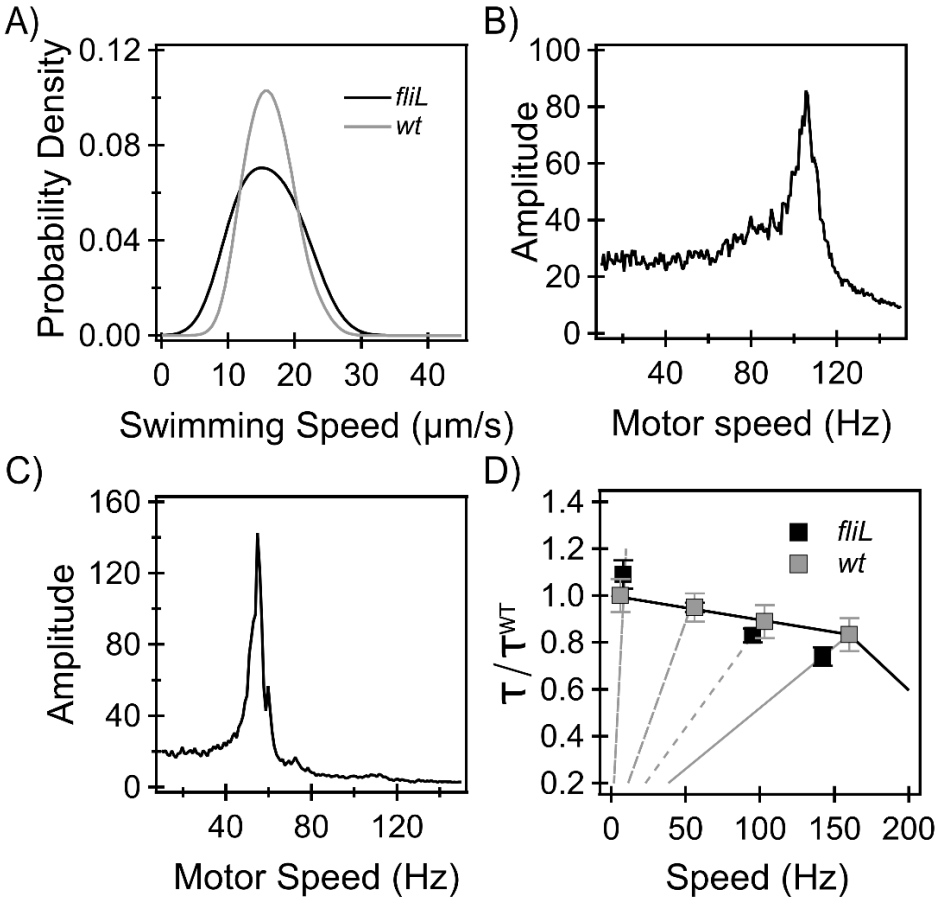

Figure 3-3 BFM response to a range of viscous loads. A) *Swimming speeds*: Kernel density estimates of swimming speeds in *fliL* (black) and wildtype (gray) strains. The difference in the mean swimming speeds was significant (p-value < 0.05). The mean swimming speed in the wild-type strain was 20% higher than that in the *fliL* strain. B) and C) *Tethered beads:* Signals from representative *fliL* motors, one rotating a 750 nm and another rotating a 1 μm bead. Peaks correspond to ~106 Hz and ~ 55 Hz, respectively. D) *Torque-speed curve:* The average torque generated by motors in the *fliL* strain (black symbols) and in the wild-type strain (gray symbols) is plotted against the average motor speed. The torque-values (τ) have been normalized by the maximum torque (τ^{WT}) measured in wild-type tethered cells. Reprinted with permission from Chawla et al, 2017 [45].

Motors were subjected to higher loads by tethering them to beads of different sizes. Single-motor rotation was measured with a photomultiplier setup that enabled high-speed tracking of bead rotation [32]. The photomultiplier-output signals were sinusoidal, each

wave corresponding to one full turn of the motor. Power spectral densities (PSD) were calculated from the output signals to obtain the rotational speed. Representative PSDs for a *fliL* motor rotating a 750 nm bead and another motor rotating a 1 μm bead are shown in Fig 3B and 3C, respectively. The peaks were sharp, indicating a good signal-to-noise ratio and enabling us to determine accurately the frequency of rotation. For wild-type motors, our measurements yielded mean speeds of ~ 47 ± 6 Hz (1 μm, 14 motors) and ~ 103 ± 25 Hz (750 nm, 15 motors), similar to earlier measurements with the wild-type strain [28]. The mean speeds for the *fliL* strain were ~ 51 ± 11 (1 μm, 15 motors) and ~ 95 ± 11 Hz (750 nm, 13 motors). A non-parametric statistical test revealed that the differences in means between the two strains were insignificant (p-value > 0.05).

The average torque was then determined for all the viscous loads used in this work (*Materials and Methods*). A comparison of the motor torque vs speed curve for the *fliL* and wild-type strains is shown in Figure 3-3D. The differences between the two curves were minor, suggesting that the absence of FliL does not significantly affect torque generation or stator-rotor association over a wide-range of loads.

Swarming in *fliL* strains

FliL has been reported to be crucial for bacterial swarming in a variety of species. We carried out measurements to test whether FliL had a measurable impact on the switch function, which in turn could affect swarming. This was done by determining the CW_{bias} (probability of CW rotation) and motor reversal frequencies. As indicated in Figure 3-4A, the mean CW_{bias} was not appreciably different in the two strains (p-value > 0.05). The difference between the mean reversal frequencies was negligible as well (p-value > 0.05).

Motor-switching is indispensable for swarming, [33] and considering that the switch function was not affected in the *fliL* strain, we tested whether the loss of FliL indeed prevented *E. coli* from swarming. Figure 3-4C shows a representative image of a swarm plate inoculated with the *fliL* strain in the environmental chamber (*Methods and Materials*). As is evident, the loss of FliL did not inhibit swarming. This was further confirmed by imaging swarming under phase microscopy with a 40x, ph3 objective. The results were reproducible (swarm diameter = 4.06 ± 1.13 cm over 8 hour incubation, 10 plates).

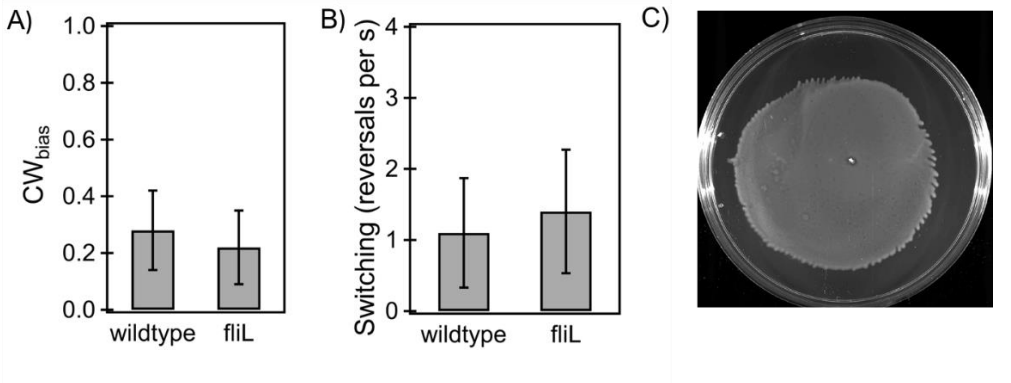

Figure 3-4 Switching behavior of the strains. A) *Probability of CW rotation.* The mean CW_{bias} was 0.28 ± 0.03 (n = 16 motors) in wild-type motors and 0.22 ± 0.03 (n = 18 motors) in *fliL* motors. The difference in the means was not significant (p-value > 0.05). B) *Switching-frequencies*: The mean reversal frequency was 1.1 ± 0.77 per second in wild-type motors and 1.4 ± 0.87 per second in *fliL* motors. The difference in the means was not significant (p-value > 0.05). C) *Swarming*: A representative swarm-plate with the *fliL* mutant. The average swarm diameter was 4.05 ± 1.13 cm, n = 10 plates (8-hour incubation). Reprinted with permission from Chawla et al, 2017 [45].

3.2.3. Model for mechanosensitive stator-remodeling

Stator units that are a part of a functioning stator complex have been shown to continually exchange with freely diffusing units in the cell membrane [34]. According to our

hypothesis, the number of stator-units associated with each motor varies with the amount of torque developed by each unit. To explain the dependence of stator binding on torque, we assumed that the dissociation rate constant (k_{off}) is a function of the force applied by each unit on the rotor, F, whereas the on-rate (k_{on}) is constant. The stator-exchange kinetics can be represented in a straightforward manner as follows:

$$\frac{dn}{dt} = k_{on}UB - k_{off}(F)n \quad (1)$$

Here, n represents the number of bound units (or occupied sites) and B represents the number of vacant binding sites. U is the total number of units available in the cell and remains more or less constant. At steady state (s.s), the total available binding sites B_T (= B_{ss} + n_{ss}) and the number of bound units are related by:

$$\frac{n_{ss}}{B_T} = \frac{1}{1+k_{off}(F)/k_{on}U} \quad (2)$$

We assumed that k_{off} depends exponentially on force similar to the Bell model for slip-bonds [35], although with a negative sign in the exponent, such that $k_{off} = k_{off}^0 exp(-F\delta/k_BT)$, where k_{off}^0 is the off-rate constant at zero force and δ is the characteristic bond length.

$$\frac{n_{ss}}{B_T} = \frac{1}{1+\varphi exp(-F\delta/k_BT)} \quad (3)$$

Here, $\varphi = \left({k_{off}}^0/k_{on}U\right)$. We constrained $1/\varphi$ ~ 0.01 – 1 based on prior estimates with other motor-associated proteins [6]. The amount of force generated by each unit, F, is known to increase with load and was assumed to decrease linearly with rotation speed.

$$F = F_{max}\left(1 - \frac{v}{v_{max}}\right) \quad (4)$$

F_{max} is the maximum force (at near-stall conditions) that a single unit can apply on a rotor with a radius r = 22.5 nm. More-accurate, non-linear models are available elsewhere[36,37].

From prior measurements, v_{max} = 300 Hz[38]. Also, $F_{max} = \tau_{max} /(n_{ss}\, r)$ and τ_{max} is the total stall-torque applied by a full complement of stator-units [29]. The dependence of motor-speed on viscous load ($\tau = \zeta\, v$) was estimated from the experimentally measured torque-speed relationships[28,29].

Equations 3 and 4 were combined to yield a single analytical expression that was fitted to the measurements of stator-rotor binding over a range of viscous loads [11]. The fits to the experimental data for the CCW and CW directions are indicated in Figure 3-5. As detailed in the supplementary text, the model was linearized and fits were obtained via linear regression. The fits were excellent (Figure 3-5) and yielded characteristic lengths of $\delta \sim$ 2.48 nm (CCW) and $\delta \sim$ 2.65 nm (CW). These lengths are equal to approximately half the size of a single step of the rotor and provide a measure of the distance over which force F acts during stepping to modulate binding. Thus, the simple model provided excellent fits and matched the shape of the non-linear experimental data reasonably well, providing further support to the torque hypothesis.

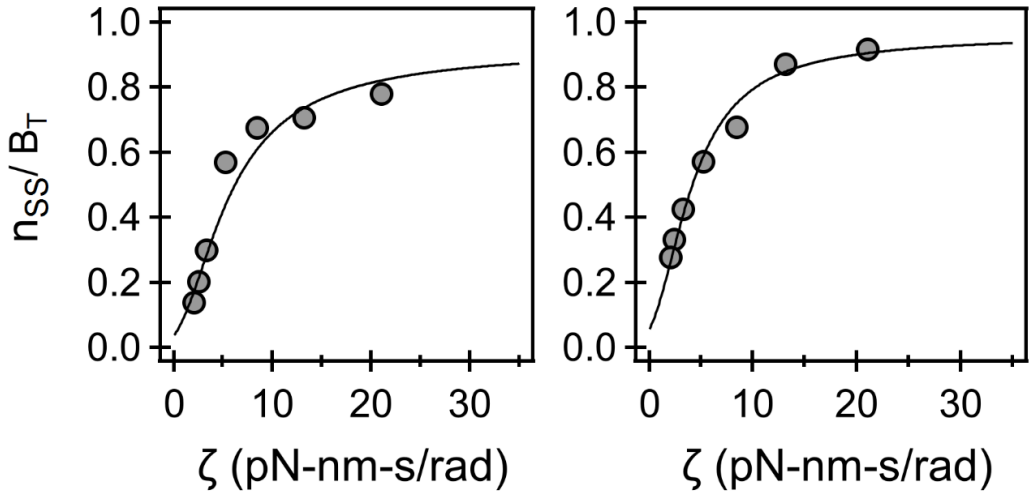

Figure 3-5 Model for mechanosensitive-remodeling. *Experiments versus analytical model.* The measurements of stator binding to motors over a range of loads are indicated by symbols for the CCW (left-panel) and the CW (right-panel) directions [11]. The model-fit is indicated by the curve. For the CCW direction, $1/\varphi \sim 0.053$ and $\delta = 2.48$ nm and for the CW direction, $1/\varphi \sim 0.035$ and $\delta = 2.65$ nm. The values of the coefficient of determination (R^2) were 0.95 (CCW) and 0.99 (CW). Reprinted with permission from Chawla et al, 2017 [45].

3.3. Discussion

Several studies have shown that the motor is highly dynamic - it remodels component complexes to adapt its function in response to a variety of stimuli [1-14]. The stator-complex is the mechanosensitive part of the flagellar motor and it responds to mechanical stimuli by remodeling. A sudden and significant increase in the load on a motor that is rotated by a single unit results in a drop in the flux of protons through the unit as well as the rotational speed. Simultaneously, the stator-unit increases the amount of force delivered from < 1 pN to ~ 5-15 pN. It is less likely that a change in the flux of protons or the drop in rotational speeds is the signal for remodeling. This is because a

disruption in the pmf, which reduces speeds as well as flux, has been observed to result in the disassembly, rather than the assembly, of stator units, at high loads [8,9].

In this work, we have tested the notion that torque regulates stator binding to the rotor [10]. It is likely that each stator unit carries cryptic binding sites that typically remain inaccessible when the unit delivers a low torque (at very low loads). However, when the unit delivers a high torque (at high loads), these sites become accessible due to the development of high tensile forces during a power stroke. In such a mechanism, higher torque strengthens the stator-rotor association, leading to stator remodeling. We tested this idea by measuring stator binding in mutants in which torque was anticipated to be weak or negligible at high loads. Our measurements indicated that the binding was unaffected by the absence of FliL, consistent with measurements that showed no reduction in torque in the *fliL* strain. On the other hand, stator-binding to the rotor was reduced in the paralyzed *motA* strain compared to the wildtype strain. An analytical model was developed that incorporated an exponential dependence of the stator unit's dissociation rate constant on the force generated by that unit. The model provided accurate fits to the available experimental data, and suggested a characteristic bond length (δ) that was ~ half the size of a rotor-step. It would be interesting to determine if there is a correspondence between δ and the length of single-steps in the motor. Specifically, does each unit combine the action of two half-steps to complete one full step of the rotor?

Earlier *resurrection* experiments demonstrated that the expression of functional MotA units in tethered cells of the paralyzed mutant resulted in step-wise increments in speeds [30], similar to the data in Figure 3-2A. Our data suggest that the paralyzed motors

in those resurrection experiments did not carry a full complement of paralyzed units. Therefore, the defective units did not sterically hinder the binding of newly expressed functional units. Instead, resurrection occurred because the high load, that each newly bound functional unit needed to work against, ensured that the rate of its dissociation from the rotor was slow.

In *Vibrio alignolyticus*, experiments suggest that FliL localizes with stators in the sodium-driven polar flagellum [39]. Defects in FliL result in the degradation of swimming and swarming in *Proteus mirabilis* [26]. However, in *E. coli* earlier reports suggested that FliL is not important in swimming and chemotaxis [23]. Our quantitative measurements confirmed the earlier findings and ruled out a role for FliL in any of the important motor-related functions, including torque-generation, switching and mechanosensitive remodeling at high loads. To exclude the likelihood that our observations were specific to the strains developed in our lab, we tested motor responses to high loads and swarming in *fliL* mutants (JP1297 and JP633a) obtained from the Harshey group [22]. Measurements revealed no significant differences between the mean rotation-speeds in the JP1297 and wildtype strains (Fig B2, Appendix B). In our hands, the JP633a strain was able to swarm.

3.4. Conclusions

In summary, we have experimentally tested a probable mechanism for the remodeling of stators in flagellar motors in response to mechanical stimuli. Our findings are consistent with the notion that higher torque exposes cryptic binding sites that strengthens stator-binding to the rotor. An analytical model that incorporates an exponential dependence of the stator unit's off rates on the torque delivered was able to fit previously measured load-

binding curves accurately. The combined experimental and analytical results presented here represent the first steps towards establishing a plausible mechanism for stator-mechanosensitivity and motor adaptation.

3.5. Materials and methods

3.5.1. Strains and media

The *fliL* strain (PL111) was generated by employing the λ-red mediated homologous recombination technique to delete nt 61-405 in the *fliL* gene [40]. The deletion was confirmed by sequencing. Mutations in *fliL* were previously observed to result in intergenic mutations in the *motB* region of *Rhodobacter sphaeroides* [25]. Sequencing revealed no such compensatory *motB* mutations in our strain. The paralyzed *motA* strain (PL64) was generated by exchanging the wild-type *motA* allele with a motA mutant (parent strain HCB84), in a strain carrying genomic *eyfp-motB* [10]. Strains JP1297 (Δ*fliL*, carrying the sticky *fliC* allele) and JP633a (Δ*fliL*) were obtained from the Harshey group [22]. Overnight cultures were grown from isolated colonies in 5mL of Tryptone broth (TB) and day cultures were subsequently grown (1:100 dilution) in 10 ml of fresh TB at 33^0C. After growing to an OD_{600} ~ 0.5, cells were washed in motility buffer (0.01 M Phosphate buffer, 0.067 M NaCl, 10^{-4} M EDTA, 0.01 M Sodium Lactate and 1 μM Methionine, pH ~ 7.0) before conducting motor-measurements. Swarm-agar plates (Peptone, 10g/L; NaCl, 5g/L; Beef extract, 3g/L; 0.45% Eiken Agar, 0.5% Glucose) were prepared fresh, dried after pouring for an hour at room temperature and then inoculated with the strains of interest (2 μl, overnight culture grown at 30^0C).

3.5.2. Motility Assays

Tethering: Cells were prepared for motor-assays as discussed elsewhere [32]. Standard glass flow cells were prepared by using double-sided adhesive tapes to stick two glass surfaces together. Cells were tethered via a sticky filament mutant that adheres to glass and beads [41]. Cell rotation was imaged and recorded on a Nikon microscope (Nikon Eclipse Ti-E) with a 20x phase objective at ~60 fps with a CCD camera (DCC1545M-GL, Thorlabs Inc). Bead-rotation was imaged on a Nikon Optiphot with a 60X phase objective coupled to a photomultiplier setup [32]. *Swarming:* Swarm-assays were carried out in an environmental chamber (ETS Model 5472, Electro-Tech Systems, Inc) that allowed a fine control over humidity and temperature. Swarm-plates were imaged ~ 8 hours after inoculation with a digital camera (Nikon Coolpix L330). *Swimming*: Cells were grown to an OD_{600} ~ 0.5 in TB and then diluted in fresh TB (1:40 dilution). The dilute suspension was observed in a standard flowcell and cell-motion was recorded with the Thorlabs camera at 60 fps.

3.5.3. Data Analysis

Tethered-Assays: Videos of tethered cells were analyzed with custom-written codes in MATLAB to determine the angular speed as a function of time[42]. Mean speeds for individual cells were determined from Gaussian fits to speed-distributions. *Swarming:* ImageJ plugins were employed to determine swarm radii from swarm images following previous protocols [43]. Briefly, since swarms rarely progressed symmetrically, the swarm expanse was first determined by manually drawing swarm-boundaries around the colony. Swarm-radius was then reported as the radius of an equivalent circular area corresponding to the selected region. *Swimming:* Most cells swam in straight lines for limited time-

periods in the liquid medium. For each cell, the frames over which straight-line motion was observed were averaged which resulted in a single image with bright streaks on a gray background. The corresponding length of the straight-line intensity profile was determined and divided by the period of observation to obtain swimming speed.

3.5.4. Torque Calculations

Cell-tracking enabled quantitative estimates of cell-geometries and the drag on tethered-cells was determined based on previous approaches [44]. A 2 μm long and 1 μm wide cell body tethered at a distance of 0.75-1 μm from the center offers an effective viscous load of ~ 150 pN-nm-s/revolution. The drag coefficient of a bead tethered to a filament stub and undergoing rotation along a circular trajectory with a non-zero eccentricity can be determined by representing the stub as a thin ellipsoid [29]. For stub lengths (~ 0.1-0.4 μm) and eccentricities (~ 0.15 - 0.5 μm), the loads due to 750 nm and 1000 nm beads at room temperature are ~ 9 and ~ 20 pN-nm-s/revolution, respectively.

3.5.5. Statistical analysis

All statistical analyses were performed in MATLAB either with the Student's t-test or the non-parametric Wilcoxon rank-sum test. Results with $p < 0.05$ were considered statistically significant and $p < 0.01$ were considered highly significant.

3.6. References

1 Turner, L., Caplan, S. R. & Berg, H. C. Temperature-induced switching of the bacterial flagellar motor. *Biophys J* 71, 2227-2233 (1996).

2 Inoue, Y. *et al.* Temperature dependences of torque generation and membrane voltage in the bacterial flagellar motor. *Biophys J* 105, 2801-2810 (2013).

3 Fukuoka, H., Inoue, Y., Terasawa, S., Takahashi, H. & Ishijima, A. Exchange of rotor components in functioning bacterial flagellar motor. *Biochem Bioph Res Co* 394, 130-135 (2010).

4 Delalez, N. J. *et al.* Signal-dependent turnover of the bacterial flagellar switch protein FliM. *Proc Natl Acad Sci* 107, 11347-11351, doi:10.1073/pnas.1000284107 (2010).

5 Yuan, J., Branch, R. W., Hosu, B. G. & Berg, H. C. Adaptation at the output of the chemotaxis signalling pathway. *Nature* 484, 233-236 (2012).

6 Lele, P. P., Branch, R. W., Nathan, V. S. & Berg, H. C. Mechanism for adaptive remodeling of the bacterial flagellar switch. *Proc Natl Acad Sci* 109, 20018-20022 (2012).

7 Lele, P. P., Shrivastava, A., Roland, T. & Berg, H. C. Response thresholds in bacterial chemotaxis. *Sci Adv* 1, doi:10.1126/sciadv.1500299 (2015).

8 Fung, D. C. & Berg, H. C. Powering the flagellar motor of *Escherichia-Coli* with an external voltage-source. *Nature* 375, 809-812 (1995).

9 Tipping, M. J., Steel, B. C., Delalez, N. J., Berry, R. M. & Armitage, J. P. Quantification of flagellar motor stator dynamics through in vivo proton-motive force control. *Mol Microbiol* 87, 338-347, doi:10.1111/mmi.12098 (2013).

10 Lele, P. P., Hosu, B. G. & Berg, H. C. Dynamics of mechanosensing in the bacterial flagellar motor. *Proc Natl Acad Sci* 110, 11839-11844, doi:10.1073/pnas.1305885110 (2013).

11 Tipping, M. J., Delalez, N. J., Lim, R., Berry, R. M. & Armitage, J. P. Load-dependent assembly of the bacterial flagellar motor. *MBio* 4, e00551-00513 (2013).

12 Castillo, D. J. *et al.* The C-terminal periplasmic domain of MotB is responsible for load-dependent control of the number of stators of the bacterial flagellar motor. *Biophysics* 9, 173-181 (2013).

13 Che, Y. S. *et al.* Load-sensitive coupling of proton translocation and torque generation in the bacterial flagellar motor. *Mol Microbiol* 91, 175-184, doi:10.1111/mmi.12453 (2014).

14 Terahara, N. *et al.* Load-and polysaccharide-dependent activation of the Na+-type MotPS stator in the Bacillus subtilis flagellar motor. *Sci Rep* 7, 46081 (2017).

15 Berg, H. C. Bacterial flagellar motor. *Curr Biol* 18, R689-R691 (2008).

16 Kojima, S. Dynamism and regulation of the stator, the energy conversion complex of the bacterial flagellar motor. *Curr Opin Microbiol* 28, 66-71, doi:10.1016/j.mib.2015.07.015 (2015).

17 Mccarter, L., Hilmen, M. & Silverman, M. Flagellar dynamometer controls swarmer cell-differentiation of *V. parahaemolyticus*. *Cell* 54, 345-351, doi:Doi 10.1016/0092-8674(88)90197-3 (1988).

18 Kearns, D. B. A field guide to bacterial swarming motility. *Nat Rev Microbiol* 8, 634-644, doi:10.1038/nrmicro2405 (2010).

19 Belas, R. Biofilms, flagella, and mechanosensing of surfaces by bacteria. *Trends Microbiol*, doi:10.1016/j.tim.2014.05.002 (2014).

20 Baker, A. E. & O'Toole, G. A. Bacteria, Rev Your Engines: Stator Dynamics Regulate Flagellar Motility. *J Bacteriol* 00088-00017 (2017).

21 Schoenhals, G. J. & Macnab, R. M. FliL is a membrane-associated component of the flagellar basal body of *Salmonella*. *Microbiology* 145, 1769-1775 (1999).

22 Partridge, J. D., Nieto, V. & Harshey, R. M. A new player at the flagellar motor: FliL controls both motor output and bias. *MBio* 6, e02367-02314 (2015).

23 Raha, M., Sockett, H. & Macnab, R. M. Characterization of the FliLGene in the Flagellar Regulon of *Escherichia coli* and *Salmonella typhimurium*. *J Bacteriol* 176, 2308-2311 (1994).

24 Jenal, U., White, J. & Shapiro, L. *Caulobacter* flagellar function, but not assembly, requires FliL, a non-polarly localized membrane protein present in all cell types. *J Mol Biol* 243, 227-244, doi:10.1006/jmbi.1994.1650 (1994).

25 Suaste-Olmos, F. *et al.* The flagellar protein FliL is essential for swimming in *Rhodobacter sphaeroides*. *J Bacteriol* 192, 6230-6239 (2010).

26 Cusick, K., Lee, Y. Y., Youchak, B. & Belas, R. Perturbation of FliL interferes with *Proteus mirabilis* swarmer cell gene expression and differentiation. *J Bacteriol* 194, 437-447, doi:10.1128/JB.05998-11 (2012).

27 Lee, Y.-Y. & Belas, R. Loss of FliL alters *Proteus mirabilis* surface sensing and temperature-dependent swarming. *J Bacteriol* 197, 159-173 (2015).

28 Chen, X. B. & Berg, H. C. Torque-speed relationship of the flagellar rotary motor of *Escherichia coli*. *Biophys. J.* 78, 1036-1041 (2000).

29 Ryu, W. S., Berry, R. M. & Berg, H. C. Torque-generating units of the flagellar motor of *Escherichia coli* have a high duty ratio. *Nature* 403, 444-447 (2000).

30 Blair, D. F. & Berg, H. C. Restoration of torque in defective flagellar motors. *Science* 242, 1678-1681 (1988).

31 Darnton, N. C., Turner, L., Rojevsky, S. & Berg, H. C. On torque and tumbling in swimming *Escherichia coli*. *J Bacteriol* 189, 1756-1764 (2007).

32 Ford, K. M., Chawla, R. & Lele, P. P. Biophysical Characterization of Flagellar Motor Functions. *J Vis Exp*, e55240, doi:doi:10.3791/55240 (2017).

33 Mariconda, S., Wang, Q. & Harshey, R. M. A mechanical role for the chemotaxis system in swarming motility. *Mol Microbio* 60, 1590-1602, doi:10.1111/j.1365-2958.2006.05208.x (2006).

34 Leake, M. C. *et al.* Stoichiometry and turnover in single, functioning membrane protein complexes. *Nature* 443, 355-358, doi:Doi 10.1038/Nature05135 (2006).

35 Bell, G. I. Models for the specific adhesion of cells to cells. *Science* 200, 618-627 (1978).

36 Meacci, G. & Tu, Y. Dynamics of the bacterial flagellar motor with multiple stators. *Proc Natl Acad Sci* 106, 3746-3751, doi:10.1073/pnas.0809929106 (2009).

37 Mandadapu, K. K., Nirody, J. A., Berry, R. M. & Oster, G. Mechanics of torque generation in the bacterial flagellar motor. *Proc Natl Acad Sci* 112, E4381-4389, doi:10.1073/pnas.1501734112 (2015).

38 Yuan, J. & Berg, H. C. Resurrection of the flagellar rotary motor near zero load. *Proc Natl Acad Sci* 105, 1182-1185, doi:10.1073/pnas.0711539105 (2008).

39 Zhu, S., Kumar, A., Kojima, S. & Homma, M. FliL associates with the stator to support torque generation of the sodium-driven polar flagellar motor of *Vibrio*. *Mol microbio* 98, 101-110 (2015).

40 Datsenko, K. A. & Wanner, B. L. One-step inactivation of chromosomal genes in *Escherichia coli* K-12 using PCR products. *Proc Natl Acad Sci* 97, 6640-6645 (2000).

41 Scharf, B. E., Fahrner, K. A., Turner, L. & Berg, H. C. Control of direction of flagellar rotation in bacterial chemotaxis. *Proc Natl Acad Sci USA* 95, 201-206 (1998).

42 Lele, P. P., Roland, T., Shrivastava, A., Chen, Y. & Berg, H. C. The flagellar motor of *Caulobacter crescentus* generates more torque when a cell swims backwards. *Nat Phys* 12, 175-178, doi:10.1038/nphys3528 (2016).

43 Morales-Soto, N. *et al.* Preparation, imaging, and quantification of bacterial surface motility assays. *J Vis Exp*, doi:10.3791/52338 (2015).

44 Meister, M. & Berg, H. C. The stall torque of the bacterial flagellar motor. *Biophys J* 52, 413-419 (1987).

45 Chawla, R., Ford, K.M., Lele, P.P. Torque, but not FliL, regulates mechanosensitive flagellar motor-function. *Sci Rep*, 7(1), 5565 (2017).

4. INDUCTION OF BIPHASIC CHEMOTAXIS IN *E. COLI* BY GUT METABOLITE INDOLE

4.1. Introduction

The mammalian gastrointestinal (GI) tract harbors a diverse community of ~10^{14} microorganisms, collectively known as the gut microbiota. Metabolites produced by the gut microbiota from dietary nutrients are key regulators of inflammation and infection in the GI tract [1-6]. In particular, indole – produced from the metabolism of tryptophan through the catalytic activity of the bacterial enzyme Tryptophanase A (TnaA) – has received wide attention for its role in regulating a broad range of bacterial phenotypes, including motility, stress responses, biofilm formation, antibiotic resistance, and virulence [7-11]. In addition to regulating bacterial physiology, indole also modulates indicators of inflammation and barrier function in intestinal epithelial cells [12]. Moreover, other indole-like metabolites derived from aromatic amino acids such as indole-3-acetate and tryptamine have also been shown to inhibit inflammation in macrophages and hepatocytes [13]. These varied functionalities underscore indole's importance as an interkingdom signaling molecule [12, 14-16].

Several species that inhabit the gut, especially those belonging to the phyla *Bacteroidetes*, *Firmicutes*, *Proteobacteria* and *Actinobacteria*, carry the *tnaA* gene and produce indole [14]. Indole production likely promotes gut health, since it inhibits colonization and virulence in several pathogenic species including enterohemorrhagic *E. coli* (EHEC) [18, 19], *Salmonella* [20, 21], and *Vibrio cholerae* [22]. However, indole can

exhibit contrasting roles in the regulation of virulence. For example, it promotes biofilm formation by *Pseudomonas aeruginosa* [24] and the survival of *Salmonella enterica* under antibiotic stress [14], two species that are incapable of producing the metabolite. The persistence of *Clostridium difficile* in the human colon also appears to be correlated with an increase in the fecal indole levels [25]. Since high concentrations of indole can inhibit cell growth, this suggests that certain metabolically-robust pathogens probably hijack indole production by the gut microbiome to out-compete commensals. Thus, the regulation of pathogenesis by indole is likely dependent on its local concentrations, although the underlying reasons are unclear.

Previous reports indicate that indole elicits a chemorepellent response in *Salmonella enterica* and *Escherichia coli* [26, 27] mediated through the Tsr chemoreceptor [28-31]. Other studies suggest that indole can induce an attractant response as well [29, 30]. Interestingly, strains of *E. coli* lacking all major chemotaxis genes other than the chemotactic response regulator *cheY* have been found to exhibit a repellent response to indole [32]. The mechanisms underlying these unusual chemotactic responses to indole and its analogues remain poorly understood.

The flagellar motor forms the output of the chemotaxis signaling network. Ligand binding to chemoreceptors modulates the phosphorylation levels of the CheY. CheY-P binds to a switch in the flagellar motor to regulate it's reversals between clockwise (CW) and counterclockwise (CCW) directions of rotation. The cell's chemotactic response can be measured in terms of the motor CW_{bias}, i.e., the fraction of the time that it rotates CW [40].

In this work, we investigated the mechanisms underlying the response of a lab *E. coli* strain to indole by tracking CW_{bias} with the aid of tethered cell assays, and demonstrate selective filtering of *E. coli* cells by indole on the basis of their chemotactic responses. Based on the biphasic chemotactic response elicited by indole, we propose a theoretical model wherein indole serves to both attract indole-producing commensals near the mucosal interface and repel pathogenic bacteria closer to the lumen.

4.2. Materials and methods

4.2.1.1. Strains and plasmids

All strains were derivatives of *E. coli* RP437 and are listed in Table 1.

Table 4-1: List of strains and plasmids.

Strain or plasmid	Relevant genotype	Source of reference
PL14	PL4 (*ΔcheY, sticky fliC*) with *pTrc99A- fliG*^{CW}	[33]
PL15	HCB33, sticky *fliC* allele	[34]
PL278	PL15 Δ*tar*	This work
PL225	PL15 Δ*tsr*	This work
PL139	PL 15 Δ*cheRcheBcheY*	This work
PL190	Δ*cheRcheBcheY,* Δ*tsr*	This work
PL221	Δ*cheRcheBcheY,* Δ*tar*	This work
PL234	Δ*cheRcheBcheY, ΔtsrΔtar*	This work
PL238	PL234+pPL3	This work
PL255	PL139+pPL3	This work
PL256	PL190+pPL3	This work
PL257	PL221+pPL3	This work
Plasmids		
pPL3	*pBAD34-cheY*	[34]
pPL1	*pTrc99A- fliG*^{CW}	[34]
pPL60s	*pBAD34-eyfpvar*	This work

4.2.1.2. Chemotactic Stimulation

A three-directional valve (Hamilton, Inc) was employed to exchange the fluid in the perfusion chambers with MB or MB containing chemoeffectors. The flow-rate (260 μl/min) was controlled by a syringe pump (Fusion 200, Chemyx Inc.). Separate calibration experiments were performed with a colored fluid to accurately estimate the average time of entry of chemoeffectors in the perfusion chamber, following a switch in the three-way valve.

4.2.1.3. pH-measurements

The pH-sensitive yellow fluorescent protein (KR-eYFP) was prepared based on an earlier approach that had been developed for the green fluorescent protein [38, 39]. The following mutations were introduced in the *eyfp* gene to generate the variant: S202H, E132D, S147E, N149L, N164I, K166Q, I167V, R168H, L220F and M153R. It was then encoded on an inducible vector (*ptrc99A*) and transformed into the wildtype RP437 strain (HCB33). The expression level was controlled with IPTG (100 μM). Excitation of the fluorophore was carried out on a Nikon Ti-E with an LED illumination source (SOLA SE II 365 light engine, Lumencor) filtered with a zet514/10x filter (Chroma Technology Corp). Approximately ~ 100-200 cells were excited in the field of view with a 60x water immersion objective (Nikon Instruments). The emission was collected by a sensitive photomultiplier (H7421-40 SEL, Hamamatsu Corporation) after passing through a bandpass emission filter (FF01-542/27, AVR Optics). Custom-written LabView codes were employed to record the photon-count over time. For calibration purposes, the emission from the cells was measured for ~ 100 s in MB. Then, the medium was

exchanged with one containing 40 mM benzoate/MB at pH 5. To test the effect of indole on internal pH, MB was replaced with MB containing 2 mM indole after 100 s. There was on pH-difference in the MB solutions with and without indole. During stimulation, cells were allowed to equilibrate for ~ 3 min before switching back to MB. Complementary *in vitro* assays with the purified protein showed a similar proportional increase in emission upon treatment with a pH 5 buffer solution.

4.2.1.4. Transwell Assay

A thin agar layer was poured in individual trans-well inserts (Nunc™ cell culture inserts), and then soaked overnight in motility buffer containing desired concentrations of indole. The inserts were then carefully transferred to individual wells in a 24-well plate (Carrier plate systems, ThermoFisher Scientific, Catalog #141002) carrying a suspension of GFP-expressing *E. coli* (see Appendix C, Figure C1). In the *primed* case, the cell suspension contained indole. In the *unprimed* case, the cell suspension contained no indole. A concentration gradient of indole was established within minutes in the wells. Cells that migrated towards the agar source (attractant response) become attached to the bottom of the agar insert. Control experiments were conducted in an identical manner except that the agar was soaked in motility buffer only and there was no indole present in the cell suspension. After 5 minutes, the insert was carefully removed, gently washed with MB to remove unstuck cells, and then imaged via confocal microscopy. Custom-written MATLAB codes were then employed to count the number of cells adhered to the surface.

4.3. Results

4.3.1. Tsr receptor dominates repellent response at low concentrations of indole

We employed the tethered cell assay to measure CW_{bias} during the stimulation of individual cells with indole in perfusion chambers. When wildtype cells were stimulated by 0.02 mM indole, a strong and reproducible repellent response was immediately observed. The response precisely adapted to the original value within ~ 30-50 s, as shown in Figure 4-1A. When indole was replaced with motility buffer, it had the opposite effect; the CW_{bias} decreased initially and subsequently adapted to its pre-stimulus value (see Appendix C, Figure C2). Stimulation of isogenic mutant cells lacking the Tar receptor did not significantly alter the response (Figure 4-1A). However, the deletion of the other major receptor, Tsr, caused complete inhibition of the repellent response. This suggested that Tsr mediates repellent responses at low concentrations of indole (0.02 mM).

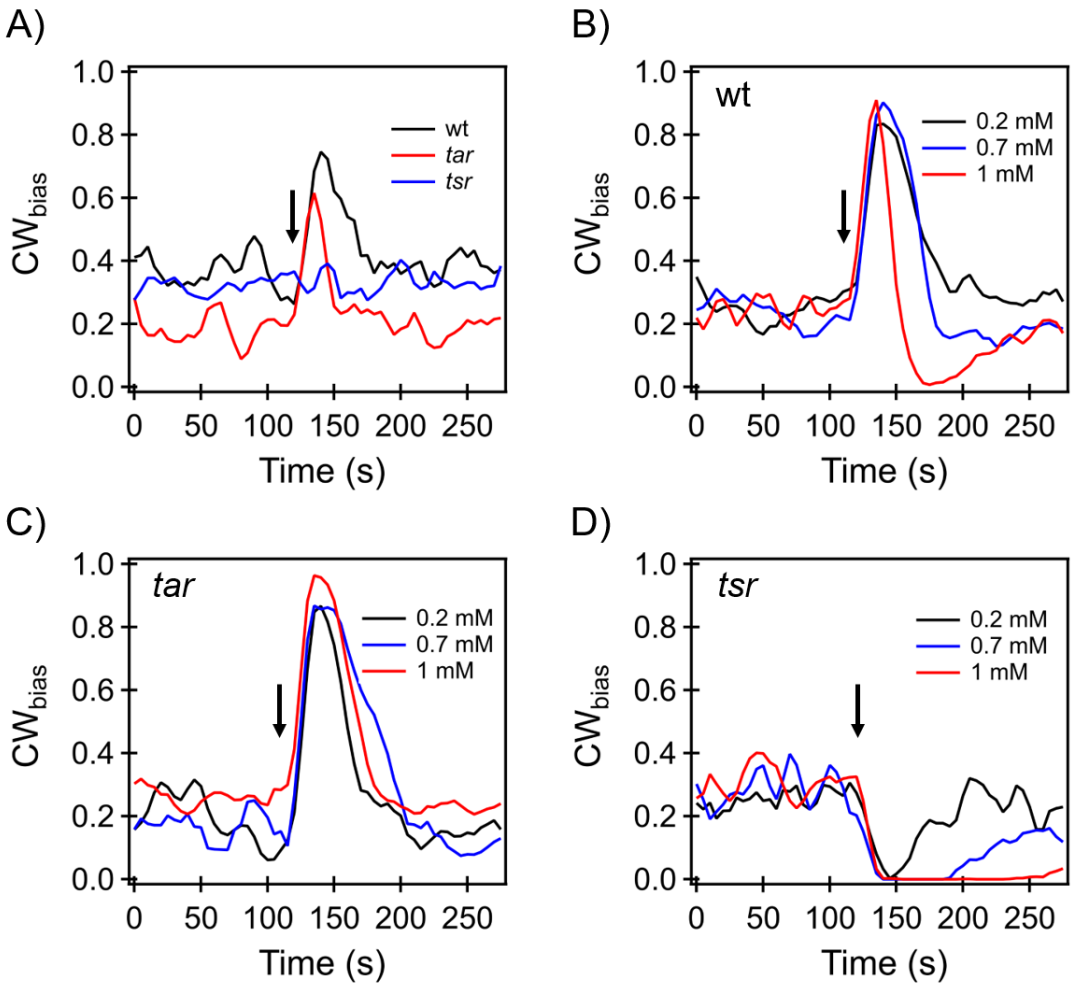

Figure 4-1 Response of wild-type, *tar* and *tsr* mutant to Indole. A) Averaged response of tethered cells to 20 uM indole. The arrow indicates the approximate time of exposure to indole. The wildtype (black curve) and the *tar* knockout (red curve) both exhibited a brief increase in CW_{bias}, indicating a repellent response. The response precisely adapted such that the pre- and post-stimulus CW_{bias} were similar. The *tsr* knockout showed no response to the stimulation. B) The short-time repellent response was evident over the entire range of concentrations tested, as indicated the increase in CW_{bias} ~ 20-50 s following stimulation. At longer times (> 50 s), an attractant response was evident when cells were treated with 1 mM indole. A similar inversion was observed upon treatment with 2 mM indole (see Fig S2). C) A strong repellent response was observed in case of the *tar* mutant over the entire range tested. The adaptation was precise in each case. D) Attractant responses were observed in the Tsr mutant over the 0.2 – 1 mM concentration range. The delay in adaptation in response increased with indole concentrations. All response curves in A, B, C, and D represent an average over n = 11-21 motors. The average error was 0.0122.

4.3.2. Tar Mediates an Attractant Response at High Indole Concentration

At higher concentrations of indole (0.2 – 0.7 mM), wildtype cells continued to exhibit the initial repellent response that adapted precisely. However, the initial repellent response inverted to an attractant response ~ 50 s later when the cells were treated with 1 mM indole, as shown in Figure 4-1B. A similar inversion was observed at 2 mM indole concentratrion (see Appendix C, Figure C2).

When stimulated with 0.2 – 1 mM indole, mutants lacking Tar exhibited repellent-only responses that adapted precisely to the pre-stimulus levels. The degree of increase in the CW_{bias} appeared to be relatively insensitive to indole concentrations, suggesting that the repellent response saturated above 0.2 mM indole. The absence of inversion in the response, even at 1 mM indole, suggested that Tar likely mediated the attractant responses that were observed in the wildtype **(**Figure 4-1C). A mutant lacking Tsr exhibited a strong attractant response to 0.2 – 1 mM indole, consistent with the notion that the repellent response is dominated by Tsr. Adaptation in the *tsr* mutant occurred with increasing delays as the concentration of indole increased, as shown in Figure 4-1D, making it unlikely that the attractant response.

The replacement of indole with motility buffer had the opposite effects in the wildtype, *tsr* and *tar* strains (see Figure C2). The opposite mediation by Tar (attractant response) and Tsr (repellent response) were also observed at 2 mM indole. A modified version of the standard chemotaxis model [41] that accounted for differential binding affinities for indole in the Tar and Tsr receptors was able to qualitatively reproduce the

results. This included the inversion in response at higher indole concentrations (see supplementary text and Figure C3).

4.3.3. Flagellar Switch Mediates a Network-Independent Response

Next, we stimulated a mutant lacking the Tar and Tsr receptors with 1 mM indole. The mutant exhibited a strong repellent-only response that did not adapt even over ~ 200 s (Figure 4-2A). Considering the weak adaptation in the *tar-tsr* mutant, it was possible that CheA activity itself was not significantly perturbed during the stimulation. If so, then the observed repellent response was likely receptor-independent.

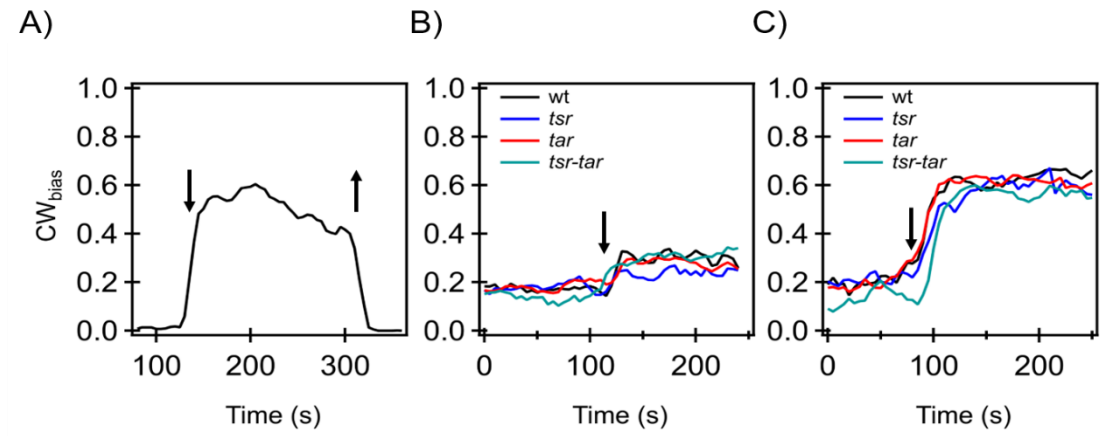

Figure 4-2 Network-independent Indole response. A) Averaged response of a *tar-tsr* mutant to 1 mM indole. The entry and exit of indole from the flowcell is indicated by the down and up arrows. A repellent-only response was observed with minimal adaptation. B and C) Averaged responses of different *cheR-cheB* mutants to 0.2 mM and 2 mM indole, respectively. Data indicated by the black, blue, red, and the green curves represent the wt (Δ*cheR-cheB*), tsr (Δ*cheR-cheB-tsr*), tar (Δ*cheR-cheB-tar*), and tsr-tar (Δ*cheRcheB-tsr-tar*) strains, respectively. The responses are purely repulsive with no adaptation. All response curves in A, B, and C, were averaged over n = 11 to 22 motors, and the average error was 0.0114.

To test the hypothesis, we stimulated motors in a Δ*cheRB* strain with indole. In the absence of the CheR and CheB (methyltransferase/methylesterase) enzymes, the sensitivity to stimulants (chemoeffectors) is drastically reduced [42]. We predicted that if the strong repellent response in Figure 4-2A was indeed CheA-independent, then a similar repellent response might occur even in the de-sensitized Δ*cheRB* strain. Since the basal kinase activity in a Δ*cheRB* strain is higher [42], the motors rotate predominantly in the CW direction. To ensure that the pre- and post-stimulus CW_{bias} remained within the dynamic range ($0 < CW_{bias} < 1$), we deleted the chromosomal *cheY* gene and expressed CheY from a low copy number plasmid [43]. The induction level was tuned such that tethered cells exhibited an averaged pre-stimulus bias similar to wildtype cells (See Figure C4 in Appendix C).

The Δ*cheRB* strain as well as Δ*cheRB* strains lacking either Tsr, Tar, or both receptors, consistently demonstrated repellent-only responses of similar magnitudes, when stimulated with indole. The responses did not adapt. The degree of change in CW_{bias} increased with increasing concentrations of indole over the range of 0.2 mM (Figure 4-2B) to 2 mM (Figure 4-2C). The attractant response that was observed in the *tsr* mutant was completely abolished in the Δ*cheR-cheB-tsr* strain. This was consistent with the notion that even at the maximum concentrations tested (2 mM), indole failed to significantly stimulate CheA in the absence of CheR and CheB, despite which a repellent response was observed.

4.3.4. Switch Response Is Independent of Cytoplasmic pH

Although the cytoplasmic pH is insensitive to indole [44, 45], Gaimster and Summers reported that bursts of high concentrations of indole (~ 60 mM) produced by stationary phase *E. coli* cells in rich media led to a reduction of the cytoplasmic pH. Since such a pH-reduction can elicit a chemorepellent response [44, 46], we hypothesized that the receptor-independent repellent-response to indole occurred due to a reduction in the cytoplasmic pH. To test this, we expressed a variant of the yellow fluorescent protein in the wildtype strain to probe if indole altered the intracellular pH (see Materials and Methods). Cells adhered to a glass surface in a perfusion chamber were treated with a mix of 40 mM Benzoate and buffer (at pH 5), following previous approaches [47, 48], and illuminated with an appropriate excitation source. Treatment with benzoate permeabilizes the membrane and equalizes the cytoplasmic pH and extracellular pH. A strong change in the emission intensities was observed when the neutral buffer medium was exchanged with a buffer containing 40 mM Benzoate at pH 5 **(**Figure 4-3A). However, repeated cycles of exposure to 2 mM indole failed to elicit a measurable change in the emission intensities (Figure 4-3B). This suggests that the exposure to 2 mM exogenous indole did not cause a measurable change in the cytoplasmic pH, subject to the detection limits of our experimental setup.

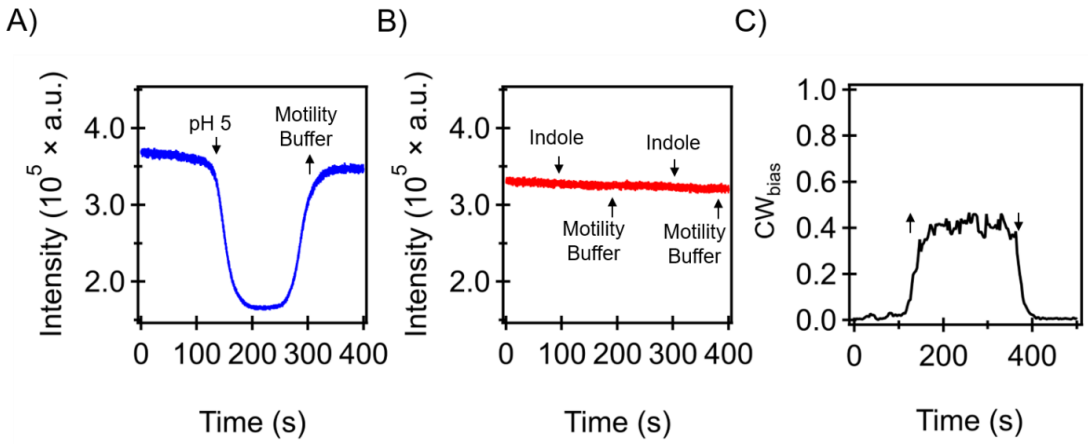

Figure 4-3 Interaction of indole with switch protein. A) Emission intensities of a pH-sensitive eYFP variant expressed in a wildtype strain. The first 100 s indicate the intensities when cells experienced a neutral buffer solution (MB, pH ~ 7). At ~ 100 s, MB was replaced with an acidic medium (MB, pH 5 plus 40 mM Benzoate). The acidification of the intracellular milieu resulted in a drop in the emission intensities. When the medium was exchange with MB (pH ~ 7) again at ~ 300 s, the emission intensity returned to a value very similar to the pre-stimulus level. The slight difference in pre- and post-stimulus values was due to photobleaching. B) Cells were stimulated with 1 mM indole at times indicated by the down arrows. No measurable change in the emission intensities was observed in the presence of indole. Signal was obtained over n ~ 100-200 cells. C) Averaged response to indole of $FliG^{CW}$-$FliG^{WT}$ motors that switch despite the lack of CheY.

4.3.5. Indole Interacts with Switch Proteins to Induce Repellent Response

The switch consists of the FliM and FliN complexes to which CheY-P binds, and the FliG ring which interacts with the stators to rotate the motor. We hypothesized that indole permeated the membrane and interacted with the flagellar switch, either directly or indirectly, to activate it. To test the hypothesis, we generated a Δ*cheY* strain, but in which the motors were capable of switching [33]. Although motors rotate only CCW in a Δ*cheY* strain, they are able to switch in this particular strain due to the presence of a few mutant FliG subunits in an otherwise wildtype FliG ring. These mutant subunits are locked in the active conformation ($FliG^{CW}$) and switching occurs incessantly through FliG-FliG

cooperative interactions [33]. Mixed FliG motors were generated by expressing the mutant subunits from an inducible vector, while the native FliG subunits were genomically-expressed. The response of the Δ*cheY* mixed FliG motors to 2 mM indole is shown in Figure 4-3C. Stimulation was followed by an increase in the CW_{bias} that was of a similar magnitude as the changes observed in Figure 4-2A-C.

Chemotactic Adaptation to Indole Promotes Rapid Colonization of Indole-Rich Surfaces

Considering that the repellent response to indole appeared to saturate but not the attractant response **(**Figure 4-1A-C), we hypothesized that cells that became adapted to lower concentrations of indole might exhibit attractant-only response at higher concentrations. To test this hypothesis, we repeatedly stimulated the same population of wildtype tethered cells with increasing concentrations of indole. Expectedly, an immediate repellent response was observed at concentrations below 1 mM. However, once the cells had precisely adapted to 0.7 mM indole, exposure to higher concentrations of indole (1 and 2 mM) induced attractant-only responses, as shown in Figure 4-4A). In such chemotactically-adapted or *primed* cells, the Tsr-mediated repellent response was absent at high indole concentrations.

Next, we investigated whether priming could induce an attractant chemotactic behavior leading to elevated attachment of cells to indole-rich substrates. To do this, we employed an inverted transwell assay (see Materials and Methods), as done previously [51, 52]. Agar pads pre-soaked in 2 mM indole were brought in contact with *E. coli* that

had been primed in 2 ml of MB containing 0.7 mM indole. Over the duration of 5 min, the primed cells migrated towards the indole-soaked agar and became stuck to the surface. Adhesion to the agar substrate was higher in primed cells compared to unprimed cells that were suspended in 2 ml MB-only (Figure 4-4B). Similarly, the adhesion of primed cells was higher relative to the basal adhesion level that was observed with agar pads soaked in MB-only and exposed to cell suspensions lacking indole.

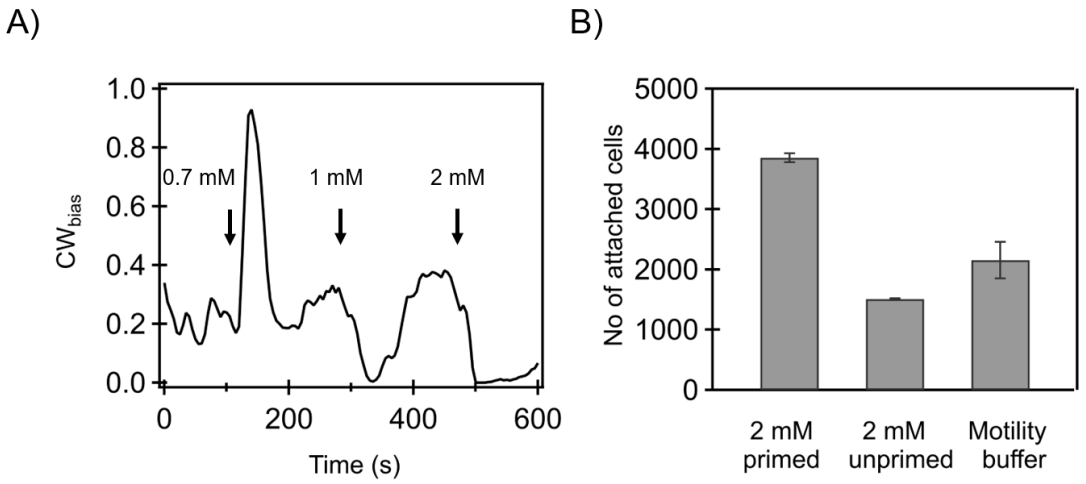

Figure 4-4 Stimulation with increasing concentration of indole and transwell assay. A) Wildtype cells were stimulated with increasing concentrations of indole. Once the cells had adapted to a lower concentration of indole (0.7 mM), they exhibited an attractant-only response at higher concentrations (> 0.7 mM indole). The preliminary repellent response that was observed in unprimed cells (Fig 1B) was absent in these primed cells. B) Cell migration towards and adhesion to indole-rich sources was measured with transwell assays. The average number of adherent cells was higher in case of the primed cells when exposed to agar soaked in 2 mM indole. In the case of unprimed cells belonging to the same wildtype strain, the average number of adherent cells was ~ 50% lower when exposed to agar soaked in 2mM indole. The basal average adhesion was also lower in case of unprimed cells exposed to agar soaked in MB-only.

4.4. Discussion

Biphasic sensing of molecules by Tar and Tsr has been reported for media of varying pH, neurotransmitters, and leucine [53-57]. Our results demonstrate that the two major receptors, Tar and Tsr, demonstrate a biphasic response to the GI tract metabolite indole by mediating attractant and repellent responses, respectively. Higher concentrations of indole (> 0.2 mM) trigger a time-dependent inversion from a Tsr-mediated repellent response to a Tar-mediated attractant response. Tsr dominates the short-time responses (~0-50 s), whereas Tar dominates the long-time responses (> 50 s).

The CW_{bias} varies steeply over a narrow range of CheY-P levels, and the dynamic range of the motor bias (0 to 1) is easily exceeded by relatively small changes in CheY-P levels [37, 58, 59]. The increasing delays in the adaptation in the *tsr* mutant are reflective of the degree of change caused by indole in the CheY-P levels – the greater the reduction in [CheY-P], longer the time necessary to restore [CheY-P] to pre-stimulus values. This indicates that the Tar response does not saturate at the levels of indole tested in this work. In contrast, Tsr's repellent response and hence, [CheY-P], saturates at indole concentrations 0.2 mM and higher. The time needed for adaptation is also insensitive to indole concentrations. Based on these observations, we propose that Tsr has a higher affinity for indole relative to Tar, and that the rate of indole binding to Tsr is also faster.

The domains of Tar and Tsr that bind indole are unknown. The repellent-response to indole is retained even in periplasm-void *E. coli* cells, which might suggest that the periplasmic binding domain of the Tsr receptor is not important in indole-sensing [60]. However, considering that repellent responses can also arise due to the interactions of the

flagellar switch with indole, further experimentation is necessary to identify the correct receptor domains involved in indole sensing. Since Tar mediates an attractant response, the domains responsible for indole-sensing may be different from those in Tsr. These questions can be addressed with receptor hybrids that exchange domains between the two major receptors [61, 62].

Part of the repellent response to indole is receptor-independent and likely arises due to the interactions of the flagellar switch with indole as the metabolite permeates the membranes. It is possible that the interactions with indole induce FliG subunits to increase their propensities for the active (CW) conformation. The increased propensity is stabilized by the binding of CheY-P to the motor, resulting in an increase in CW_{bias} even when CheA activity remains unchanged. A two-state model for the flagellar switch, which was adapted from previous work [37], was able to correctly predict the receptor-independent motor responses to indole based on this idea (see Appendix C and Figure C3).

Our data indicate that in presence of ~ 0.7 mM indole, the Tsr receptors become immediately saturated whereas the Tar receptors do not. Upon adaptation to the threshold level of 0.7 mM indole, no short-time repellent response is observed when the primed cells are further exposed to higher indole concentrations. Instead, only the Tar-induced strong attractant response is observed. In unprimed cells however, the short-time repellent response persists even at high indole concentrations. Based on this, we propose a two-zone model in the GI-tract, where the physiological effects of indole differ based on its concentrations. In the proximity of the mucosal interface where indole-producing commensal microbes exist, indole concentrations are high (0.3 to ~ 6.5 mM in human stool

samples [45]). Commensal bacteria present in these microenvironments likely sense indole as a chemoattractant since they are primed through continuous exposure to concentrations above the threshold. Away from the mucosal interface, indole levels drop below the threshold in the lumen of the GI tract [21]. In this region (zone 2), bacteria sense indole as a chemorepellent, which prevents chemotactic migration towards the mucosal interface (Figure 4-5). This is supported by our observations that indicate a higher number of primed cells migrate and adhere to sources rich in indole concentrations, relative to unprimed cells.

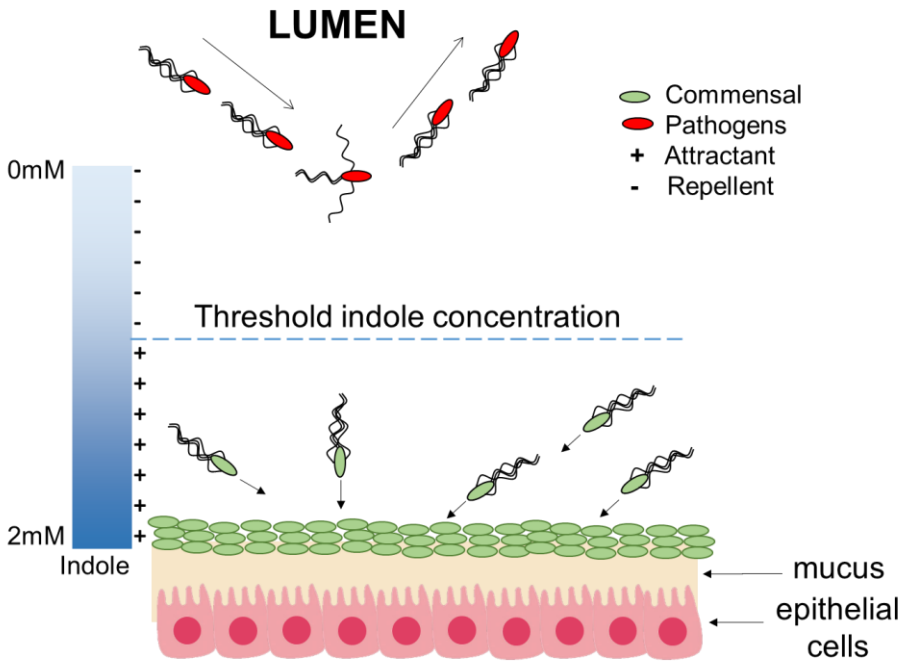

Figure 4-5 Filtering action of indole in the GI-tract. The indole levels near the mucosal layers (zone 1) are above the threshold concentration. Primed cells are attracted to the source, leading to recruitment of commensal bacteria to existing microbial communities. Away from the source (zone 2), indole concentrations are lower than the threshold. Low indole concentrations prevent cells from becoming primed, inducing a strong repellent response. This causes pathogens to migrate towards the lumen.

The induction of biphasic chemotaxis by indole has significant implications in the maintenance of gut health. The chemoattractant response induced by high indole concentrations near the mucosal interface likely promotes the recruitment of motile commensal bacteria to existing microbial communities and the development of new microbial niches [9]. On the other hand, the chemorepellent response induced by low concentrations of indole in the lumen likely thwarts motile pathogenic bacteria such as *E. coli* O157:H7 and *Salmonella* from gaining a foothold in the mucosa. Since indole's ability to attract or repel bacteria depends on its concentrations, we speculate that its production is tuned by the microbial community in the gut to complement the host's natural defense mechanisms. It is also likely that indole plays a key role in the regulation of biofilms in abiotic environments, by recruiting bacteria through positive chemotaxis during biofilm formation and by promoting bacterial spread through negative chemotaxis during biofilm dispersal. Our findings provide the first explanation for indole's dose-dependent regulation of the formation and maintenance of microbial communities.

4.5. References

1. Sekirov, I. and B.B. Finlay, *The role of the intestinal microbiota in enteric infection.* The Journal of physiology, 2009. **587**(17): p. 4159-4167.

2. Keeney, K.M. and B.B. Finlay, *Enteric pathogen exploitation of the microbiota-generated nutrient environment of the gut.* Current opinion in microbiology, 2011. **14**(1): p. 92-98.

3. Flint, H.J., et al., *The role of the gut microbiota in nutrition and health.* Nature reviews Gastroenterology & hepatology, 2012. **9**(10): p. 577.

4. Zhang, Y.-J., et al., *Impacts of gut bacteria on human health and diseases.* International journal of molecular sciences, 2015. **16**(4): p. 7493-7519.

5. Valdes, A.M., et al., *Role of the gut microbiota in nutrition and health.* Bmj, 2018. **361**: p. k2179.

6. Makki, K., et al., *The Impact of Dietary Fiber on Gut Microbiota in Host Health and Disease.* Cell Host & Microbe, 2018. **23**(6): p. 705-715.

7. Domka, J., J. Lee, and T.K. Wood, *YliH (BssR) and YceP (BssS) regulate Escherichia coli K-12 biofilm formation by influencing cell signaling.* Appl Environ Microbiol, 2006. **72**(4): p. 2449-59.

8. Lee, J., et al., *Enterohemorrhagic Escherichia coli biofilms are inhibited by 7-hydroxyindole and stimulated by isatin.* Appl Environ Microbiol, 2007. **73**(13): p. 4100-9.

9. Bansal, T., et al., *Differential effects of epinephrine, norepinephrine, and indole on Escherichia coli O157:H7 chemotaxis, colonization, and gene expression.* Infect Immun, 2007. **75**(9): p. 4597-607.

10. Lee, J., et al., *Indole and 7-hydroxyindole diminish Pseudomonas aeruginosa virulence.* Microb Biotechnol, 2009. **2**(1): p. 75-90.

11. Nikaido, E., et al., *Effects of indole on drug resistance and virulence of Salmonella enterica serovar Typhimurium revealed by genome-wide analyses.* Gut Pathog, 2012. **4**(1): p. 5.

12. Bansal, T., et al., *The bacterial signal indole increases epithelial-cell tight-junction resistance and attenuates indicators of inflammation.* Proc Natl Acad Sci U S A, 2010. **107**(1): p. 228-33.

13. Krishnan, S., et al., *Gut microbiota-derived tryptophan metabolites modulate inflammatory response in hepatocytes and macrophages.* Cell reports, 2018. **23**(4): p. 1099-1111.

14. Lee, J.H. and J. Lee, *Indole as an intercellular signal in microbial communities.* FEMS Microbiol Rev, 2010. **34**(4): p. 426-44.

15. Tomberlin, J.K., et al., *Indole: An evolutionarily conserved influencer of behavior across kingdoms.* Bioessays, 2017. **39**(2).

16. Lee, J.-H., T.K. Wood, and J. Lee, *Roles of Indole as an Interspecies and Interkingdom Signaling Molecule.* Trends in Microbiology, 2015. **23**(11): p. 707-718.

17. Lee, J., A. Jayaraman, and T.K. Wood, *Indole is an inter-species biofilm signal mediated by SdiA.* BMC microbiology, 2007. **7**(1): p. 42.

18. Sridharan, G.V., et al., *Prediction and quantification of bioactive microbiota metabolites in the mouse gut.* Nat Commun, 2014. **5**: p. 5492.

19. Kumar, A. and V. Sperandio, *Indole Signaling at the Host-Microbiota-Pathogen Interface.* mBio, 2019. **10**(3): p. e01031-19.

20. Kohli, N., et al., *The microbiota metabolite indole inhibits Salmonella virulence: Involvement of the PhoPQ two-component system.* PloS one, 2018. **13**(1): p. e0190613.

21. Bettegowda, C., et al., *The genome and transcriptomes of the anti-tumor agent Clostridium novyi-NT.* Nat Biotechnol, 2006. **24**(12): p. 1573-80.

22. Howard, M.F., X.R. Bina, and J.E. Bina, *Indole inhibits ToxR regulon expression in Vibrio cholerae.* Infection and Immunity, 2019: p. IAI.00776-18.

23. Oh, S., et al., *The bacterial signalling molecule indole attenuates the virulence of the fungal pathogen Candida albicans.* Journal of Applied Microbiology, 2012. **113**(3): p. 622-628.

24. Kim, S.-K., H.-Y. Park, and J.-H. Lee, *Anthranilate Deteriorates the Structure of Pseudomonas aeruginosa Biofilms and Antagonizes the Biofilm-Enhancing Indole Effect.* Applied and Environmental Microbiology, 2015. **81**(7): p. 2328-2338.

25. Darkoh, C., et al., *Clostridium difficile Modulates the Gut Microbiota by Inducing the Production of Indole, an Interkingdom Signaling and Antimicrobial Molecule.* mSystems, 2019. **4**(2): p. e00346-18.

26. Tsang, N., R. Macnab, and D.E. Koshland, *Common Mechanism for Repellents and Attractants in Bacterial Chemotaxis.* Science, 1973. **181**(4094): p. 60-63.

27. Tso, W.W. and J. Adler, *Negative chemotaxis in Escherichia coli.* Journal of bacteriology, 1974. **118**(2): p. 560-576.

28. Springer, M.S., M.F. Goy, and J. Adler, *Sensory transduction in Escherichia coli: two complementary pathways of information processing that involve methylated proteins.* Proceedings of the National Academy of Sciences of the United States of America, 1977. **74**(8): p. 3312-3316.

29. Muskavitch, M., et al., *Attraction by repellents: an error in sensory information processing by bacterial mutants.* Science, 1978. **201**(4350): p. 63-65.

30. Reader, R.W., et al., *Pleiotropic Aspartate Taxis and Serine Taxis Mutants of Escherichia coli.* Microbiology, 1979. **111**(2): p. 363-374.

31. Parkinson, J.S. and P.T. Revello, *Sensory adaptation mutants of E. coli.* Cell, 1978. **15**(4): p. 1221-1230.

32. Montrone, M., D. Oesterhelt, and W. Marwan, *Phosphorylation-independent bacterial chemoresponses correlate with changes in the cytoplasmic level of fumarate.* Journal of Bacteriology, 1996. **178**(23): p. 6882-6887.

33. Lele, Pushkar P. and Howard C. Berg, *Switching of Bacterial Flagellar Motors Triggered by Mutant FliG.* Biophysical Journal, 2015. **108**(5): p. 1275-1280.

34. Lele, P.P., et al., *Mechanism for adaptive remodeling of the bacterial flagellar switch.* Proc. Natl Acad. Sci. USA, 2012. **109**(49): p. 20018-22.

35. Scharf, B.E., et al., *Control of direction of flagellar rotation in bacterial chemotaxis.* Proceedings of the National Academy of Sciences, 1998. **95**(1): p. 201-206.

36. Ford, K.M., R. Chawla, and P.P. Lele, *Biophysical characterization of flagellar motor functions.* JoVE (Journal of Visualized Experiments), 2017(119): p. e55240.

37. Lele, P.P., et al., *Response thresholds in bacterial chemotaxis.* Science Advances, 2015. **1**(9): p. e1500299.

38. Miesenböck, G., D.A. De Angelis, and J.E. Rothman, *Visualizing secretion and synaptic transmission with pH-sensitive green fluorescent proteins.* Nature, 1998. **394**(6689): p. 192.

39. Morimoto, Y.V., et al., *M153R mutation in a pH-sensitive green fluorescent protein stabilizes its fusion proteins.* PLoS One, 2011. **6**(5): p. e19598.

40. Block, S.M., J.E. Segall, and H.C. Berg, *Adaptation kinetics in bacterial chemotaxis.* Journal of Bacteriology, 1983. **154**(1): p. 312-323.

41. Tu, Y., *Quantitative modeling of bacterial chemotaxis: signal amplification and accurate adaptation.* Annu Rev Biophys, 2013. **42**: p. 337-59.

42. Sourjik, V. and H.C. Berg, *Receptor sensitivity in bacterial chemotaxis.* Proceedings of the National Academy of Sciences, 2002. **99**(1): p. 123-127.

43. Guzman, L.M., et al., *Tight regulation, modulation, and high-level expression by vectors containing the arabinose PBAD promoter.* Journal of Bacteriology, 1995. **177**(14): p. 4121-4130.

44. Kihara, M. and R.M. Macnab, *Cytoplasmic pH mediates pH taxis and weak-acid repellent taxis of bacteria.* Journal of Bacteriology, 1981. **145**(3): p. 1209-1221.

45. Slonczewski, J.L., et al., *Effects of pH and Repellent Tactic Stimuli on Protein Methylation Levels in Escherichia coli.* Journal of Bacteriology, 1982. **152**(1): p. 384-399.

46. Repaske, D.R. and J. Adler, *Change in intracellular pH of Escherichia coli mediates the chemotactic response to certain attractants and repellents.* Journal of bacteriology, 1981. **145**(3): p. 1196-1208.

47. Wilks, J.C. and J.L. Slonczewski, *pH of the Cytoplasm and Periplasm of Escherichia coli: Rapid Measurement by Green Fluorescent Protein Fluorimetry.* Journal of Bacteriology, 2007. **189**(15): p. 5601-5607.

48. Martinez, K.A., et al., *Cytoplasmic pH Response to Acid Stress in Individual Cells of Escherichia coli and Bacillus subtilis Observed by Fluorescence Ratio Imaging Microscopy.* Applied and Environmental Microbiology, 2012. **78**(10): p. 3706-3714.

49. Duke, T.A., N. Le Novère, and D. Bray, *Conformational spread in a ring of proteins: a stochastic approach to allostery.* J. Mol. Biol., 2001. **308**(3): p. 541-53.

50. Bray, D. and T. Duke, *Conformational spread: the propagation of allosteric states in large multiprotein complexes.* Annu Rev Biophys Biomol Struct, 2004. **33**: p. 53-73.

51. Jani, S., et al., *Chemotaxis to self-generated AI-2 promotes biofilm formation in Escherichia coli.* Microbiology, 2017. **163**(12): p. 1778-1790.

52. Jani, S., *Visualizing Chemoattraction of Planktonic Cells to a Biofilm*, in *Bacterial Chemosensing*. 2018, Springer. p. 61-69.

53. Khan, S., et al., *Chemotactic signal integration in bacteria.* Proceedings of the National Academy of Sciences, 1995. **92**(21): p. 9757-9761.

54. Mao, H., P.S. Cremer, and M.D. Manson, *A sensitive, versatile microfluidic assay for bacterial chemotaxis.* Proceedings of the National Academy of Sciences, 2003. **100**(9): p. 5449-5454.

55. Khan, S. and D.R. Trentham, *Biphasic excitation by leucine in Escherichia coli chemotaxis.* Journal of bacteriology, 2004. **186**(2): p. 588-592.

56. Yang, Y. and V. Sourjik, *Opposite responses by different chemoreceptors set a tunable preference point in Escherichia coli pH taxis.* Molecular Microbiology, 2012. **86**(6): p. 1482-1489.

57. Lopes, J.G. and V. Sourjik, *Chemotaxis of Escherichia coli to major hormones and polyamines present in human gut.* The ISME journal, 2018. **12**(11): p. 2736-2747.

58. Cluzel, P., M. Surette, and S. Leibler, *An ultrasensitive bacterial motor revealed by monitoring signaling proteins in single cells.* Science, 2000. **287**(5458): p. 1652-1655.

59. Yuan, J., et al., *Adaptation at the output of the chemotaxis signalling pathway.* Nature, 2012. **484**: p. 233.

60. Eisenbach, M., et al., *Repellents for Escherichia coli operate neither by changing membrane fluidity nor by being sensed by periplasmic receptors during chemotaxis.* Journal of Bacteriology, 1990. **172**(9): p. 5218-5224.

61. Pham, H.T. and J.S. Parkinson, *Phenol Sensing by Escherichia coli Chemoreceptors: a Nonclassical Mechanism.* Journal of Bacteriology, 2011. **193**(23): p. 6597-6604.

62. Bi, S., F. Jin, and V. Sourjik, *Inverted signaling by bacterial chemotaxis receptors.* Nature communications, 2018. **9**(1): p. 2927.

5. SURFACE-INDUCED DRAG ON MOTILE BACTERIA

5.1. Introduction

Flagellated bacteria often exhibit a surface-dependent collective motility known as swarming. Swarming represents an important mechanism for bacterial colonies to cover large distances on soft surfaces and tissues, and has been implicated in infections of the urinary tract [1]. Swarming in E. coli and other swarmer species is typically studied on agar surfaces, which mimic tissues to an extent. E. coli swarm over a very narrow range of agar concentrations (0.45-0.5% of Eiken agar) but are unable to exhibit swarming at higher concentrations of agar. Furthermore, when swarmer cells are removed from the substrate and dispersed in liquid cultures, they revert back to planktonic cells.

The key difference between growth on a substrate and the liquid culture is the difference in the frictional forces experienced by bacteria in the two cases. It has been proposed that the agar surface represents a high load condition on the flagellum and the cell body [1, 2]. Sensing of the high loads by flagella likely initiates the transition from the planktonic to the swarming state [2]. However, the underlying assumption that proximity of the flagella or the cell to soft surfaces such as agar can result in an increase in viscous loads remains untested. Here, we attempted to measure surface drag as a function of agar concentrations. The goal was to determine the role of surface drag near soft-substrates in the transition from planktonic to swarmer states. To do this, we employed optical traps to catch and release 2μm-spherical beads at discrete separations from an agar surface. The diffusion of the beads was measured at these discrete separations

to indirectly determine the surface drag at two different agar concentrations. Our methods and results are explained ahead.

As the gap between a particle and a no-slip solid surface becomes small, it requires increasingly large amounts of pressure to push in or squeeze out the fluid mass between the two [3]. This leads to strong frictional forces, which slow the movements of the particle with respect to the surface [3]. These effects are particularly significant at very short separations from the surface of the wall (separation ~ 0.01 radius of the bead). Hence, the diffusion of a spherical particle near a solid boundary is dampened. The behavior is not understood for a partial slip surface [4]. This reduction in diffusion is true for the lateral mode (parallel to the surface) as well as transverse model (normal to the surface). The closer the bead to the surface, the lower its diffusion coefficient. The first crude approximations for the dependence of spherical particle surface-drag (or, from which equivalent expression diffusions can be calculated) as a function of separation from a rigid wall were developed by Lorentz and Faxen [5, 6]. Later work by Brenner et al. provided exact expressions for both the transverse (perpendicular mode) and lateral (parallel mode) components of diffusion coefficient near a no-slip boundary [7-9]. Various experimental approaches have been used to successfully test the validity of these predictions for range of particle sizes [3]. These approaches include photonic force microscopy [10], optical trap microscopy[11], near-wall velocimetry measurements [12], three-dimensional total internal reflection velocimetry (TIRV) [13], standard and multilayer nano-PIV [14], and different dynamic light scattering (DLS) approaches like standard DLS [15], low-

coherence DLS [16], resonance-enhanced DLS [17], and evanescent wave DLS [18, 19]. The experimental observations closely match theoretical predictions for the no-slip conditions. Therefore, by measuring the diffusion coefficient of a bead at varying separations from a surface, it is possible to estimate the surface drag and surface properties. For soft surfaces such as agar, the no-slip condition is expected to apply only partially given the porous nature of the substrate. Our expectation is that the larger the pore size of agar, the lower the surface drag. Since pore size decreases with agar concentrations, we expect that the surface drag will also increase with agar concentrations.

5.2. Methodology

Our approach was to measure the diffusion coefficient of a spherical particle as a function of its separation from agar. To do this, one must allow the bead to diffuse over a long period of time to collect adequate statistics. However, since diffusion may cause the particle to move far from the original separation, it is not possible to accurately calculate the diffusion coefficient at a given separation. This can be remedied with the aid of optical traps. The optically-trapped bead is positioned at a fixed separation from the surface (Figure 5-1A). The trap position is held fixed with respect to the surface for the duration of the experiment. Next, the trap is turned off and on repeatedly with a chopper that rotates at high speeds. When the trap is off, the bead is released and allowed to diffuse for a short period of time (Figure 5-1B). Before it can diffuse too far, the trap is turned back on, which causes the bead to return back to the same starting separation from the surface each time. By repeatedly releasing and re-trapping the bead with such blinking optical trapping, it is

possible to generate thousands of diffusion trajectories for the bead at a given separation, allowing adequate statistical sampling to calculate the diffusion coefficient at that separation. The entire experiment is repeated at a new separation. In this manner, the dependence of the diffusion coefficient on separation from the surface can be obtained.

5.2.1. System

A challenge in microscopy experimentation is the 2D nature of imaging. Assume that the x-y plane defines the focal plane. If a bead was optically trapped and translated along the z-axis to bring it close to the coverslip surface that is parallel to the focal plane, it is not straightforward to determine its separation from that surface. Hence, even though its diffusion coefficient along the x-y plane (lateral mode) can be measured, calculating the separation is a challenge, which is typically overcome by placing probes on the surface [20]. However, there are numerous practical challenges that prevent us from using such a technique to determine the separation when the surface is made of agar.

To overcome the above-mentioned challenge, a custom-made flow cell was designed that enabled us to orient the agar surface perpendicular to the focal plane. In this geometry, the distance between the bead and the surface was defined by the x-axis. Diffusion along this axis represented the transverse mode. Diffusion along the y-axis (parallel to the surface) represented the lateral model. Around 1000 particle trajectories were recorded at each separation by blinking the tweezers. Particle tracking techniques were employed to calculate the x-y position of the bead with respect to the surface. The

positions yielded the mean-squared displacements for each of the two modes for each separation. Finally, the two diffusion modes were calculated as a function of separation.

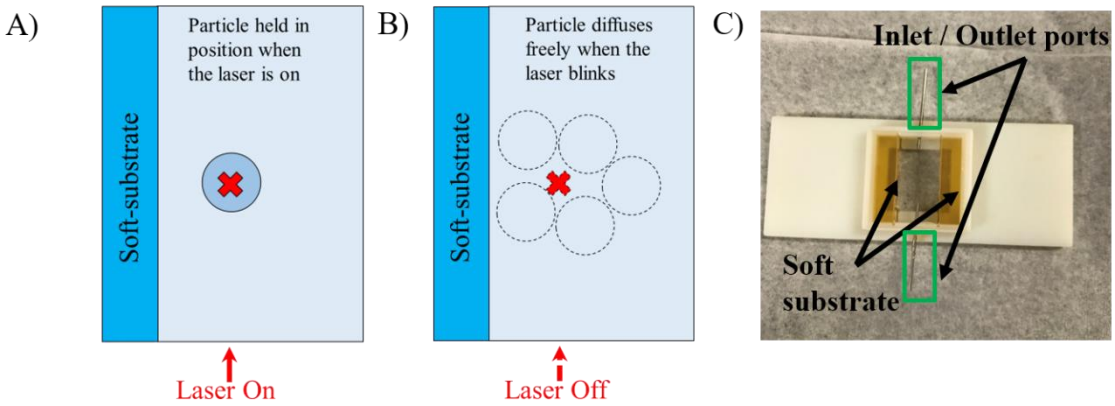

Figure 5-1 Optical trapping experiment. A) Blinking optical tweezer approach employed to estimate the diffusivities of spherical latex bead close to soft interfaces. The particle is held in position (at beam-center) while the laser is on (indicated by the cross). B) The particle diffuses away when the beam is blocked by the chopper wheel. C) Flow cell used for the experiment. Soft-substrate (2% agar; yellow surfaces in the figure) with vertical interface were generated in a custom flow cell, and inlet and outlet ports are shown in green boxes).

5.2.2. Experimental setup

Autoclaved media (2% Eiken agar, 10g/L Peptone, 5g/L NaCl, 3g/L Beef Extract) was prepared a day before the experiment and maintained at 60°C. It was poured into the custom flow cell on the day of the experiment (Figure 5-1C). Two vertically-placed coverslips (22mm by 22mm) ensured that the agar was restricted to the two sides of the cell as shown. After the agar was cured (~3h), the vertical coverslips were gently removed

to create empty space in the center, which was to be later occupied by a buffer containing latex beads. The flow cell was sealed with coverslips at the bottom and top using an ultraviolet curing adhesive (Norland Optical Adhesive# 611, Norland Products Inc.). An inlet and an outlet port were retained for the introduction of buffer containing 2-μm diameter (Cat# 19814, Polysciences Inc.). A syringe was employed to inject the bead suspension.

The optical traps were generated with a laser of wavelength of 976 nm (CW, 10W, Azur Light Systems, ALS-IR-132) at 0.51W power. A Nikon Eclipse Ti microscope with a high N.A. water immersion objective (60X, N.A.1.2) served as both the imaging and optical trapping system. An optical chopper wheel was introduced in the optical path (ThorLabs Optical System-MC2000; chopper wheel MCF1F2) and rotated at a frequency of 8Hz to generate blinking traps. The duration between two laser 'on' events was ~0.14s, during which the bead diffused. Videos were recorded using uEye cockpit (UI-3240LE-M-GL, IDS Imaging Development Systems GmbH).

5.2.3. Analysis

A single trajectory comprised of the displacement of the bead center between two blinking events captured over 10 camera frames. The particle position in each frame was calculated with sub-pixel accuracy using custom-written Matlab codes based on a standard approach [21]). If $\vec{r}$ denotes the position vector of the bead center then the total mean-squared-displacement (MSD) ($<\Delta r^2>$) is given by:

$<\Delta r^2>= <\Delta x^2> + <\Delta y^2>$……..Equation 1

where $<\Delta x^2>$ and $<\Delta y^2>$ are mean-squared-displacement in x and y axis, respectively. Thus,

$MSD = MSD_x + MSD_y$ ……Equation 2

where MSD_x and MSD_y reflect the transverse and lateral mode, respectively. The diffusion coefficient was calculated from the MSD using:

$MSD = 2dD\tau^{\alpha}$ …….. Equation 3

where, d is the dimensionality for the track (d=1, 2, or 3 for one, two, and three-dimensions), D is the diffusion coefficient, τ is the lag time, and α is the diffusion exponent. The diffusion coefficients along the modes were calculated from the slopes in the respective MSD plots. The transverse (or normal) mode diffusion coefficient was calculated using the following relation (Brenner's model [7]):

$$\frac{D_\perp}{D_0} = \frac{4sinh\alpha}{3}\sum_{n=1}^{\infty}\frac{n(n+1)}{(2n-1)(2n+3)} \times \left[\frac{2sinh[(2n+1)\alpha]+(2n+1)sinh[2\alpha]}{(2sinh\left[\left(n+\frac{1}{2}\right)\alpha\right])^2-((2n+1)sinh\alpha)^2} - 1\right]$$ ……Equation 4

where $\alpha = \cosh^{-1}\left(\frac{h}{R}\right)$, R is the radius of the sphere, h is the distance of the sphere center from the surface, $D_\perp$ is the diffusion coefficient in the normal direction and D_0 is the bulk diffusion coefficient. The diffusion coefficient in the **lateral (or parallel) mode** was calculated using (Faxen's model [6]) :

$$\frac{D_\parallel}{D_0} \approx 1 - \frac{9}{16}\frac{R}{h}$$ ……Equation 5

where $D_\parallel$ is the diffusion coefficient in the direction lateral (or parallel) to the surface.

5.3. Results and Discussion

To validate the approach, we first used glass as the surface since the dependence of diffusion coefficient on separation from a glass surface is well established [20]. We measured the diffusivities of the bead as a function of separation from the surface as discussed in Figure 5-2. The linearity of the MSD curve indicated the absence of hydrodynamic flows due to leakage or evaporation in the setup (Figure 5-2A). The diffusion coefficient was calculated from the slope for the MSD plot for each separation. The dependence of D on separation for the two modes is shown in Figure 5-2B. The transverse (red circles) and lateral (blue circles) measurements were in good agreement with the respective predictions.

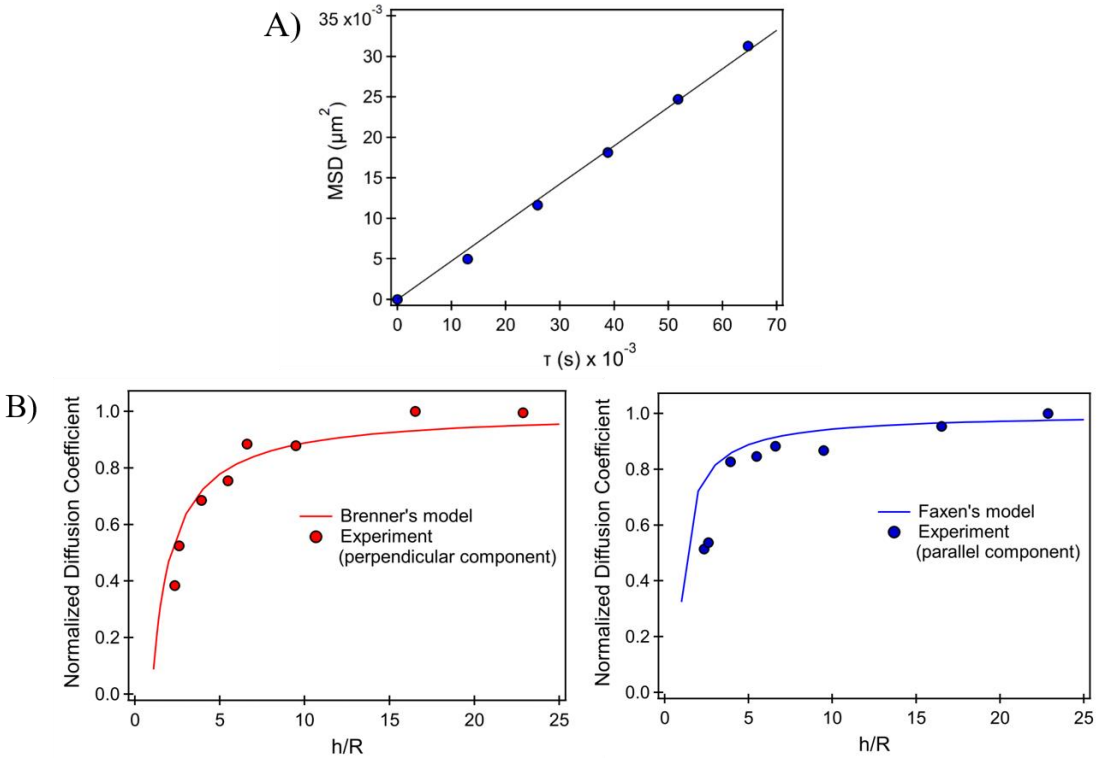

Figure 5-2 Mean-squared-displacement plot and diffusion coefficient for a no-slip wall. A) MSD plot. The plot shows mean-squared-displacement (MSD) plotted against lag time to calculate diffusion coefficient of 2-μm latex bead. Linearity of the curve can be used a guide to detect leakage or evaporation induces flows, which show up as non-linearity on the plot. B) Diffusion coefficient as a function of separation for a no-slip boundary. The variation of perpendicular and parallel component of the diffusion coefficient with separation distance from the coverslip is indicated in the left and right panel respectively. The experimental measurement are shown by red and blue data points for transverse and lateral components respectively. Theoretical predictions for no-slip boundary are indicated by the solid curves (red: Brenner's model, blue: Faxen's model).

5.3.1. Variation of diffusion coefficient with separation from soft-substrate

Next, we used the blinking optical tweezer to study the effect of surface drag in the case of 2% agar. The variation of the diffusion coefficient in transverse mode (red circles) and lateral mode (blue circles) as a function of separation from the agar surface is

indicated in Figure 4. Contrary to our expectations, these experimental values also agreed with the predictions of the no-slip model (red and blue curve). This suggests that 2% agar offers similar resistance to the diffusion of a 2-μm particle as a solid glass surface.

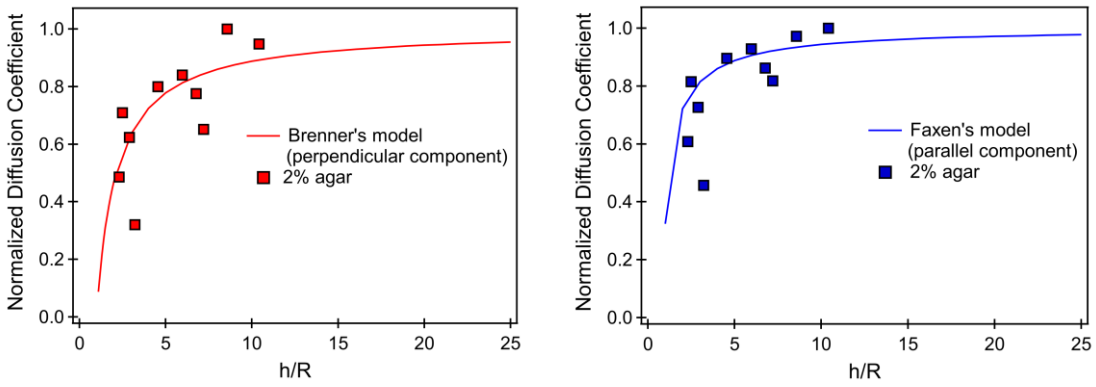

Figure 5-3 Diffusion coefficient as a function of separation for a partial-slip boundary. The variation of perpendicular and parallel component of the diffusion coefficient with separation distance from 2% Eiken agar is indicated in the left and right panel respectively. The experimental measurement are shown by red and blue data points for transverse and lateral components respectively. Theoretical predictions for no-slip boundary are indicated by the solid curves (red: Brenner's model, blue: Faxen's model).

The reason for this could be that the pore size of 2% agar is much smaller than the diameter of the bead. Although measurements of the pore size variation with Eiken agar concentration was not available in the literature, a crude approximation of the behavior of the agar with agarose (a purified component of the agar) was employed. The pore size for agarose ranges from 500-1200 nm for 0.5% agarose, and reduces to 100-200 nm for 2% agarose [22]. It could be that swarming is prevented on such high agar concentration

surfaces due to the increased drag. More measurements are needed to make definitive conclusions.

5.3.2. Future directions

Future investigations are anticipated to help explain the effect of surface drag on the initiation of swarming. Such measurements are likely to help researchers characterize soft interfaces with probe beads. To best of our understanding, there are no available measurements or models of surface drag near a soft-substrate, with only one available study investigating the simulation near a partial-slip conditions using two fundamental singularities of Stokes flow-the point force (Stokeslet) and the point force [4].

5.4. Conclusions

In this work, we employed blinking optical tweezers to measure normal mode of diffusion coefficient of probes near surfaces. We first validated our approach by measuring diffusion coefficient of a bead as a function of separation from a no-slip boundary. The results were in a good agreement with the model predictions. Next, we measured diffusion coefficient of the probes in proximity of 2% agar surface and found that it matched the predictions for no-slip condition, suggesting that 2% agar may offer a similar frictional resistance to cell movements as a solid non-porous surface.

5.5. References

1. Kearns, D.B., *A field guide to bacterial swarming motility.* Nat. Rev. Microbiol., 2010. **8**(9): p. 634-44.

2. Copeland, M.F. and D.B. Weibel, *Bacterial Swarming: A Model System for Studying Dynamic Self-assembly.* Soft Matter, 2009. **5**(6): p. 1174-1187.

3. Lisicki, M. and G. Nägele, *Colloidal Hydrodynamics and Interfacial Effects*, in *Soft Matter at Aqueous Interfaces*, P. Lang and Y. Liu, Editors. 2016, Springer International Publishing: Cham. p. 313-386.

4. Lauga, E. and T.M. Squires, *Brownian motion near a partial-slip boundary: A local probe of the no-slip condition.* Physics of Fluids, 2005. **17**(10): p. 103102.

5. Lorentz, H.A., *Abhandlungen über theoretische Physik*. 1907, Leipzig; Berlin: B.G. Teubner. 489 p.

6. Faxen, H., Ark. Mat., Astron. Fys., , 1924. **17**(No. 27).

7. Brenner, H., *The slow motion of a sphere through a viscous fluid towards a plane surface.* Chemical engineering science, 1961. **16**(3-4): p. 242-251.

8. Goldman, A.J., R.G. Cox, and H. Brenner, *Slow viscous motion of a sphere parallel to a plane wall—I Motion through a quiescent fluid.* Chemical Engineering Science, 1967. **22**(4): p. 637-651.

9. Goldman, A.J., R.G. Cox, and H. Brenner, *Slow viscous motion of a sphere parallel to a plane wall—II Couette flow*. Chemical Engineering Science, 1967. **22**(4): p. 653-660.

10. Pralle, A., et al., *Local viscosity probed by photonic force microscopy.* Applied Physics A: Materials Science & Processing, 1998. **66**: p. S71-S73.

11. Faucheux, L.P. and A.J. Libchaber, *Confined Brownian motion.* Physical Review E, 1994. **49**(6): p. 5158-5163.

12. Sadr, R., et al., *Diffusion-induced bias in near-wall velocimetry.* Journal of fluid mechanics, 2007. **577**: p. 443-456.

13. Huang, P. and K.S. Breuer, *Direct measurement of anisotropic near-wall hindered diffusion using total internal reflection velocimetry.* Physical review E, 2007. **76**(4): p. 046307.

14. Huang, P., J.S. Guasto, and K.S. Breuer, *The effects of hindered mobility and depletion of particles in near-wall shear flows and the implications for nanovelocimetry.* Journal of Fluid Mechanics, 2009. **637**: p. 241-265.

15. Lobry, L. and N. Ostrowsky, *Diffusion of Brownian particles trapped between two walls: Theory and dynamic-light-scattering measurements.* Physical Review B, 1996. **53**(18): p. 12050.

16. Ishii, K., T. Iwai, and H. Xia, *Hydrodynamic measurement of Brownian particles at a liquid-solid interface by low-coherence dynamic light scattering.* Optics express, 2010. **18**(7): p. 7390-7396.

17. Plum, M.A., et al., *Probing dynamics at interfaces: resonance enhanced dynamic light scattering.* Optics express, 2009. **17**(12): p. 10364-10371.

18. Holmqvist, P., J.K. Dhont, and P.R. Lang, *Colloidal dynamics near a wall studied by evanescent wave light scattering: Experimental and theoretical improvements and methodological limitations.* The Journal of chemical physics, 2007. **126**(4): p. 044707.

19. Michailidou, V., et al., *Dynamics of concentrated hard-sphere colloids near a wall.* Physical review letters, 2009. **102**(6): p. 068302.

20. Lele, P.P., et al., *Colloidal diffusion and hydrodynamic screening near boundaries.* Soft Matter, 2011. **7**(15): p. 6844-6852.

21. Crocker, J.C. and D.G. Grier, *Methods of digital video microscopy for colloidal studies.* J. Colloid Interf. Sci., 1996. **179**(1): p. 298-310.

22. Narayanan, J., J.-Y. Xiong, and X.-Y. Liu. *Determination of agarose gel pore size: Absorbance measurements vis a vis other techniques*. in *Journal of Physics: Conference Series*. 2006. IOP Publishing.

6. CONCLUSIONS AND FUTURE WORK

6.1. Conclusions

Recent work has shown that the bacterial flagellar motor is able to regulate its structure in order to adapt to long-lived perturbations in the cell's thermal, chemical, electrical, and mechanical environments. These flagellar adaptations play a key role in invasion, colonization, and pathogenesis. However, the mechanisms of flagellar response, especially to mechanical stimuli, were unknown. I have addressed this key gap in knowledge in my work.

In Section 2, we reviewed the evidence for mechanosensing in select bacterial species with a focus on mechanosensitive molecular motors. Mechanosensing can help a bacterium sense its adhesion to a surface provided there is a change in the mechanical load. We discussed two prominent mechanosensitive appendages, the pilus and the flagellum, which experience viscous load changes when attached to a surface. For the load change to persist, their respective motors need to continue generating a force or a torque. The ability to sense differences in the signs and magnitudes of the load change, the ability to detect temporal persistence in mechanical stimuli, and a high sensitivity to mechanical signals are key attributes of effective bacterial mechanosensors.

In Section 3, we experimentally tested our model to explain the remodeling of flagellar stators under mechanical stress. Our findings are consistent with the notion that higher torque generated by the stators exposes cryptic binding sites that strengthen their association to the rotor. Our analytical model that incorporated an exponential dependence

of the stator unit's off-rates on the torque delivered was able to fit previously measured load-binding curves accurately. The combined experimental and analytical results presented in this work represent the first steps towards establishing a plausible mechanism for stator-mechanosensitivity and motor-adaptation.

In Section 4, we utilized flagellar motor output as a probe for the chemotactic responses of *E. coli* to indole, a key gastrointestinal tract microbiota metabolite. Indole regulates numerous bacterial phenotypes including stress response, drug resistance and biofilm formation. In this work, we dissected the mechanisms underlying chemotaxis signaling in response to indole in *E. coli*. We exposed *E. coli* to a range of indole concentrations and measured the dynamic responses of individual flagellar motors to determine the mechanisms of chemotaxis. We found that wild-type *E. coli* cells exhibited a time-dependent inversion response from repellent to attractant mediated by opposing responses of two major chemoreceptor. We also found that flagellar motor itself mediated a repellent response independent of the receptors. Furthermore, our chemotaxis assays revealed that wild-type cells were attracted to regions of high indole concentration if they had previously adapted to indole but were otherwise repelled. Overall, our results suggest that indole acts to spatially segregate cells based on their state of adaptation and may help guide the development of niches in the GI tract.

In Section 5, we tested the underlying assumption that flagella and the cells experience higher drag near soft surfaces such as agar by measuring surface drag as a function of agar concentrations. We employed blinking optical tweezers to measure the

diffusion coefficient of probes near surfaces along the normal and transverse modes. A custom-made flow cell was designed that enabled us to orient the agar surface perpendicular to the focal plane. We validated our approach by measuring diffusion coefficient of a bead as a function of separation from a no-slip boundary. The results were in a good agreement with the model predictions. Next, we measured diffusion coefficient of the probes in proximity of 2% agar surface and found that it matched the predictions for no-slip condition, suggesting that 2% agar may offer a similar frictional resistance to cell movements as a solid non-porous surface.

Overall, we took various biophysical approaches to understand the mechanisms of adaptive response of bacterial flagellar motor to mechanical and chemical stimuli.

6.2. Future directions

Our model for stator remodeling is based on the idea of a catch-bond; tensile forces increase the binding affinity of ligands to their receptors. There is additional evidence for this idea; recent experiments by Wadhwa et al, 2019 indicate that the unbinding rates of stator molecules decrease as torque increases, and the on-rates decrease with speed when the motor speeds are high. However, much work needs to be done, especially to elucidate specific binding sites within the stator units which confers mechanosensitivity. Specifically, what are the domains of MotA and MotB involved in the remodeling? It could be that the cytoplasmic domain of MotA domain is involved, considering it interacts with the rotor where the load arises. One approach to test this idea is to measure the torque-speed curve and stator-remodeling characteristics for MotA mutants. Similar experiments

with MotB mutants with altered ability to attach to the peptidoglycan layer will provide further insights into torque-dependent mechanosensing. Lastly, how is the mechanosensitive nature of the motor maintained between CCW and CW switching state? This is interesting since there is an asymmetry in the torque generated in the two directions.

Tar and Tsr are the two major receptors that mediate opposite responses to indole. However, more work is needed to determine the local determinants in the Tar and Tsr receptors that mediate these responses. Indole could elicit opposing responses by diffusing into cytoplasmic membrane to influence the equilibrium position or structural stability of the transmembrane helices, thereby modulating the packing stability of the HAMP bundle in a manner similar to phenol (Pham et al, 2011). Future investigation by using different chimeras and point mutants of Tsr and Tar, as approached previously by Pham et al, 2011 to determine the sites involved phenol sensing, would help isolate the interacting domains. These include the periplasmic, transmembrane and cytoplasmic domains of the receptors Moreover, molecular dynamics simulations along the line of recent work of Bai et al, 2018 would help computationally predict the receptor domains of receptors that mediate the indole response. Beyond establishing the molecular determinants in indole sensing, other experimental observations need further investigation. We observed a receptor mediated response and a network-independent flagellar response to indole. However, the wild-type cells exhibited precise adaptation in response, suggesting the two responses do not act simultaneously. This raises the question if there are any mechanisms that switch responses

between the two. Second, our preliminary experiments with tethered cells (sticky mutant) of CCW mutant did not show a rotational speed reduction upon 2mM indole stimulation, while there was a significant reduction in the swimming speed of a CCW mutant. This raises a conundrum, as the former observation suggests no change in PMF (Gabel et al), whereas the latter argues for a reduction in PMF. More experiments, taking into account the dose- and load-dependence, will be required to resolve this paradox. Finally, future work is required to establish the physiological role of indole to test the relevance and validity of our spatial segregation model of indole action in-vitro and in-vivo. Moreover, the physiological response and signal integration in cells experiencing multiple chemical compounds which invoke opposing phenotypic responses (for e.g. indole and norepinephrine) is an interesting problem for further investigation (Lopes et al, 2018).

Future work could focus on determining the surface drag as a function of agar concentrations, especially around the range of 0.45% agar, which is conducive for swarming. Additionally, to the best of our understanding there are not many available theoretical models that predict surface drag near a soft-substrate. One simulations-based study modeled the case with partial-slip conditions using two fundamental singularities of Stokes flow-the point force (Stokeslet) and the point force. These theoretical predictions would provide a useful guide to validate the experimental results near soft-substrates. Additionally, we used spherical beads as a model system; however, swarming cells like *E. coli* are rod shaped. This would result in anisotropic drag forces. Hence, future investigations with anisotropic particles would provide valuable insights into the surface

drag experienced by the bacteria. Moreover, on the leading edge of a swarming plate, bacteria swarm with soft-substrate at bottom and a thin-fluid film on the top. This could be taken into account with a combination of interfacial geometries and our flowcells.

Lastly, we focused on mechanical and chemical stimuli and cell responses. However, in a real environment, bacteria encounter multiple types of stimuli simultaneously. For example within the gut, bacteria experience multiple types of chemical signals in presence of highly viscous mucosal layers. Future work is needed to understand how bugs integrate these complex signals to initiate colonization and virulence.

6.3. References

1. Wadhwa, N., Phillips, R. and Berg, H.C., 2019. Torque-dependent remodeling of the bacterial flagellar motor. Proceedings of the National Academy of Sciences, 116(24), pp.11764-11769.
2. Pham, H.T. and Parkinson, J.S., 2011. Phenol sensing by Escherichia coli chemoreceptors: a nonclassical mechanism. Journal of bacteriology, 193(23), pp.6597-6604.
3. Bi, S., Jin, F. and Sourjik, V., 2018. Inverted signaling by bacterial chemotaxis receptors. Nature communications, 9(1), p.2927.

4. Gabel, C.V. and Berg, H.C., 2003. The speed of the flagellar rotary motor of Escherichia coli varies linearly with protonmotive force. Proceedings of the National Academy of Sciences, 100(15), pp.8748-8751.
5. Lopes, J.G. and Sourjik, V., 2018. Chemotaxis of Escherichia coli to major hormones and polyamines present in human gut. The ISME journal, 12(11), p.2736.

APPENDIX A

LAMBDA RED RECOMBINATION PROTOCOL FOR ALLELE EXCHANGE

A1. Introduction

In this appendix, I describe the Lambda Red recombination ("recombineering") technique we have employed for generating mutants in the Lele lab. It is a frequently used technique in genetic engineering that utilizes phage-derived Lambda Red recombination system to generate genetic modifications like precise insertion, deletion, and point mutations in *E. coli* and other bacteria [1-6]. Specifically, this method involves introduction of a foreign, linear piece of DNA in bacteria with sufficient homology in presence of three phage-derived recombinases-Gam, Exo and Beta [7]. The linear piece of DNA is designed to have a degree of homology to the original DNA (as indicated by the green regions as shown in Figure 1A). A homology of at least 35-50 bp on either side of the flanking region is typically employed [1, 4]. Gam inhibits RecBCD and SbcCD nucleases from digesting the linear piece of DNA [8]. Exo degrades the linear DNA from 5' to 3' direction, leaving behind a partial double stranded DNA with single-stranded DNA in the cleaved region [3, 9]. Beta binds to the single-stranded regions generated by Exo, and promotes its annealing to the homologous target site [3-5]. This is shown in Figure A1B. Recent work suggest that the integration of this DNA fragment takes place as an Okazaki fragment on the lagging strand during DNA replication [7].

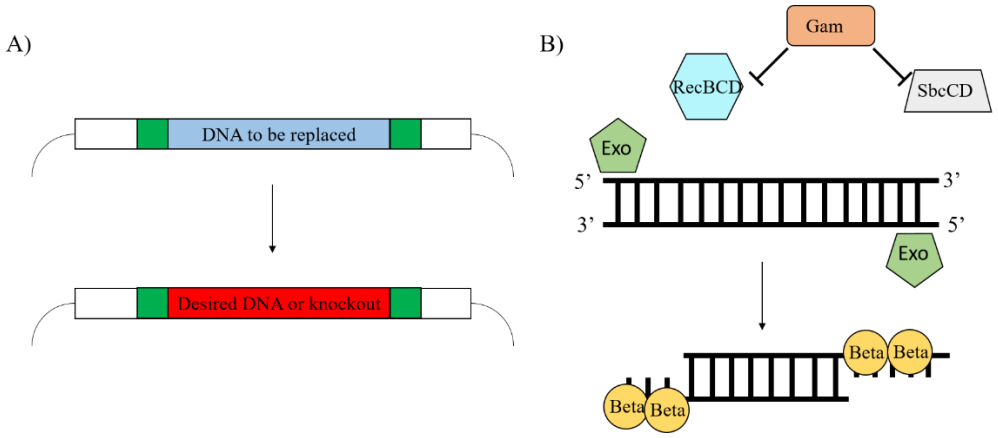

Figure A1. Overview of Lambda Red recombination. A) Overview of the overall goal of the Lambda Red recombination. The linear piece of DNA is designed to have a degree of homology to the original DNA as indicated by the green regions. B) Components of Lambda Red system. Three phage-derived recombinases-Gam (orange), Exo (green) and Beta (yellow) are involved in processing the foreign, linear piece of DNA. See text for details.

A2. Experiment overview

We used a two-step approach [1] for the experiments as shown in Figure A2.

Step 1. The strain of interest is transformed with pKD46, a temperature-sensitive plasmid carrying the Lambda Red recombinase genes and inducible with L-arabinose. The strain is grown at 30º C in LB with Amp and ~0.1% L-arabinose to early exponential growth phase. The linear DNA for the first cross is obtained from a PCR reaction with pKD45 as template and introduced in the cell via electroporation (pKD45 encodes a kanamycin resistance cassette and a ccdB toxin under the control of a rhamnose-inducible promoter). We typically name primers used for pKD45 reactions with 'RED' prefix or suffix. Alternatively, if there is already a successful *kan-ccdB* insert available in the lab strain list, then use the primers to amplify the region and use this DNA for transformation. In

either case, it is important to use PCR purified DNA of high quality (260/280 ratio ~1.8) and high concentration (>100 ng/μL) as we found that this yields more number of successful colonies. The workflow of replacement of the target gene with *kan-ccdB* occurs is illustrated in Figure 2.

Preparation for Step 2.

Cells which have lost the original DNA due to replacement with *kan-ccdB* gene are selected from either Kan plates or Kan-Amp plates. Here, it is important to verify whether the *kan-ccdB* has crossed in. This is done by running a PCR and checking on the gel. Two set of design primers are used for carrying out this diagnostic:

1. The first primer pair is such that they start from regions outside the target DNA. Usually the DNA band size will be ~1600-2000 bp depending on primer design.
2. A second pair of primer pair with one primer in the kan-ccdB region and the other in a region upstream or downstream of the site of modification in genome is used if the region being replaced is same size as *kan-ccdB* cassette (~1600bp).

Motility of RP437 strain provides us with a powerful phenotype that can be used to verify if genetic manipulation somehow interfered with the strain creation process. To use this to our advantage, we check the motility of the *kan-ccdB* intermediates which has successfully passed the diagnostic PCRs under the microscope. For example, insertion of *kan-ccdB* gene in *tsr* gene should not interfere with motility of the strain. Therefore, any non-motile intermediate strain in this case should be discarded and a motile strain should be used for any steps to follow. However, this luxury of testing motility of an intermediate

strain is not available when modifying genes whose products are responsible for motility or if the intermediate gene exerts a polar effect on motility-associated genes. The final intermediate strain obtained above is then re-transformed with pKD46. Note: pKD46 re-transformation step is skipped entirely with kan-amp selections.

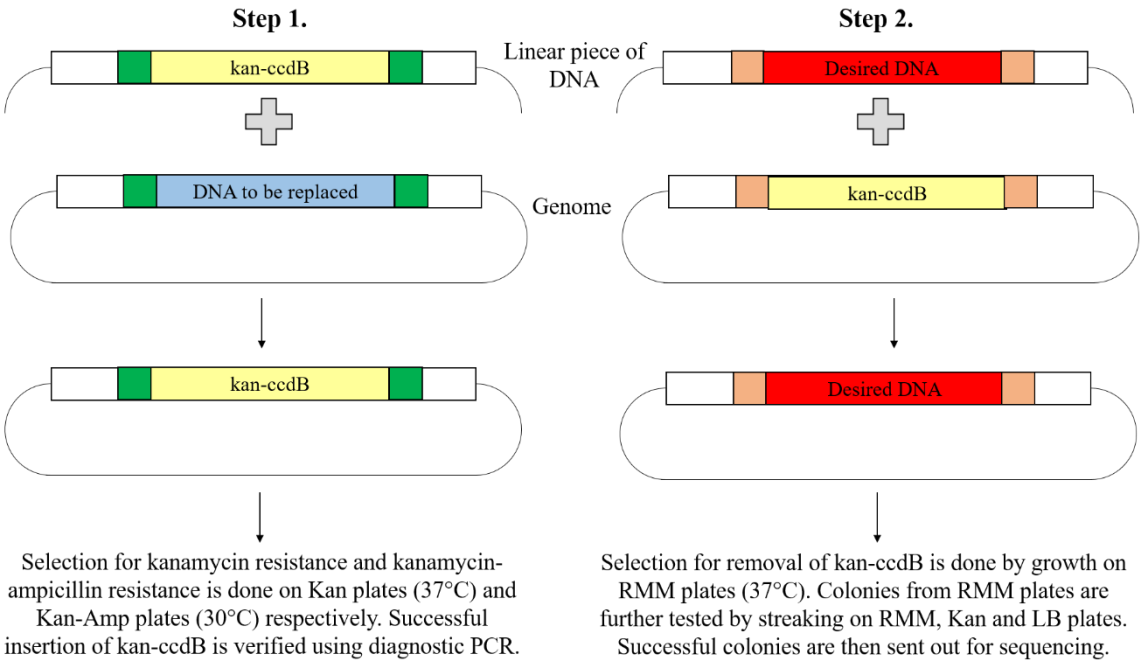

Figure A2 Overview of the two step Lambda Red recombination. Step 1. Linear piece of DNA in this step is obtained through a PCR reaction using the plasmid pKD45 (yellow piece) as template. The homology (green stubs) is achieved by correct primer design, usually with 40 bp on either ends. Upon successful replacement, genome carries kanamycin resistance (kan gene) and will not grow on rhamnose plates (*ccdB* suicide gene). Step 2. Here, linear piece of DNA is obtained through a PCR reaction with primer design dictating the length of homology, shown here in light orange. Yellow strip on the genome is the *kan-ccdB* part obtained from pKD45. In theory, there is no limit to the degree of homology one can use in step 2, especially when deleting genes (see text for details on reported maximum lengths successfully employed in practice). Upon integration of the desired DNA in the genome, cells lose the *ccdB* gene and can now grow on rhamnose plates, allowing selection of the appropriate colonies.

Step 2: This step involves crossing out of the DNA (deletion) or crossing in a DNA with desired characteristic (Figure A2). The *kan-ccdB* strain with pKD46 is grown at 30º C, LB, Amp induced with L-arabinose as in Step 1. Freshly made electrocompetent from exponential growth phase are electroporated with the desired linear DNA. The cells are then cured at 37°C for 3h; this also excludes pKD46 from the strain. Cured cells are washed three times with 1X RMM liquid media, pelleted and plated on L-rhamnose plates. The colonies on rhamnose plates are re-streaked on Kan, LB and RMM plates for further testing. The final streaks are on LB and grown at 37°C. If allele exchange is successful, the strain loses Kan resistance and is able to grow on RMM plates since *ccdB* gene is also lost. This allows selection for the correct cross in (or out). A detailed description of the experimental details is provided under the sub-heading 'Detailed experimental protocol.'

A3. Deletions achieved in the lab

Using our protocol I was able to successfully generate intermediate strains, deletions and mutations in *tsr, tar, fliL, fliG, motB and cheRB* region of the genome in various backgrounds (strains with a prior mutations/deletions) in RP437, and the lab in general has succesfully employed it to generate other range of genetic modifications. Of special note here is the *tar* mutation/deletion. Generating the *tar* deletion turned out trickier than other deletions. We first had challenges in inserting the *kan-ccdB* in the *tar* region, but this was overcome by playing with regions of homology of the primers with *tar* region. However, even with a successful intermediate I was not able to generate a

deletion in the *tar* region. To ultimately generate a successful deletion, we used an intermediate strain with *kan-ccdB* in the *cheRB* region and employed a linear fragment of DNA with *tar* deletion (we retained 30bp from the original sequence) combined with intact *tap* and *cheRBY* sequence. This fragment was about ~4.8kbp in length and helped us generate our final deletion which was verified using sequencing. Similarly, in a *tar* deletion background, the *kan-ccdB* insertion in *tsr* region was replaced with a ~5kbp fragment.

A4. Perspective

Lambda Red technique is an extremely powerful tool which has been successfully used to make genetic modifications in *E. coli* (both non-pathogenic [1, 2] and pathogenic strains [10-12]) and in bacteria like *Salmonella* [13], *Bacillus* [14], *Vibrio* [15], *Pseudomonas* [16] and others. Despite its usefulness, the technique has often yielded variable frequency in my own experience, with some regions of genome easier to target than others (e.g. *frd* and *tar* were more difficult to manipulate than other regions listed above). Moreover, same region (e.g. *tsr*) became more difficult to delete in strain with a previous deletion of *tar* compare to wild-type. Lambda Red technique is a stochastic process [17] and the recombination frequency of gene insertion is rather low (~$5x10^{-4}$ recombinants per viable cell) [2] . The recombination frequency is dependent on multiple factors like cell growth cycle, lengths of the homology arms, DNA concentration, use of oligonucleotides versus double stranded DNA, and presumably the region of target gene [5, 7].

Lambda Red recombineering with fragments from up to 3-4 kbp are reported in the literature, although another study specifically investigating the effect of length on recombineering on size found these sizes (and larger) to be prohibitively difficult due to nonspecific recombination of fragment into sites other than the target ([18, 19]).

The use of rational design approaches are now paving way to incorporate larger fragments of DNA into (cite dissertation) from ~9-15kbp [18, 20] and with up to 15% deletion of *E. coli* genome [21]. Specifically, improved understanding of the mechanisms is being used for rational design and improvements in Lambda Red [7].

Recent work has shown that the use of oligonucleotides strand is more effective in smaller deletions whereas double stranded is more effective for larger deletions [7, 22-25]. Other work from the same lab showed that phosphorothioate (PT) bonds to protect 5' end of lagging-targeting strand results in a significant improvement of recombination frequency, while the PT bonds on leading targeting strand reduce the recombination frequency, presumably through inhibiting Lambda Exo from the lagging-targeting intermediate[24]. A later work from the authors shows the detrimental and beneficial role of the PT bonds depends on the background nuclease activity in the recombineering strain [7]. Moreover, their work showed removal of endogenous nuclease (or exonuclease) ExoVII results in significantly improved double-stranded DNA recombination frequency [24]. Based on their work, the limiting factors for Lambda Red recombination are the number of oligonucleotides within the cell and the amount of accessible ssDNA at the laggings strand.

Recent advances in the mechanistic understanding, modifications, and improvements in Lambda Red along with incorporation of newer techniques are being used to increase the efficiency of Lambda Red recombination [5, 26, 27]. A recent work coupling CRISPR/Cas9 with Lambda Red was able to successfully deleted ~19kbp from *E. coli* chromosome [28]. Thus, an improved understanding of the mechanism and rational design combined with new emerging techniques has tremendous scope to improve genetic modifications in bacterial chromosome.

A5. Detailed experimental protocol

1. Transformation of strain with pKD46

- Start an overnight culture in 5mL LB at 37ºC. Grow the day cultures in 25mL LB at 37ºC to an OD of 0.5-0.6.
- Make strain electro-competent (EC) and transform with pKD46. Use ~ 75µL of EC cells and 1.5uL of ~50-60ng/µL of plasmid (pKD46). Save the remaining EC cells in 10% glycerol at -80ºC.
- Cure the transformed cells, suspended in SOC media (1 ml), for 30min-1h at 30ºC. pKD46 has a temperature-dependent origin of replication, so it is necessary to grow the cells carrying pKD46 at 30ºC and ampicillin.
- Plate different dilutions on LB+Amp plates and store overnight at 30 ºC:
  - 100µL cured cell culture
  - 25µL cured cell culture +75µL LB
  - 8µL cured cell culture +92µL LB

- Re-streak the isolated colonies on LB+Amp plates and grow an OC (LB+Amp) from a single colony the next day. Grow at 30 ºC, not 37ºC.

2. Transformation with RED DNA

- Store the strain at -80C and label it strain name-pKD46. Start a day culture in a 250mL flask by inoculating 25mL of LB with 250µL of OC. Add 50µL of 50mg/mL ampicillin stock and 500uL of 10%(w/w) sterile filtered L-Arabinose. Ensure the cap of the flask is not tight and there is plenty of aeration, grow at 30ºC to an OD of 0.6-0.7. To ensure aeration, you may use an aluminum foil or saran wrap to cover the flask.
- Make cells electro-competent by washing them in cold water (25 ml) three times. Before the third and final wash, place the SOC medium in 30ºC incubator.
- Electroporate 75µL of electrocompetent cells with ~200-300ng of λ-red DNA. Note: Keep a record the time constant values! Successful transformations have had a time constant of 4.6 -5.0. Immediately cure the cells with 1mL SOC media. Split the 1 ml culture equally (500uL) into two test-tubes. Note: The λ-red DNA comes by amplifying the kan-ccdB allele in pKD45, see step 3 for more information.
- Cure one at 30ºC and the other tube at 37ºC for 3h. Keep 3 LB-Kan-Amp plates at 30ºC and 3 LB-Kan plates at 37ºC for at least 20-30min before utilizing them for plating in the next step. Remember that Kan plates will be warmed at 37 ºC and kan-amp plates at 30 ºC.

- Spread the entire 30ºC culture on the 3 LB-KanAmp plates and store overnight at 30 ºC. Similarly, spread the other tube on LB-Kan plates and store overnight at 37ºC. Suggested volumes are 150µL, 150µL and 200µL.
- Next day, streak isolated and uniform colonies on LB-Kan-Amp plates. To do this, first draw 6 equal spaces (using a marker) on each plate. Then for each space, select one colony and apply one primary streak, discard the toothpick. Select a new toothpick and apply two streaks, dragging the cells from the primary streak. Discard the toothpick. Finally, pick a fresh toothpick and then apply three tertiary streaks, dragging cells from the secondary streak. Store at 30ºC to test for false positives. Do the same for LB-Kan plates and store at 37 C.

3. RED PCR

- Run 3 PCR reactions, 50 ul each (use NEB Phusion Mastermix-High Fidelity) with RED primers to isolate the linear piece of DNA (with Kan-ccdB cassette) from pKD45.
- Run the gel with the 3 reactions in adjacent lanes. Cut the three DNA bands (should be ~ 1650 bp) together and purify in the same purification column. Final concentration should be ~ 75-80 ng/µL.

4. Growth on LB-Kan-Amp/LB-Kan plates

A diagnostic PCR (use Econotaq) reaction is carried out on the colonies that have grown robustly on the new Kan or Kan-amp plates, using primers that lie well outside the anticipated RED insertion- do not use the same RED primers that you employed in Step 3! If the cells take longer than 16-20 hours to grow (to individual colonies of ~ 1-1.5 mm diameters), something's probably wrong – speak with Dr. Lele before proceeding further. Remember to run the diagnostic for kan and kan-amp colonies in parallel. Run gel electrophoresis to confirm the insertion of the RED DNA*. The ideal result is that one of the kan-amp colonies is a positive (contains kan-ccdB in the correct region). This saves you an extra step - if not, use colonies that are positive from the kan colonies and transform that colony with pKD46. *Note: Streak out the kan-ccdB positive colony (or colonies) from the diagnostic step on RMM plate to ensure no growth on RMM plates. It is important to only use the colonies that do not grow on RMM plates for the next steps as the number of false positives severely increases in next step if this not verified.

Grow the intermediate strain (strain + kan-ccdB + pKD46) in an overnight culture (5ml) in LB+Kan+Amp at 30ºC. Next day, store the strain as frozen stock at -80ºC. A 250uL overnight culture is then introduced in 25mL of fresh LB medium (supplemented with Kan and Amp) and 500µL of 10% sterile-filtered L-arabinose. Cells are grown to an O.D. of 0.6-0.7, and made electro-competent. The EC cells (75µL) are then electroporated with 200-300ng of the desired DNA (the actual desired allele). Add 1mL of SOC medium

immediately after electroporation and the cells are cured at 37ºC for 3h. Remember to keep the SOC medium at 37ºC for 30minutes prior to electroporation.

Note: Like RED PCR step, we run three PCR reactions to obtain the desired DNA, at a concentration of at least 75-80ng/µL.

5. Selecting for desired deletion/insertion

The cured cells are then centrifuged at 1500g for 7min and the supernatant is discarded. The cells are then given a sequential washing of 3mL, 2mL and 1mL of rhamnose buffer (brought to 37ºC) at 1500g for 5 min. The pellet obtained after the last step is re-suspended in 300µL of rhamnose buffer. Three RMM plates (maintained at 37ºC half an hour prior to plating) are each gently plated with 100uL of above cell suspension, and incubated at 37ºC for ~40-48h. Multiple white colonies should be visible (~ 1 mm diameter). Select colonies that are at least ~ 1 mm in diameter. Ignore pin-point like colonies, they're probably false positives. Select suitable colonies streak them in the following manner. First, draw at least 9 equal spaces on the backs of 1 Kan, 1 RMM and 1 LB plate. Label each space with a unique letter or number. For example, '1' on the kan, '1' on the RMM, '1' on the LB plate. You will streak a single colony in these identically labeled spaces on the 3 types of plates. To do this, select a single suitable colony from the original rhamnose plate. Use a toothpick to pick the colony gently and apply a primary streak first on rhamnose plate in space '1'. Then use the same pick to apply a primary streak on the Kan plate in space '1' and then finally a primary streak on the LB plate in space '1'. Then discard the toothpick. Select a new colony and do the same for space '2'

and so on. Once all colonies of interest have been streaked in this manner, select fresh toothpicks and apply two secondary streaks on all the primary streaks in the kan and LB plates. Make sure that you are not using the same toothpick for different colonies (e.g. '1' and '2'). There should be no cross-contamination. If there are 9 different colonies, you'll have used 9 fresh picks for the Kan plate and 9 fresh picks for the LB plates. Now do the same for tertiary streaks. Around 20-30 colonies are typically tested.

The colonies that do not grow on Kan plates are the desired positive colonies. They should grow on RMM and LB. A diagnostic PCR and gel is then run to ensure the correct deletion/insertion is in place. The purified DNA cab be sent to Eurofins Genomics for sequencing. Upon confirmation of sequencing results, an overnight culture of the correct colony is grown in LB (only) at 37°C and frozen stock stored at -80ºC the following day.

A6. References

1. Datsenko, K.A. and B.L. Wanner, *One-step inactivation of chromosomal genes in Escherichia coli K-12 using PCR products.* Proc. Natl Acad. Sci. USA, 2000. **97**(12): p. 6640-6645.

2. Yu, D., et al., *An efficient recombination system for chromosome engineering in Escherichia coli.* Proceedings of the National Academy of Sciences, 2000. **97**(11): p. 5978-5983.

3. Court, D.L., J.A. Sawitzke, and L.C. Thomason, *Genetic engineering using homologous recombination.* Annual review of genetics, 2002. **36**(1): p. 361-388.

4. Sharan, S.K., et al., *Recombineering: a homologous recombination-based method of genetic engineering.* Nature protocols, 2009. **4**(2): p. 206.

5. Murphy, K., *λ Recombination and Recombineering.* EcoSal Plus, 2016. **7**(1).

6. Thomason, L.C., et al., *Recombineering: genetic engineering in bacteria using homologous recombination.* Current protocols in molecular biology, 2014. **106**(1): p. 1.16. 1-1.16. 39.

7. Mosberg, J.A.W., *Studying and Improving Lambda Red Recombination for Genome Engineering in Escherichia coli*. 2013.

8. Kulkarni, S.K. and F.W. Stahl, *Interaction between the sbcC gene of Escherichia coli and the gam gene of phage lambda.* Genetics, 1989. **123**(2): p. 249-253.

9. Poteete, A.R., *Involvement of DNA replication in phage lambda Red-mediated homologous recombination.* Molecular Microbiology, 2008. **68**(1): p. 66-74.

10. Murphy, K.C. and K.G. Campellone, *Lambda Red-mediated recombinogenic engineering of enterohemorrhagic and enteropathogenic E. coli.* BMC molecular biology, 2003. **4**(1): p. 11.

11. Tuntufye, H.N. and B.M. Goddeeris, *Use of lambda Red-mediated recombineering and Cre/lox for generation of markerless chromosomal deletions in avian pathogenic Escherichia coli.* FEMS Microbiology Letters, 2011. **325**(2): p. 140-147.

12. Egan, M., et al., *Lambda Red-mediated Recombineering in the Attaching and Effacing Pathogen Escherichia albertii.* Biological procedures online, 2016. **18**: p. 3-3.

13. Husseiny, M.I. and M. Hensel, *Rapid method for the construction of Salmonella enterica serovar Typhimurium vaccine carrier strains.* Infection and immunity, 2005. **73**(3): p. 1598-1605.

14. Wang, Y., et al., *Bacillus subtilis genome editing using ssDNA with short homology regions.* Nucleic acids research, 2012. **40**(12): p. e91-e91.

15. Yamamoto, S., et al., *Application of λ Red recombination system to Vibrio cholerae genetics: Simple methods for inactivation and modification of chromosomal genes.* Gene, 2009. **438**(1-2): p. 57-64.

16. Lesic, B. and L.G. Rahme, *Use of the lambda Red recombinase system to rapidly generate mutants in Pseudomonas aeruginosa.* BMC Molecular Biology, 2008. **9**(1): p. 20.

17. Wang, H.H., et al., *Genome-scale promoter engineering by coselection MAGE.* Nature methods, 2012. **9**(6): p. 591.

18. Kuhlman, T.E. and E.C. Cox, *A place for everything: Chromosomal integration of large constructs.* Bioengineered bugs, 2010. **1**(4): p. 298-301.

19. Kuhlman, T.E. and E.C. Cox, *Site-specific chromosomal integration of large synthetic constructs.* Nucleic acids research, 2010. **38**(6): p. e92-e92.

20. Juhas, M. and J.W. Ajioka, *Lambda Red recombinase-mediated integration of the high molecular weight DNA into the Escherichia coli chromosome.* Microbial Cell Factories, 2016. **15**(1): p. 172.

21. Pósfai, G., et al., *Emergent Properties of Reduced-Genome Escherichia coli.* Science, 2006. **312**(5776): p. 1044-1046.

22. Wang, H.H., et al., *Programming cells by multiplex genome engineering and accelerated evolution.* Nature, 2009. **460**(7257): p. 894.

23. Lajoie, M.J., et al., *Manipulating replisome dynamics to enhance lambda Red-mediated multiplex genome engineering.* Nucleic acids research, 2012. **40**(22): p. e170-e170.

24. Mosberg, J.A., et al., *Improving lambda red genome engineering in Escherichia coli via rational removal of endogenous nucleases.* PloS one, 2012. **7**(9): p. e44638.

25. Mosberg, J.A., M.J. Lajoie, and G.M. Church, *Lambda red recombineering in Escherichia coli occurs through a fully single-stranded intermediate.* Genetics, 2010. **186**(3): p. 791-799.

26. Yang, J., et al., *High-Efficiency Scarless Genetic Modification in Escherichia coli by Using Lambda Red Recombination and I-SceI Cleavage.* Applied and Environmental Microbiology, 2014. **80**(13): p. 3826-3834.

27. Bubnov, D.M., et al., *Development of new versatile plasmid-based systems for λRed-mediated Escherichia coli genome engineering.* Journal of Microbiological Methods, 2018. **151**: p. 48-56.

28. Pyne, M.E., et al., *Coupling the CRISPR/Cas9 system with lambda red recombineering enables simplified chromosomal gene replacement in Escherichia coli.* Appl. Environ. Microbiol., 2015. **81**(15): p. 5103-5114.

APPENDIX B

SUPPLEMENTARY INFORMATION TO SECTION 3

B1. Stator-Rotor Binding

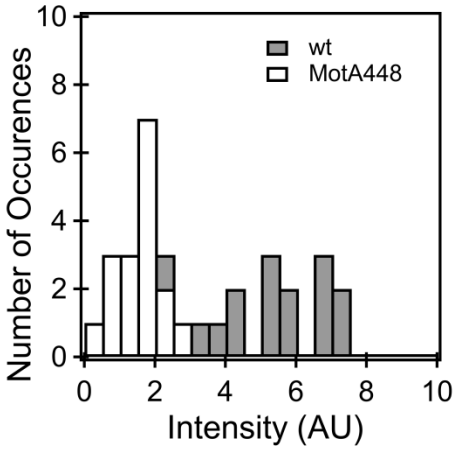

Figure B1: Raw intensity data from figure 2C. Differences between the two means were statistically significant, with fewer eYFP-MotB bound to individual rotors in paralyzed motors.

B2. Steady-state speed

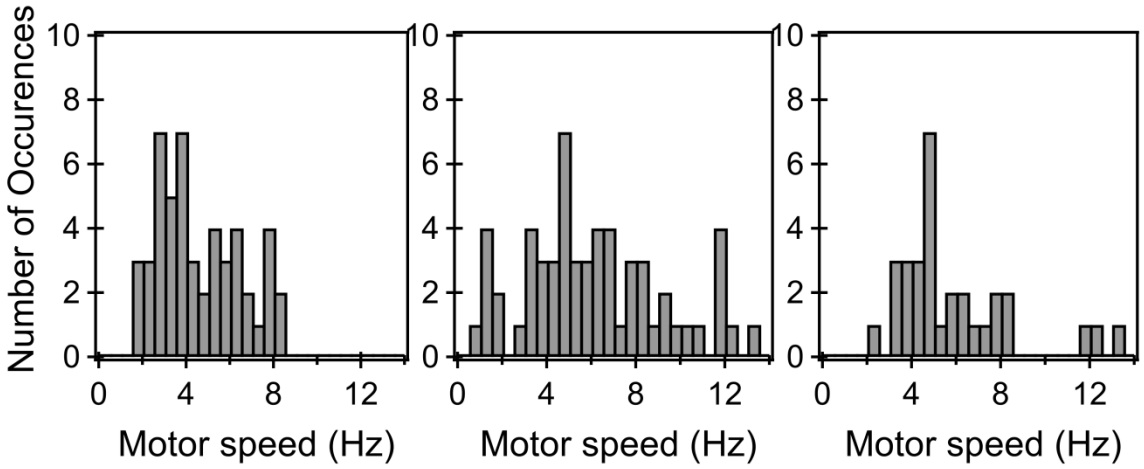

Figure B2. S*peed comparisons*. Steady-state speed distributions determined for the wild-type motors (left panel, MT02, 50 motors), *fliL* mutant (middle panel, strain PL62, 58 motors) and another *fliL* mutant (right panel, strain JP1297; n=30 motors) are shown. The p-values were > 0.05.

B3. Model-linearization and best-fits

We linearized the model presented in equations 3 and 4 as:

$$\log\left(\frac{B_T}{n_{ss}} - 1\right) = \log(\varphi) - {\tau^1}_{max}\delta\left(1 - \frac{\tau}{V_{max}\zeta}\right)/rk_BT \quad (1)$$

The experimental data was then replotted, $\log\left(\frac{B_T}{n_{ss}} - 1\right)$ vs τ/ζ. The chi-square value was ~ 0.1 and R^2 > 0.93-0.99, indicating very accurate fits.

APPENDIX C

SUPPLEMENTARY INFORMATION TO SECTION 4

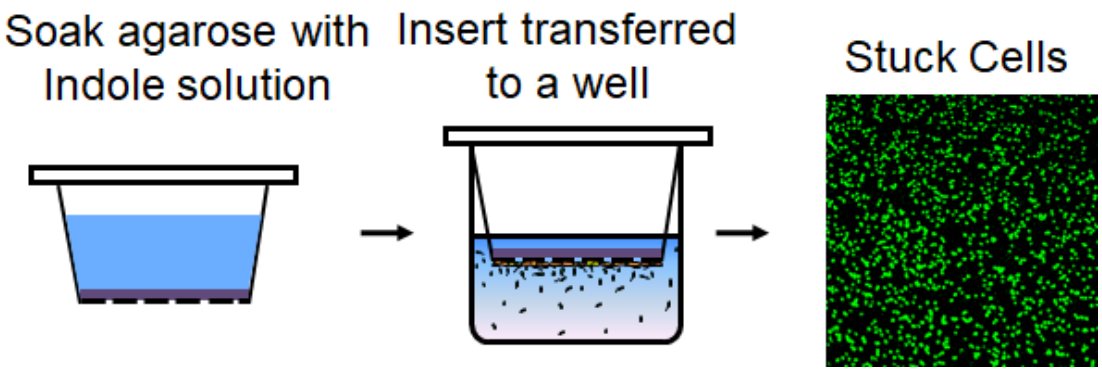

Figure C1: *Transwell insert assay.* Agar was soaked in indole solutions overnight in the insert (left) and the insert was then transferred into a well containing cells (middle). A concentration gradient formed within a few minutes and the cells actively migrated in response to the stimulant. The insert was carefully removed after 5 min, gently washed in MB and imaged via confocal microscopy (right).

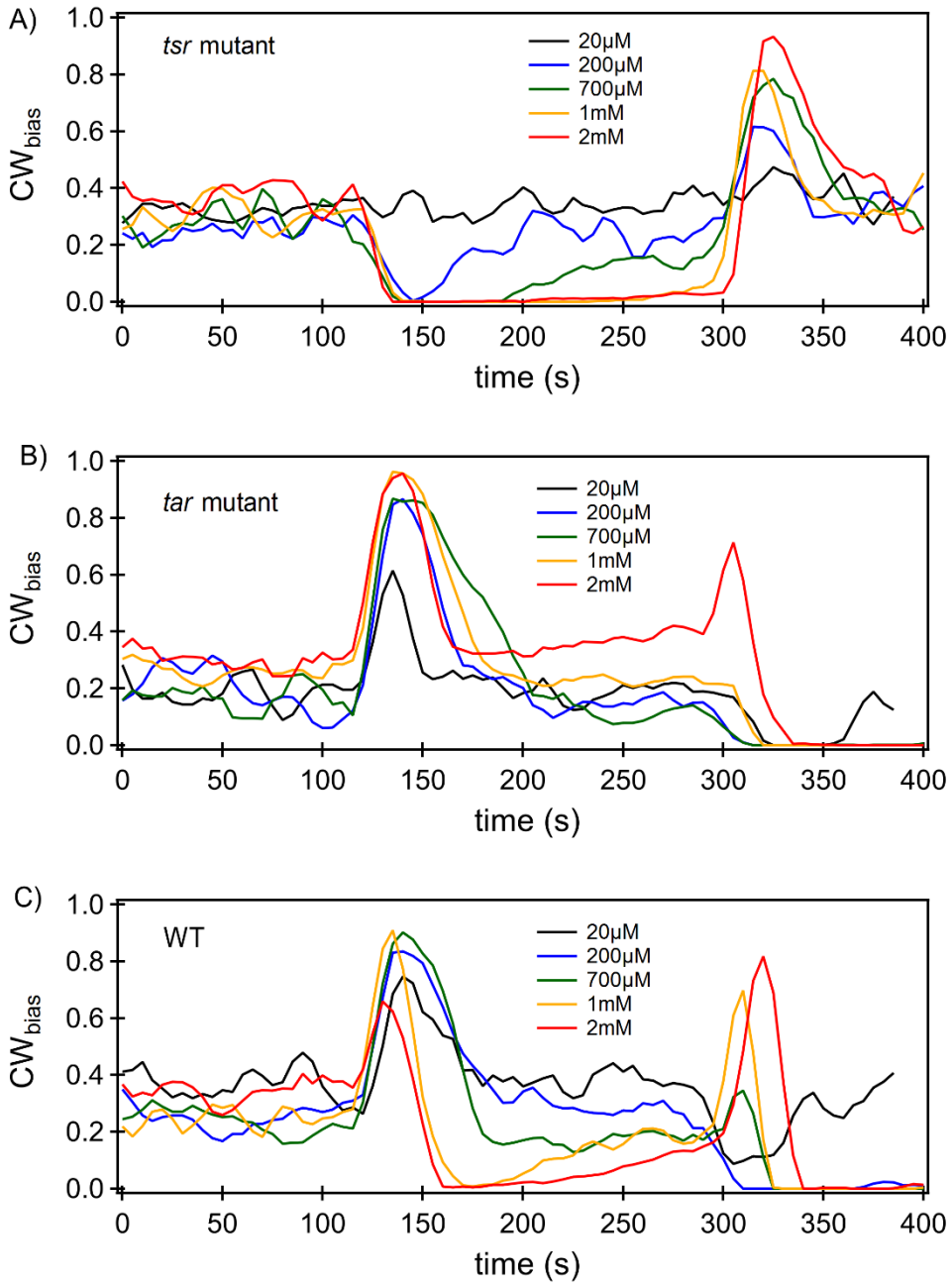

Figure C2: Tethered-cell responses to the addition and removal of indole. Indole was replaced with MB in the perfusion chamber at ~ 300 seconds.

Analytical Modeling of Receptor and Flagellar Motor Mediated Responses

Receptor effects: To simulate the activation of the histidine kinase (CheA) by interactions between the ligand (indole) at a concentration L and the chemoreceptors, we adopted the standard Monod-Wyman-Changeux (MWC) approach. The receptor cluster was assumed to be made up of N sub-clusters, with tight coupling of receptors in each subcluster. The only contributors to the kinase activity were assumed to be N_{Tar} and N_{Tsr} subclusters ($N = N_{Tar} + N_{Tsr}$), representing the two major receptors that form 90% of the total methyl-accepting chemoreceptors. Each subcluster adopted either an inactive or active state, represented by values 0 and 1, respectively. The overall level of activity of the kinase was represented by:

$$\langle a \rangle = (1 - \exp(-N_{Tsr}\Delta G_{Tsr} - N_{Tar}\Delta G_{Tar}))^{-1} \quad (1)$$

The difference in free energy between the active and inactive states for the respective receptor subcluster, ΔG, is a combination of the inherent free energy difference that depends on subcluster methylation level (ΔG_m) and the free energy change due to ligand binding to that subcluster (ΔG_L):

$$\Delta G = \Delta G_m(\tau, m) + \Delta G_L(L) \quad (2)$$

where m represents the methylation level and τ represents the time elapsed since stimulation. Stimulation by indole was assumed to effect an instantaneous change in the free energy due to ligand binding at the instant of stimulation:

$$\Delta G_L = \ln\left(\frac{1+L/K_1}{1+L/K_0}\right) \quad (3)$$

K_1 and K_0 represent the ligand dissociation constants for the active and inactive receptors. Indole was assumed to preferentially bind to the inactive N_{Tar} subclusters ($K_1 >> K_0$) and it was assumed to preferentially bind to the active N_{Tsr} subclusters ($K_1 << K_0$), stabilizing the inactive and active states of the Tar and Tsr subclusters, respectively. This represents the competing responses of the two receptors to indole.

The adaptation in the kinase activity upon stimulation was represented by:

$$\Delta G_m = \propto (m_o) - \propto (m) \frac{t}{c+t} \quad (4)$$

where the time constant c determined the adaptation rate and α represented a proportionality constant. A high value of c was assumed for the Tar receptor to reflect its slow adaptation in Fig 2D and a low value of *c* was assumed for the Tsr receptor to reflect the faster adaptation kinetics observed in Fig 2C.

Motor effects: The kinase activity directly sets the level of CheY-P and the CW_{bias} depends ultrasensitively on CheY-P levels. The bias was modeled as:

$$CW_{bias} = (1 - exp(\Delta G_{FliG} - a.\varepsilon))^{-1} \quad (5)$$

where ΔG_{FliG} represents the free energy difference between the CW and CCW conformations of the FliG ring, and ε represents the binding energy per molecule of CheY-P, which remains constant. ΔG_{FliG} was assumed to change linearly with Indole concentrations to mimic the modulation of FliG subunit energetics by the metabolite. Thus, equation 5 enabled predictions of the combined receptor- and motor-mediated responses to Indole. Setting *a* constant (and independent of L) at a basal activity level (a_o) enabled predictions of the switch-only response to indole. On the other hand, assuming ΔG_{FliG} to be invariant with respect to indole concentrations and a non-zero ε enabled predictions of receptor-only mediation to Indole.

Fig S2A shows receptor-only effects, where the stimulation of wild-type cells with increasing indole concentrations is correctly predicted to result in a repellent peak at short-times. At low concentrations (20 μM), the Tsr contribution (black curve) is dominant, and

the response adapts over long-times to the pre-stimulus values. However, at higher concentrations of Indole, the contribution from the Tar receptor begins to dominate over long-times, as observed by the reduction in post-stimulus CW_{bias} below the pre-stimulus levels. The deletion of the Tsr or Tar receptors, can be modeled by setting N_{Tsr} and N_{Tar} values to 0, respectively. The resultant responses were correctly predicted to be purely attractive (Tsr deletion) or repulsive (Tar deletion), respectively (results not shown).

As discussed in the previous section, indole likely offsets the free energy difference ΔG_{FliG} between the CW and CCW conformations of the individual FliG ring, directly. At a constant receptor activity level a_o, an indole concentration-dependent decrease in ΔG_{FliG} is predicted to cause a concomitant step increase in the post-stimulus CW_{bias} (Fig S2 B). Finally, the predictions for the combined effects of receptor stimulation and switch stimulation by Indole (equation 5) are shown in Fig S2C. Although the 20 μM case (black curve) correctly predicts the purely repellent response and adaptation that was observed in the wild-type motors (Fig 1A), increasing concentrations of indole are predicted to cause a disappearance of the attractant response that is mediated by Tar with a steady non-adapting offset (long-time post-stimulus response is higher than pre-stimulus response). The disappearance of the attractant response and the emergence of the offset were due to the purely-repellent response of the flagellar switch to Indole, which was observed experimentally (Fig 2). Although the Tsr-mediated short-time repellent response was observed in the predictions at all concentrations, the permanent long-time offset was not seen over the duration of the experiments (~300 s). Further modeling under the assumption of imprecise adaptation to indole to compensate for the switch-induced offset did not resolve the discrepancy in predictions (receptor plus switch effects) and experiments (Fig 1, 2).

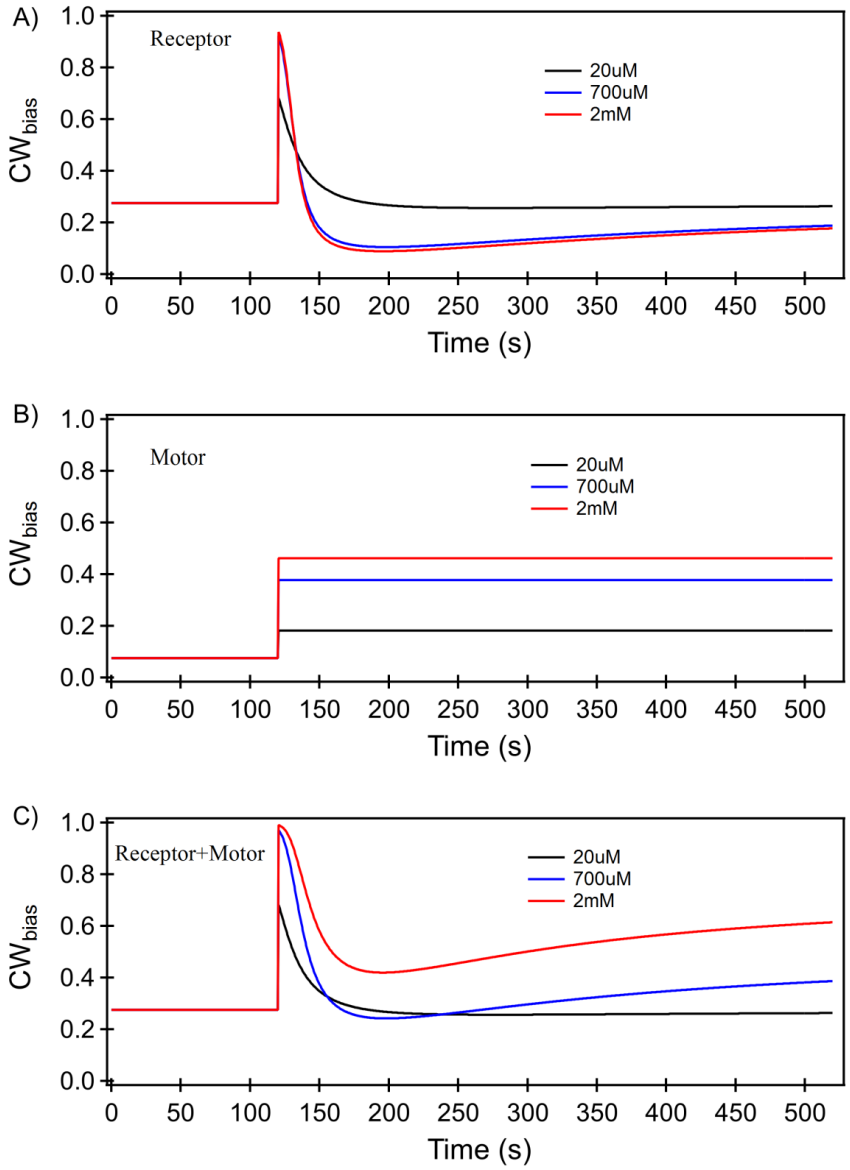

Figure C3. A) Predictions for receptor-mediated motor responses. Stimulation by ligand occurred at 120 s and the change in CW_{bias} was assumed to depend solely on receptor-mediation. At 20 μM Indole (black curve), response is purely repellent (increase in bias) followed by perfect adaptation to pre-stimulus levels. At higher concentrations, the conflicting Tsr and Tar contributions are observed by the short-time increase in bias

(repellent response) and the long-time decrease in bias (attractant response), respectively. **B)** Predictions for direct Indole action on motor responses. The offset in ΔG_{FliG} (equation 5) was assumed to increase with Indole levels. A constant receptor activity-level a was assumed. The post-stimulus levels do not adapt and the response at all concentrations is purely repellent and independent of receptor-mediation. **C)** Combined effects of motor- and receptor-mediation. A repellent response is predicted at low concentrations (20 μm) that adapts perfectly. At higher concentrations of Indole, the attractant response disappears and is replaced by a permanent offset (post-stimulus response > pre-stimulus levels).

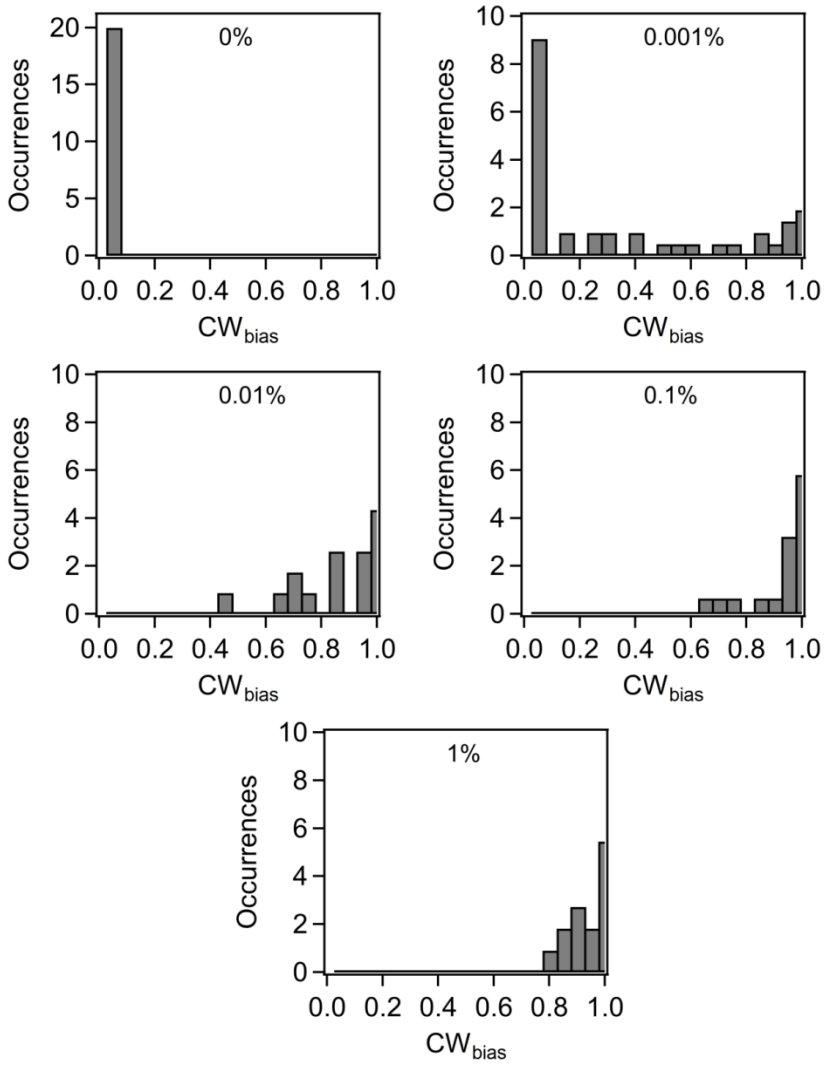

Figure C4: CW_{bias} distributions as a function of the expression levels of CheY in a Δ*cheRcheBcheY* background. The *cheY* allele was encoded on a pBAD34 vector which is inducible with L-arabinose. The inducer concentrations are indicated for each plot. Induction with 0.001% L-Arabinose enabled sampling of tethered cells with a pre-stimulus bias of ~0.2.